Electromagnetic Energy Transduction Using Metamaterials and Antennas

by

Thamer Almoneef

A thesis

presented to the University of Waterloo

in fulfilment of the

thesis requirement for the degree of

Doctor of Philosophy

in

Electrical and Computer Engineering

Waterloo, Ontario, Canada, 2017

Examining Committee Membership

The following served on the Examining Committee for this thesis. The decision of the Examining Committee is by majority vote.

External Examiner	John Volakis Professor
Supervisor(s)	Omar Ramahi Professor
Internal Member	Raafat Mansour Professor
Internal Member	Christopher Backhouse Professor
Internal-external Member	Behrad Khamesee Professor

I hereby declare that I am the sole author of this thesis. This is a true copy of the thesis, including any required final revisions, as accepted by my examiners.

I understand that my thesis may be made electronically available to the public.

Abstract

The advent of rectenna systems almost half a century ago has enabled numerous applications in a number of areas, with the main goal of recycling the ambient microwave energy. In previously presented rectennas, microstrip antennas were the main energy source used to capture and convert microwaves to AC power. However, the conversion efficiency of antennas have never been examined in terms of their capability of absorbing microwave energy, and hence any enhancements to the overall efficiency of rectenna systems were mainly attributed to the rectification circuitry instead of the antenna.

In the first part of this dissertation, a novel electromagnetic energy collector is presented, consisting of an array of Split Ring Resonators (SRRs), used for the first time as the main electromagnetic source of energy in a rectenna system. The SRR array is compared to an array of patch antennas to determine the radiation to AC efficiency when both arrays are placed on the same footprint. Numerical simulations and experimental tests show that the SRRs achieve higher efficiency and wider bandwidth than microstrip antennas. The idea of electromagnetic energy harvesting using metamaterials is further explored by designing a metamaterial slab based on the full absorption concept. The metasurface material parameters are tuned to achieve a surface that is matched to the free space impedance at a certain band of frequencies to minimize any reflections and ensure full absorption within the metasurface. The absorbed energy is then channeled to a resistive load placed within each element of the metasurface. Different from previous metasurface absorber designs, here the power absorbed is mostly dissipated across the load resistance instead of the substrate material. A case study is considered where the metamaterial slab is designed to operate at 3 GHz. The simulation and experimental results show radiation to AC efficiencies of 97% and 93%, respectively.

A novel method is proposed in the second part of the thesis that significantly increases the conversion efficiency of electromagnetic energy harvesting systems. The method is based on utilizing the available vertical volume above a 2-D flat panel by vertically stacking panels while maintaining the same 2-D footprint. The concept is applied to SRRs and folded dipole antennas. In both cases, four vertically stacked arrays are compared to a single array panel, both occupying the same flat 2-D footprint in terms of power efficiency. The numerical and experimental results for both the SRRs and the antennas show that the stacking concept can increase the conversion efficiency by up to five times when compared to a single 2-D flat panel.

The third part presents the design of a near unity electromagnetic energy harvester that uses a Tightly Coupled Antenna array. Compared to the unit cell of metamaterial surfaces, the dimension of a TCA unit cell is about five times larger, thus providing simplified channeling networks and cost-effective solutions. The TCA surface contains an array of Vivaldi shape unit cells with a diode at each cell to convert the harvested electromagnetic energy to dc power. The dc power from each unit cell is channeled to one single load via series inductors. A sample 4×4 TCA array, when simulated, fabricated and tested shows solid agreement between the simulated and measured results.

The thesis then discusses the idea and design of a dually polarized metasurface for electromagnetic energy harvesting. A 4×4 super cell with alternating vias between adjacent cells is designed to allow for capturing the energy from various incident angles at an operating frequency of 2.4 GHz. The collected energy is then channeled to a feeding network that collects the AC power and feeds it to rectification circuitry. The simulation results yield a radiation to AC, and AC to DC conversion efficiencies of around 90% and 80%, respectively. As a proof of concept, an array consisting of nine super cells is fabricated and measured. The experimental results show that the proposed energy harvester is capable

of capturing up to 70% of the energy from a planewave with various incident angles and then converting it to usable DC power.

As future work, the last part introduces the concept of metasurface energy harvesting in the infrared regime. The metasurface unit cells consist of an H-shaped resonator with the load placed across the gap of the resonator. Different from infrared metamaterial absorber designs, the resonator is capable of not only full absorption but also maximum energy channeling across the load resistance. The numerical simulation demonstrates that 96% of the absorbed energy is dissipated across the load resistance. In addition, a cross-polarized H-resonator design is presented that is capable of harvesting infrared energy using dual polarization within three frequency bands.

Acknowledgments

In the name of Allah the All-Merciful, The Ever-Merciful.

First and foremost, I would like to thank Allah ,the Almighty, for giving me the strength to successfully accomplish this thesis and for blessing me with great family and friends, whom have been my greatest support in both my personal and professional life.

I want to express my sincere gratitude to my supervisor Prof. Omar M. Ramahi. I cannot thank him enough for his support, guidance, friendly advice and excellent supervision. Thanks to him for the discussions that we had which always sparked novel ideas. I also like to extend my gratitude to my committee members, Prof. Raafat Mansour, Prof. Christopher Backhouse, Prof. Behrad Khamesee, and Prof. John Volakis for spending their time to read my thesis and give valuable comments and feedback.

I like to express my deepest gratitude and appreciation to my dear parents Solaiman Almoneef and Norah Altahini for their love, support and sincere advice. They supported me in all aspects of this life and I would always be indebted to them. I would also like to thank my siblings, my uncles, my aunts and all my family members for being there for me in hard situations before the pleasant once. My apologies to them for being away for a long time.

Special thanks to my wife and best friend Hetaf Almehbash. I cannot thank her enough for her continuous support and patience during this journey. Thanks to Allah for blessing me with my cute and lovely daughter Danah. She indeed was an important factor in making my life in Canada more enjoyable, especially whenever I picked her up from day care after a very exhaustive day at the university. I am also thankful to my father in law Fahad Almehbash and my mother in law Fatima Altasan for being understanding and

considerate while my family is away, specially their granddaughter Danah. May Allah bless them all with health and good spirit.

I would like to thank my current and former electromagnetic research group members at the University of Waterloo. I am very lucky to be part of this active and friendly group. Specifically, I would like to thank Dr. Muhamed Boybay, Dr. Babak Alavikia, Dr. Zhao Ren, Dr. Mohammed Bait-Suwailam, Dr. Khawla Alzoubi, Dr. Mohammed AlShareef, Dr. Miguel Ruphuy, Dr. Abdulbaset Ali, Faruk Erkmen, Ahmed Ashoor, Mohamed El Badawe, Ali Albishi, Dawood Alsaedi, Maged Aldhaeebi, Seyed Mirjahanmardi, Mohammed Aldosari, Saeed Bamatraf, Melad Olaimat and Jamal Busnaina. My apologies to those whom I forgot to mention here. Their friendship will always be remembered.

This PhD research work was supported by Prince Sattam University, Saudi Arabia. This dissertation would have been extremely difficult to accomplish without their generous financial support.

Dedication

To my dear parents and siblings, my beloved wife Hetaf and my lovely daughter Danah

Table of Contents

List of Tables

List of Figures

Chapter 1

Introduction

1.1 Wireless Power Transfer: Types and Classification

Electromagnetic energy harvesting is commonly discussed under the broad topic of Wireless Power Transfer (WPT); in fact it is regarded as an application of WPT systems. A general WPT system consists of transmitting circuitry and a transmitter antenna for transmiting electromagnetic waves at a specific frequency or range of frequencies. This electromagnetic wave travels through a medium to a receiving system. The receiving system consists of a receiving antenna and a receiving circuit, which together capture the incoming wave to perform a specific task depending on the desired

application. This method transfers the power in the far field of the transmitting antenna where the receiving antenna is placed several wavelengths from the transmitting antenna. In another method of transferring electric power wirelessly, two coils are placed electrically close to each other such that the energy from one coil is coupled to that of the other coil in a manner similar to that used in electrical transformers. Hence, WPT systems can be classified in general into three main types: 1) Near field, 2) Mid field and 3) Far field WPT systems, as shown in the block diagram of Fig. 1.1.

The difference among the three types depends strictly on the separation distance between the transmitter and the receiver. When the separation distance is comparable to or less than the size of the transmitter, the transmitter and the receiver experience strong near field coupling and thus it is regarded as a near-field WPT system.

In the near field, the energy can be coupled either inductively or capacitively to the receiver. Figure 1.2 illustrates the components of the inductively coupled WPT system. The inductive coupling method utilizes a primary coil driven by an AC source that generates an alternating magnetic field. This magnetic field is then coupled to a secondary coil placed at a distance less than the size of the coil. Therefore, the power transfer efficiency between the coils is the ratio of the power delivered to the load

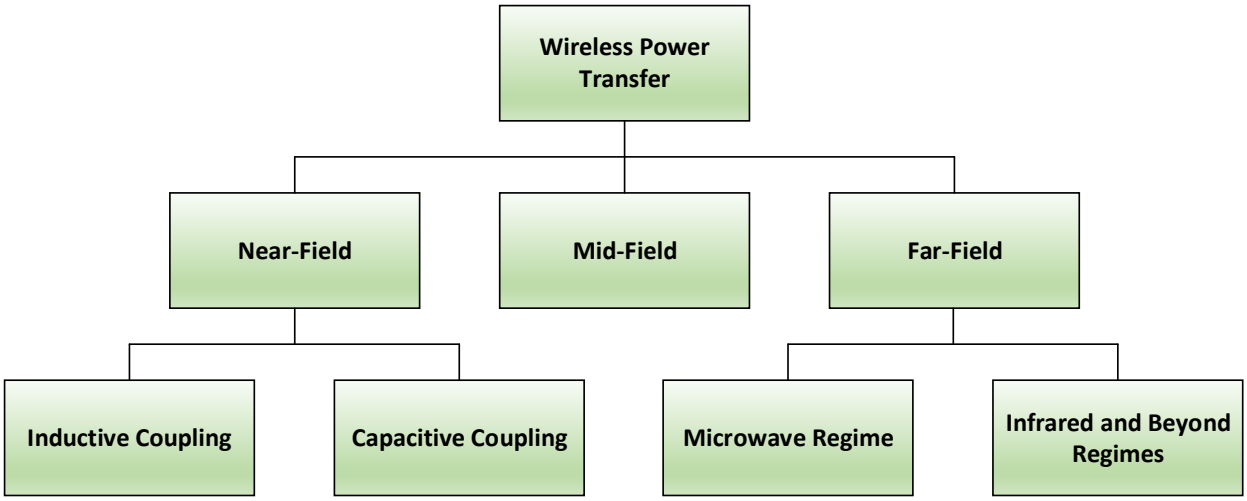

Figure 1.1: A block diagram showing the different classifications stemming from WPT systems.

of the secondary coil to the injected power exciting the primary coil. This efficiency is highly dependant on the quality factor of the coils, the strength of the coupling between the coils (which is dictated by the separation between the two coils), and the alignment of the two coils [3, 4]. This method has proved to be very effective in biomedical applications where the energy is transferred to an implanted device through inductive coupling [5].

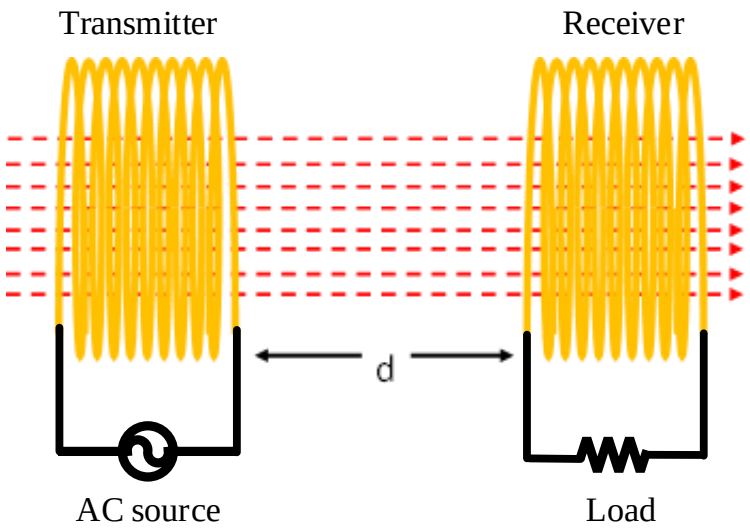

Figure 1.2: A schematic illustrating an inductively coupled WPT system.

Capacitive coupling utilize the electric field as the main energy carrier instead of the magnetic field ;therefore, it can be regarded as the dual of inductive coupling. In capacitive coupling, four metallic sheets are used to form two capacitors as shown in Fig. 1.3. The use of the two capacitors is essential to forming a closed loop by which the current flows from the source to the desired load. The energy transferred between the capacitor plates is based on the principle of displacement current. Hence, higher power transfer can be achieved with higher displacement currents. These currents can be realized by increasing the area of the capacitor plates;increasing the

operating frequency, which consequently increases the rate of change of the electric field; and/or increasing the dielectric permittivity of the medium between the plates of the capacitors [6, 7]. Electric vehicle battery charging [8] and implantable biomedical devices [9] are examples of applications for WPT being capacitive coupling.

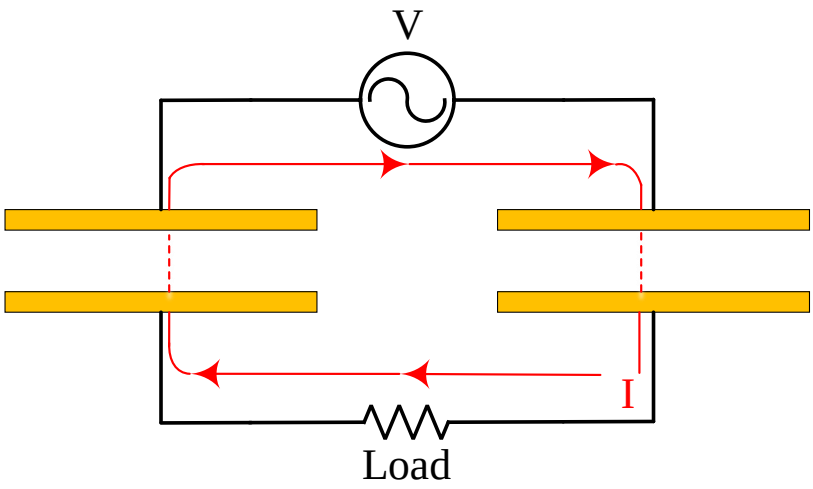

Figure 1.3: A schematic illustrating a capacitively coupled WPT system.

When the desired application requires a larger separation distance than the radius of the transmitting coil, mid field WPT can be used, which is based on the concept of resonance energy transfer [10]. In this method, the transmitter consists of a driven loop excited by an RF amplifier and a spiral coil made of N number of turns. Similarly, the receiver consists of a spiral coil and a receiving loop terminated by a load having the same size

and dimensions as the transmitter's coil and exciting loop, as shown in Fig. 1.4. When the transmitter coil is excited by an RF source, a magnetic field is generated, which will couple to the spiral coil. The spiral coil acts as an RLC resonator oscillating at a specific frequency. The energy stored in the transmitting coil is then coupled magnetically to the receiving coil through the mutual inductance between them. This process induces a current in the receiver loop, which then causes a voltage to develop across the terminated load [11]. Charging consumer electronics [12], electric vehicles [13] and biomedical implanted devices [14] are applications of the resonance energy transfer method. In this thesis, the contribution is to the far field WPT, and therefore it will be discussed in depth in the following sections.

1.2 Far Field WPT and Rectenna Systems: Mechanism of Operation

In this thesis, the focus is on transferring the energy wirelessly in the far field where the separation between the transmitter and the receiver is multiple wavelengths apart and in some cases hundreds or thousands of wavelengths away, as we will see in the feasible applications of such a system. A far field based WPT system consists of a transmitter, a travelling medium and

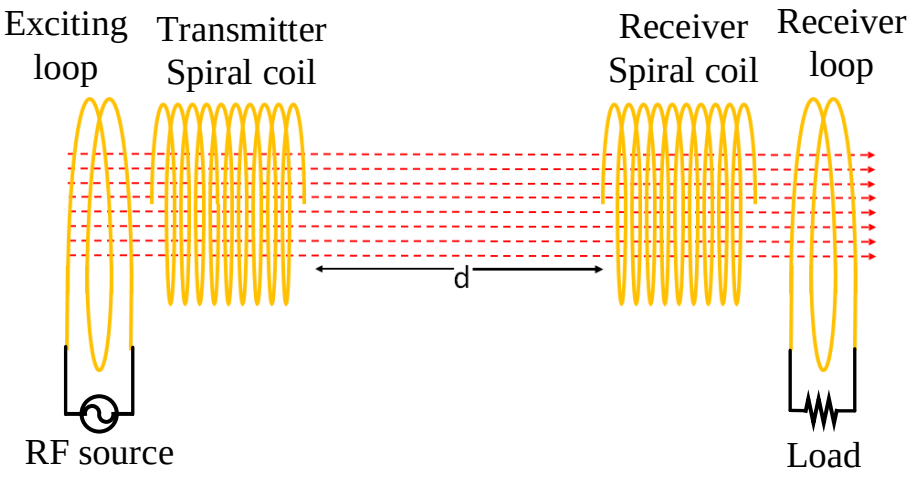

Figure 1.4: A schematic illustrating the setup in a magnetic resonance (mid field) WPT.

a receiver. The receiving part consists of an antenna to capture the electromagnetic radiative waves and convert it to AC power across the feed of the antenna, and a rectifier to convert the AC power to DC power across a terminating load. Because it is formed by integrating an antenna and a rectifier, the receiver part is commonly referred to as rectenna system. A block diagram of the individual constituents of a rectenna system is shown in Fig. 1.5. In a rectenna system, an antenna is used to collect the electromagnetic energy from the ambient and convert it to AC power. A matching network is then used in the pre-rectification stage to match the impedance of the antenna to that of the diode impedance and to ensure maximum

power transfer to the diode. A diode is then used to convert the AC power to DC. In the microwave regime, a Schottky diode is commonly used for the rectification process. In the infrared regime and beyond, however, a Metal Insulator Metal diode (MIM) is used instead for its fast switching speed at the operation frequency. At the post rectification stage, a DC filter is integrated to smooth out the rectified AC power so that a constant DC power is apparent across the terminated load. The most common application of far field wireless power transfer is electromagnetic energy harvesting from the ambient [15–17] and from space [18], which will be discussed in further detail in section 1.4. From this point in the dissertation and beyond, only far field WPT is discussed as it comprises the main area the author contributes to.

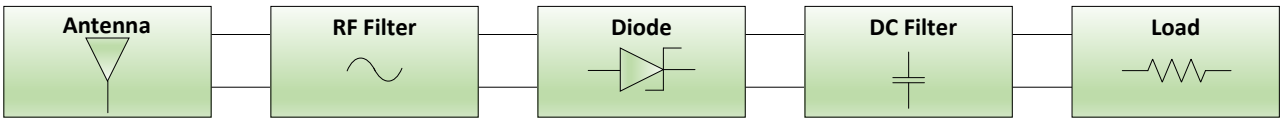

Figure 1.5: A block diagram showing the 5 components that form a rectenna system.

1.3 Historical Millstone

It could be argued that transferring power without wires dates back to the early work of Michael Faraday in 1831. In his experiment, he was able to

transfer energy from one coil to another without physical connection. This discovery led to what is known now as Faraday's law of electromagnetic induction. A famous application based on his discovery is the electric transformer. However, due to the strong mutual inductive coupling required, the coils must be placed in close proximity to each other limiting the feasibility of using such devices to transfer energy over appreciable distances [19, 20]. A few decades later, James Clerk Maxwell predicted that electromagnetic disturbances cause a wave to propagate through the ambient traveling at the speed of light [21].

In 1888, Heinrich Hertz demonstrated Maxwell's prediction of propagation of electromagnetic waves in free space. In his experiment, an induction coil was used to charge the opposite halves of a dipole with high voltage. This generated a spark across the gap of the dipole antenna. As a result, propagation of electromagnetic waves was detected by a receiver made of a loop antenna. He also used reflectors to help in directing the radiated energy to the receiver [22]. This vital demonstration is regarded to be the first experimental validation of Maxwell's hypothesis of electromagnetic propagation in free space travelling with the speed of light.

At the end of the 19th century, Nikola Tesla conducted another attempt at wireless power transfer. The experiment apparatus included a huge coil

resonating at 150 kHz and a 60 m pole placed over the coil. A sphere made of 1 m diameter copper ball of was placed on top of the pole. A 300 kW power with low frequency was used to excite the coil. Consequently, high voltage of up to 100 MV was produced at the sphere. The generated high sparks were used to light up 200 light bulbs at a distance from the base station. At the dawn of the 20th century, many researchers were interested in the concept of wireless power transfer, especially after the experiments carried out by Tesla [23]. However, limitations on available high power and high frequency energy sources were a barrier against effective wireless power transmission over longer distances.

The modern era of WPT was sparked in 1950s when high power microwave tubes were developed, enabling efficient transmission of high power. The first efficient WPT system was developed by William C. Brown in 1963 [22, 24]. He carried out an experiment using a transmitter that fed a horn antenna with a power level of 400 W at the resonance frequency of 2.45 GHz. At the receiving part, a reflector was used to focus the received energy to a focal point where the energy was collected by a diagonal horn antenna. Using thermionic diodes, the energy was then converted back to DC with an efficiency of up to 50%. This low efficiency was mainly attributed to the losses of the thermionic diode used during the conversion of AC power to

DC. Brown knew that it was essential to develop a more efficient diode to boost the efficiency of the total system. In response to his interest, Hewlett-Packard Associates developed the 2900 silicon Schottky-barrier diode having smaller size, higher efficiency and better power-handling capabilities than the thermionic diodes [25].

An important milestone in the history of transferring power wirelessly over relatively long distances was an experiment conducted in 1975 in the Mojave Desert. In the experiment, a transmitting parabolic antenna was fed by a high powered klystron with a frequency of 2.4 GHz. The energy transmitted by the parabolic antenna was picked up by a receiver placed 1.54 km away from the transmitter. The receiver consisted of 4590 rectennas occupying a footprint of 26 m^2, each rectenna consisting of a dipole antenna and a Schottky diode. Part of the generated 30 kW DC power was used to power a set of light bulbs, each pair of bulbs energized by a group of rectennas [24, 26]. This experiment has considered to be successful for its high conversion efficiency that reached up to 84% over a long distance. Following the success of the Mojave Desert experiment, a number of programs were launched in Canada and Japan, aiming for microwave power transfer to a specific target such as unmanned airplanes [24].

Since the efficiency of a WPT system is affected mostly by the receiving

part, the focus was shifted to developing efficient and reliable rectennas. In 1985, a printed rectenna system was developed by Brown and Triner [27]. The key advantage of printed technology is its light weight, it being approximately 10 times lighter than antennas made of metallic rods. The designed rectenna was operating at 2.45 GHz, achieving conversion efficiencies of up 85%. Due to their low cost, light weight and ease of fabrication, most rectennas developed since then have been made of printed technology.

The emphasis of recent developments reported in the literature focuses in improving various aspects of rectenna systems, depending on the targeted application. To increase the reliability of the rectenna system, rectennas operating at dual or multiple bands where designed to increase the amount of collected energy [28,29]. However, the challenge is to design a single rectifier that operates at the multiple selected frequencies or instead build multiple rectifiers where each rectifier covers one frequency band, thus adding more weight, cost and complexity to the rectenna system. Other rectenna designs proposed the use of wide band antennas to scavenge energy from a wide range of frequencies [30–32]. However, to channel the collected energy efficiently to a diode, a matching network must be used to match the diode impedance to that of the antenna over a wide band. The use of a matching network will limit the bandwidth over which the energy is channelled to

the diode effectively. Hence, the work reported in [33,34] proposed the idea of mounting diodes right at the feeds of wideband spiral antennas, without a matching network. Although wideband response was achieved, the total efficiency was compromised, having efficiencies ranging only between 5 - 45 %.

In previous works, various types of rectenna systems were presented as a single element [35–37] and in array form [38–40]. A number of rectifiers were used, such as a half-wave series diode [41], a half-wave shunt diode [42], voltage doublers [43] and full-wave rectifiers [44]. The rectified power can be smoothed by simply connecting a series inductor [35], shunt capacitor [45] and short and open stubs [46] before the load resistance. The rectified DC power can be channeled in series, parallel, or a combination of both [16, 47, 48]. However, the channeling mechanism remains a challenge for the full-wave rectifier topology. In the work presented in [44], an array of dipoles with full-wave rectification was studied, and a channeling mechanism was proposed where by a full wave rectifier was connected between two dipoles, and the rectified energy was channeled and filtered through a high inductor placed between the dipole antennas. The choice of the rectifier along with the channeling mechanism depends on the desired voltage or current level across the connected load. For the energy collector part, mi-

crostrip based antennas were used, including but not limited to dipoles [49], patches [50], bow-ties [51], spirals [52] and loops [53]. The choice of antenna type used depends on the targeted application, such as dual frequency operation [54], circular polarization [55], broadband reception [34,56], wireless power transfer [57], and dual polarization [58].

A new type of energy collector was introduced in [59], which consists of an array of electrically small metamaterial particles made of Split Ring Resonators (SRR). An array of 9×9 SRRs showed wideband reception with radiation to AC efficiency of up to 75% at the operating frequency of 5.8 GHz [59]. A comparative study between an SRR array and a patch antenna array both occupying the same footprint area and operating at the same frequency is presented in [60]. The study suggests that the SRR array can achieve 30% more radiation to AC efficiency than the efficiency achieved by the patches.

Since then metamaterials have played an important role in the design of the main collector for rectenna systems [61–63].

In a recent article [64], a metamaterial surface made of 13×13 electrically small resonators was presented as a new electromagnetic collector or antenna. The results show that a radiation to AC efficiency of near unity is feasible.

This dissertation expands the boundary of rectenna system theory and design by incorporating metamaterials as the main energy source in a rectenna system, as will be discussed in the following chapters in further detail.

1.4 Applications

The advancement of the rectenna system has enabled numerous applications since its main goal is to deliver efficient DC power to a load wirelessly. A vital application of rectenna systems was proposed by Petter E. Glasser in 1968: to use rectennas to harvest energy from space in what was termed Space Solar Power (SSP) [65]. In SSP, solar energy is converted to electricity using arrays of solar cells placed 22,300 miles above the Earth's equator. Then the collected power is converted to microwaves and transmitted to a receiver site located on earth, using a highly directive antenna. Large rectenna arrays would then receive the microwave energy and convert it to electricity [18]. Although SSP is not operational at the time of this dissertation, it is believed to be very promising for our energy future, with great amount of money being devoted to projects in many countries, especially Japan and the USA [66].

One of the most important applications of rectenna systems is electro-

magnetic energy harvesting in both the microwave and infrared regimes. In the microwave part of the spectrum, rectennas are designed to scavenge energy from various communication applications, such as TV broadcasting, cellular towers, and WIFI modems [29]. In the infrared regime, however, rectennas are designed to collect the infrared radiation from the solar system. An advantage of such application is that infrared energy is available even at night time, due to the cooling process of earth, which releases significant amounts of infrared energy, enabling infrared rectennas to scavenge energy around the clock [67].

Other applications of rectenna systems reported in the literature are RFID's [68], driving mechanical actuators [58], implantable biomedical devices [69], remote sensing [70] and many others.

This dissertation does not target a certain application in particular but rather proposes a rectenna system that can be used in almost any application presented in the literature.

1.5 Efficiency Calculation

In previous works, the energy collector elements used were classical antennas of printed (low-profile) [28, 34, 38, 45, 55, 71] and non-printed types [72].

Interestingly, in all previous works concerned with electromagnetic power transfer or electromagnetic energy harvesting, the antennas used were those that have been tested and employed extensively for communication systems. In electromagnetic energy harvesting, antennas are used purely in the receiving mode. Despite the applicability of the reciprocity theorem to receive-transmit antenna pairs, a receiving antenna's behavior cannot be comprehensively predicted by understanding its behavior when operating in the transmission mode (please refer to section 2.4 for further details). These, amongst other considerations particular to the reception of traveling plane waves, design of receiving antennas or energy collectors in general, need to be viewed with a fresh perspective distinct from that considered for communication systems.

We have demonstrated through numerical simulation and experiment that an SRR array can be used to collect electromagnetic energy [59]. In developing a new electromagnetic energy harvesting platform, it is critical to demonstrate that the new platform, for now assumed to be a flat surface, provides energy conversion efficiency higher than which could have been achieved using previously used collector or antenna technology. Notice that in general, the efficiency of an antenna in the transmission mode is different from that in the receiving mode. In the transmission mode, the efficiency

of the antenna is simply the ratio of the power radiated to the power accepted by the terminals of the antenna. In the receiving mode, the antenna experiences a plane wave arriving from one or more directions, a physical scenario that is not reciprocal to the energy *explosion* scenario of the transmission mode (Notice that an implosion of waves would be the reciprocal of the explosion of waves, which is clearly not what the receiving antenna experiences). Therefore, a new method for computing the efficiency of collectors is introduced for describing the efficiency of collectors in general and their ability to harvest available electromagnetic energy. For example, if the rooftop of a building of defined area A $\times$ B as shown in Fig. 1.6 is to be used for electromagnetic energy harvesting, then the efficiency of the system would be the efficiency of the collectors in converting all power incident on the rooftop to available AC power. It is important to realize that this new definition, first reported in [59], does not depend on the effective area of the collectors but on the total area occupied by the collectors. This definition is given by

$$\eta = \frac{P_{av}}{P_{area}} \tag{1.1}$$

where P_{area} is the total time-average power incident on the footprint and P_{av} is the time-average AC power received by all collectors occupying

the same footprint under consideration and which is available at the feed terminal of the receiving collectors. For N collectors, P_{av} is given by:

$$P_{av} = \sum_{i=1}^{N} \frac{V_i^2}{R_i} \tag{1.2}$$

where V_i is the voltage across and the resistance R_i of collector i. This efficiency definition allows for a meaningful comparison between different energy collectors.

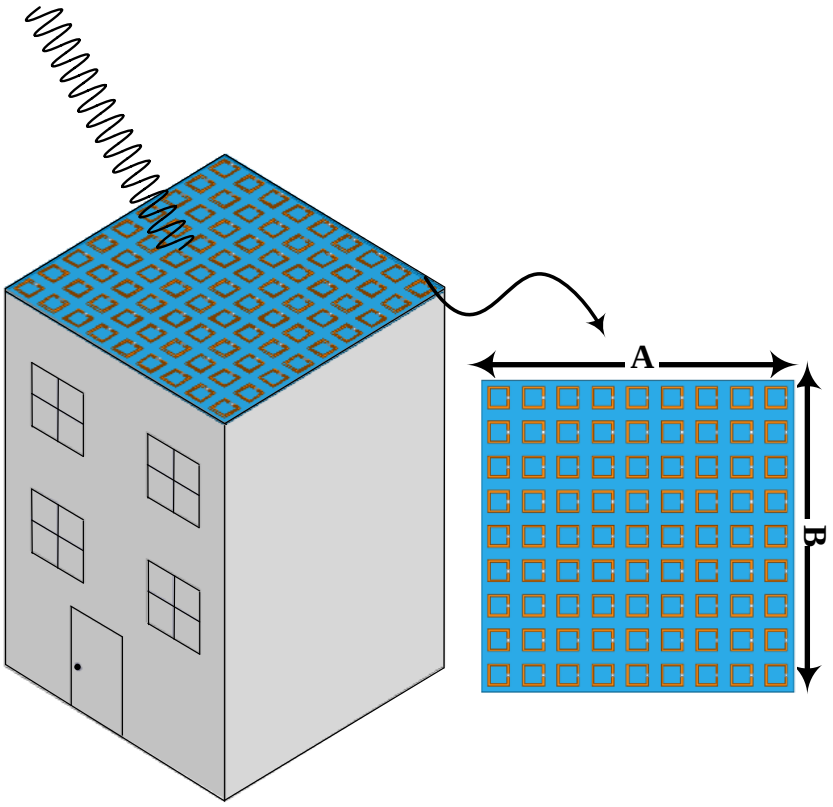

Figure 1.6: An illustration describing the proposed efficiency concept, highlighting the importance of the total footprint in the overall consideration of the energy-harvesting system.

In this dissertation, the efficiency definition is used in two forms: the radiation to AC and the radiation to DC conversion efficiencies. The efficiency definition of the two forms is the same except that the output power

across the resistive loads is AC or DC depending on whether the circuit connected across the terminals of the collector is simply a resistor or a full rectification circuitry.

1.6 Research Problem and Contributions

The efficiency of a rectenna system undergos two main stages: the radiation to AC conversion efficiency (antenna) and the AC to DC conversion efficiency (rectifier). In previous works, the main electromagnetic collector used to capture and convert the electromagnetic energy to AC power is the antenna. The losses of the rectenna system during the conversion of radiation to DC power was mainly attributed to the rectification circuitry. Hence, the contributions were mostly focused on enhancing the AC to DC conversion efficiency which is mainly attributed to the type of diode used and the AC/DC filtering before and after the diode. However, the efficiency of the antenna in the receiving mode has never been studied, even though it is the main energy source and the most critical part of a rectenna system. Of particular importance is, the efficiency of the receiving antenna per footprint, as it is the most meaningful efficiency definition and describes the ability of any collector to harvest electromagnetic energy.

Therefore, the course of this work is focused on the following:

1. **Introduce** an efficiency definition that is capable of analyzing the ability of any electromagnetic energy collector to leverage the electromagnetic energy that impinges on a footprint area.

2. **Analyze** the radiation to AC conversion efficiency of the collectors used in current rectenna systems (antennas)

3. **Introduce** an electromagnetic energy collector based on metamaterials that is capable of achieving higher radiation to AC conversion efficiency per footprint relative to the collectors presented in the literature

4. **Extend** the concept proposed in 3 to solve the problem of harvesting electromagnetic energy independent of the polarization of the incoming wave (a polarization independent energy harvester)

5. **Introduce** a method for enhancing radiation to AC and the total radiation to DC conversion efficiencies of electromagnetic energy harvesting systems, using vertical 3-dimensional stacked arrays

6. **Apply** the method in 5 to antennas, in addition to the proposed collector based on metamaterials proposed in 3

7. **Introduce** the concept of near unity electromagnetic energy harvesting using electrically small unit cells

8. **Introduce** the concept of near unity electromagnetic energy harvesting using electrically large unit cells

9. **Introduce** various channeling and power combining networks that can guide the collected energy to a single or multiple loads

10. **Examine** the feasibility of extending the concept in 7 and 8 to the infrared regime

1.7 Dissertation Outline

The remaining of this dissertation is outlined as follows:

Chapter 2 proposes a new and novel methodology: using metamaterial particles as electromagnetic energy harvesters instead of classical antennas. The chapter also provides numerical and experimental validations showing that an SRR array overpowers an array of antennas both placed in the same footprint area in terms of radiation to AC conversion efficiency.

Chapter 3 introduces the concept of perfect metamaterial absorption for electromagnetic energy harvesting. Unlike earlier designs of metamaterial

absorbers, here the power absorption is mostly dissipated across a resistive load instead of the dielectric substrate. This implies that near unity electromagnetic energy harvesting can be achieved.

Chapter 4 and 5 present a methodology to further increase the efficiency of the harvesting system per footprint area. This method utilizes the vertical space by stacking panels of energy collectors while maintaining the same 2-D foot print. Thus, the efficiency per footprint can be increased significantly. Two case studies investigate this concept using metamaterials and folded dipole antennas. In both cases, numerical and experimental results show that the efficiency of the 3-D system consisting of four stacked panels can be increased up to five times, as compared to a flat 2-D footprint.

Chapter 6 expands the concept of the near-unity efficiency of electrometric energy harvesting using electrically large elements. By using tightly coupled antennas where each unit cell is electrically large, simplified channeling methods and cost effective solutions can be achieved.

Chapter 7 presents the idea of a multi-polarized energy harvester. Using the concept of near unity electromagnetic energy harvesting, a metasurface is presented where each alternating unit cell is responsible of collecting the energy from a single polarization. In addition, a new channeling method is introduced. It uses the concept of a super cell where each super cell consists

of a number of sub unit cells.

Chapter 8 studies the feasibility of extending the concept of near unity energy harvesting to the infrared regime. Encouraging preliminary numerical results are presented, and open many avenues for possible future directions.

Finally, the accomplished work, list of publications, and possible future directions are summarized in Chapter 9.

Chapter 2

Electromagnetic Energy Harvesting Using Split Ring Resonators

2.1 Introduction

This chapter presents a novel collector based on metamaterial particles, that is to be used for electromagnetic energy harvesting. The proposed collector is formed by an array of Split Ring Resonators with a resistive load placed across the gap of each resonator to absorb the power from an incoming wave. Most importantly, the proposed metamaterial array is compared to previously used collectors (antennas) in terms of radiation to AC conversion efficiency. The simulated and measured results show the of metamaterial particles' effectiveness in scavenging the energy from microwaves efficiently.

2.2 Metamaterials and their Potential for Energy Harvesting

Metamaterials are typically formed by assembling electrically small resonators that take various shapes and compositions [73]. The fact that metamaterials can be engineered to produce an effective medium having simultaneously negative permeability and permittivity has ignited a number of unprecedented applications with various frequency bands, from acoustics [74, 75] to the visible regime [76, 77]. Such applications include cloaking [78,79], energy harvesting [59,60,63,64], negative index of refraction [80], perfect lensing [81], and perfect absorption [82].

One of the most common type of resonators used to build metamaterials is the SRR, which is made of single, multiple, concentric or parallel electrically small broken rings [83, 84]. In this chapter the focus is on SRRs as a building block for metamaterials, and other shapes will be proposed and investigated later on in subsequent chapters.

The fact that an SRR develops a relatively high electric field within its structure at resonance frequency, which implies a build up of voltage across its gap, is indicative of its ability to harvest electromagnetic energy. A single broken loop, such as an SRR element, can be realized as a simple

RLC circuit where the dimensions directly affect the overall inductance and capacitance of the SRR. Hence, by varying these dimensions, one can design an SRR to resonate at a specific frequency. At the resonant frequency, the SRR exhibits a concentration of electromagnetic energy, in which the magnetic field is significantly more dominant than the electric field. A detailed study of the effect of varying the mentioned parameters on the SRR resonance frequency can be found in [85, 86].

When an SRR is excited by a magnetic field normal to the plane of the SRR, a highly concentrated electric field develops across the gap of the structure, as indicated by the red color in Fig. 2.1 for a single ring SRR. Even if the incident field is incident at an angle to the normal, resonance can be excited in the SRR, leading to a concentration of electric field across the gap. Since the gap is electrically small, we can interpret the field buildup across the gap as a voltage. Effectively, the field-illuminated SRR becomes a voltage source.

An SRR cell was designed using the full-wave simulator ANSYS HFSS to resonate at around 5.8GHz. The designed SRR has dimensions of $l = 5.9$ mm, $w = 0.55$ mm and $g = 0.8$ mm, as shown in Fig. 2.1. Since the optimal resistance value is not known in advance, the input impedance at the gap of the SRR needs to be computed. To this end, the SRR was excited by

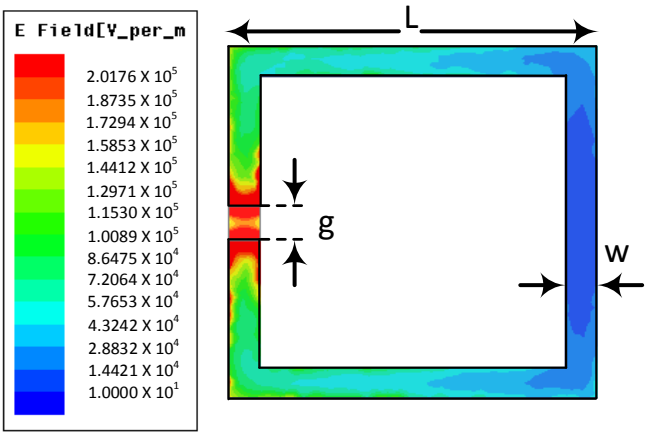

Figure 2.1: The distribution of the electric field on the plane of a single ring SRR, where the dark red color indicates high energy concentration in the gap of the SRR.

a source placed at the gap of the resonator. The input impedance of the resonator was extracted for a range of frequencies, as shown in Fig. 2.2. From Fig. 2.2(b), the impedance seen at the gap of the SRR at the resonance frequency is purely resistive, with a value of 14 kΩ. The SRR was then loaded with a resistor and excited by a plane wave such that the magnetic field is perpendicular to the SRR plane. It was found that maximum power dissipation across the resistive load occurs for a resistance value of 14 kΩ. This confirms that maximum power absorption occurs when the load is equal to the input resistance of the SRR. In the case of an SRR array, however, the mutual coupling between the cells significantly affects the in-

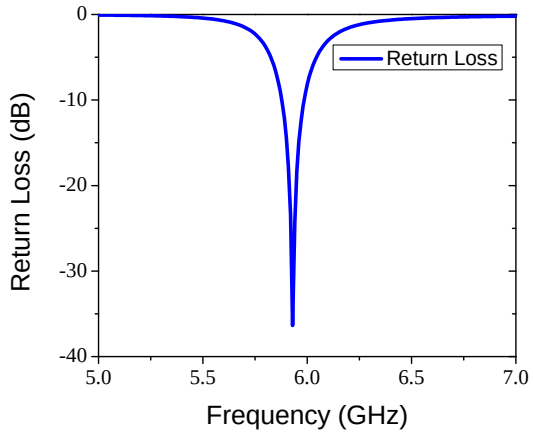

(a)

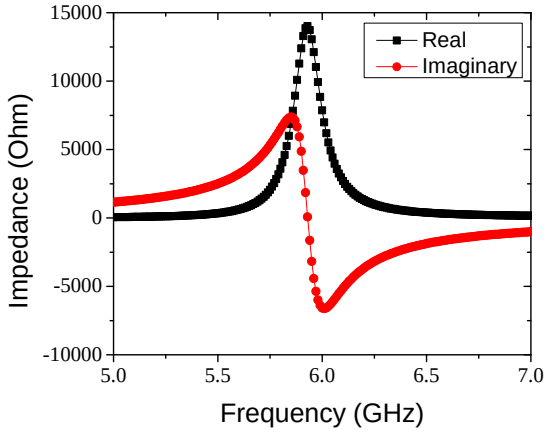

(b)

Figure 2.2: (a) Simulated reflection coefficient of a single SRR .(b) Simulated real and imaginary part of the input impedance of a single SRR fed by a voltage source at the gap.

put impedance of each SRR cell, and consequently, the optimal resistance for maximum power absorption also changes. Another factor that affects

mutual coupling is the relative orientation of the SRR cells. In [87], it was shown that orientation indeed affects overall efficiency. However, optimization of the overall efficiency with respect to the relative orientation of the SRR cells and their relative spacing is deferred to future work. In fact, in light of the input impedance analysis performed here, the resistance used in [59] could not have been optimal (for receiving maximum power) in any sense.

Since the emergence of metamaterials, and until very recently when the potential of harvesting electromagnetic energy using metamaterial particles was first introduced [59], metamaterials have never been analyzed for the reception of electromagnetic energy. In order to understand the feasibility of a single metamaterial cell, especially the SRR, to receive energy in the far field similar to classical antennas, the concept of reciprocity was revised.

Reciprocity states that for any two radiating elements in a certain medium, if a 1 Amp current source is placed across the feed nodes of either radiator and the voltage is recorded across the *open* circuit feed of the other radiator, then exchanging the current source and voltmeter produces the same reading (see for example, the discussion in [143]). A very simple numerical experiment is conducted in this section to show that even though the SRR is an electrically small resonator, it indeed follows the rules of reciprocity

and can therefore receive energy. To this end, we consider a dipole antenna and a single loop SRR, both resonating at the same frequency. The experiment is divided into four cases: For the first case, an SRR is excited by a current source placed across its gap, and then the voltage across the feed of the dipole antenna is recorded. In the second case, a dipole antenna is excited by a current source placed at its feed, then the voltage across the gap of the SRR is recorded as shown in Fig. 2.3 (a) and (b). The voltage of both cases is as $V = \mathbf{E} \cdot \mathbf{d}$, where $\mathbf{E}$ is the electric field at the feed and $\mathbf{d}$ is the gap length vector of the feed of each radiator. Simulation results give identical voltage readings for both cases. When a voltage source is used instead of a current source, as in Fig. 2.3 (c) and (d), different readings are obtained for the feed voltages.

This very simple numerical exercise shows conclusively that although SRRs might not be a suitable choice for transmitting antennas due to practical source considerations, they indeed can operate as receivers whose effectiveness can vary due to additional factors such as impedance matching and proximity to adjacent cells.

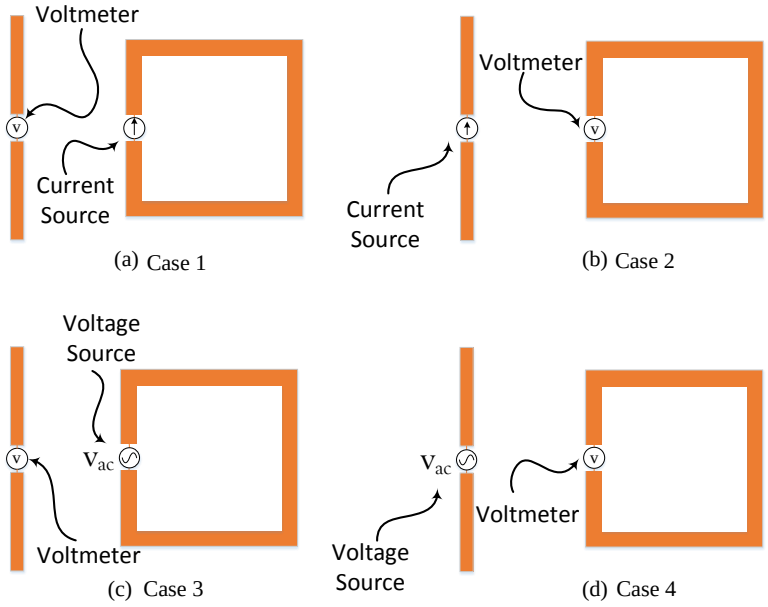

Figure 2.3: Simulation setup illustrating respectively, the reciprocity theorem for (a) case 1 , (b) case 2, (c) case 3 and (d) case 4, as described in the text. In each case, the relative size of the two radiators is not to scale.

2.3 Experimental Validation of a Single SRR as an Energy Harvester

To demonstrate the ability of a single SRR to pick up electromagnetic energy, an experiment was conducted for a single SRR having the dimensions stated above. The fabricated SRR was loaded with a resistor across the gap as shown in Fig. 2.4. The loaded resistor value used in the experiment was not necessarily the optimal resistance that will yield maximum power

absorption across the resistor. However, the goal of this experiment was to show the ability of the resonator to pick up electromagnetic energy regardless of the resistive load value used. In the experiment, a signal generator was used to excite a 19 dBi gain antenna array operating at the resonance frequency of 5.8 GHz. The SRR single cell was placed 30 cm away from the transmitting antenna such that the H-field was perpendicular to the plane of the SRR. The voltage across the resistive load was measured using an Agilent Infiniium 91304ADSA 12GHz oscilloscope equipped with a single-ended probe. It was found that the SRR loop was able to develop 611mV across the resistive load. This simple experiment proves the capability of an electrically small SRR to capture electromagnetic energy, indicating its potential to be used as an electromagnetic energy harvester [59].

2.4 The Equivalent Circuit and Input Impedance of SRRs

In the above numerical and experimental tests, the analysis focused on the AC power developed across the surface-mount resistor placed at the gap of the resonator. In a practical energy harvesting system, this resistor is replaced by a full rectification circuitry that is capable of converting AC

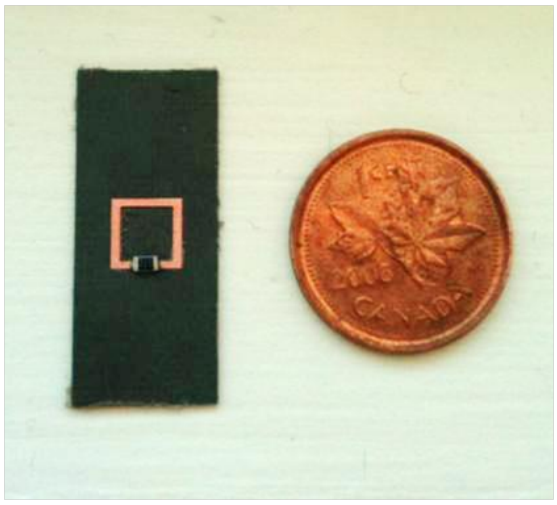

Figure 2.4: A picture showing the fabricated SRR loaded with a mount resistor across its gap.

power to DC, employing matching networks, diodes such as Schottky diodes, and a load. Designing such a rectification circuit depends on the SRR input impedance. The equivalent circuit model of a *receiving* single loop SRR is shown in Fig. 2.5, where R is the total resistance (radiation and Ohmic), L is the self inductance, and C represents the gap capacitance of the SRR. Here, it is assumed that the resonator is operating at resonance frequency while illuminated by an incident electromagnetic field. Notice that we have represented the voltage induced within the SRR (which is essentially part of the entire emf voltage induced by the arriving incident wave) as a dependent voltage source. Whether the dependent voltage source is current dependent or voltage dependent is not relevant here. What matters is that it is a

dependent voltage source that depends on the magnitude, polarization and frequency of the incident electromagnetic field.

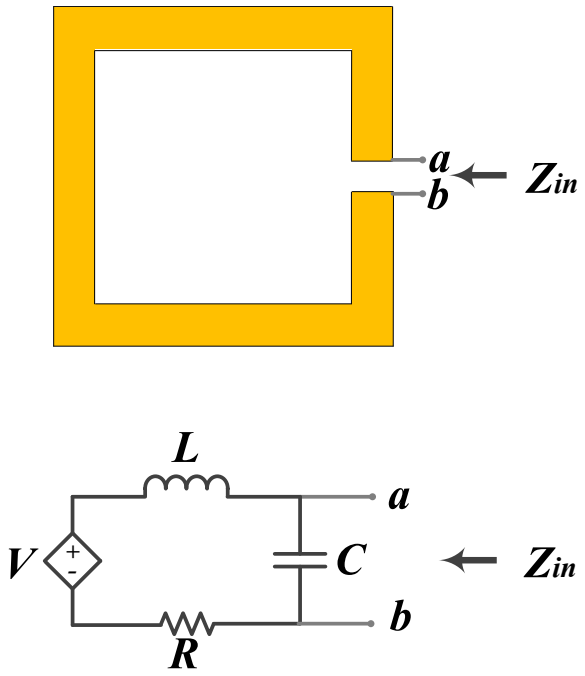

Figure 2.5: Equivalent circuit model of a single loop SRR.

In earlier works using SRRs as building blocks for metamaterials, the gap provided the capacitance needed for resonance. To harvest energy from an SRR through the gap, a resistive load needs to be placed across the gap. The optimal load resistance at the gap that will maximize power absorption depends on the topology of the SRR. Therefore, when designing a loaded SRR to operate at a specific frequency, the load resistance that can achieve maximum power transfer can be found through constrained optimization

by varying the resistance and selecting the resistance value that provides maximum power dissipation across the gap for a particular field polarization and angle of incidence. With reference to Fig. 2.2(b), it is interesting to note that a single square loop with a perimeter of $\lambda_o/2$ experiences high resistance at the resonance frequency. This occurs because, at this small loop size, the radiation resistance is much smaller than is the case when the perimeter size is slightly larger than a wavelength [88, 143]. Such high impedance (Kohms range) makes the process of matching and tapping the energy from the gap then channeling it to a diode for energy harvesting quite impractical.

However, when we stack highly resistive loops in such a way that each loop is close to adjacent loops, the input impedance is reduced dramatically to values that allow for integration of a practical matching network and other types of associated circuitries. (This change in the internal impedance of loops was also observed and accounted for in [89]). The input impedance can be controlled by changing the periodicity of the cells, the dimensions of the loop, and the dielectric material used to host the loops.

It is a common practice to design, analyse and optimize antennas in transmitting mode. The same antenna can then be used in the receiving mode while retaining the same properties, due to the reciprocal behaviour

of antennas. This assumption is acceptable to some extent for a single isolated antenna [90]. However, when an array of antennas is used in the receiving mode, the transmitting mode analysis is no longer valid due to the difference in the mutual coupling between the transmitting and receiving modes. The work presented in a series of papers by Hui et al. [91–95] highlighted a methodology to compensate for the mutual coupling in the receiving mode for an array of antennas. This mutual coupling reduction is critical for various applications in the field of telecommunications, as mutual coupling will degrade system performance [96,97]. However, for energy harvesting, such coupling can be advantageous, reducing the input impedance of each unit cell, which enables the integration of rectification circuity and a matching network. In the next chapter, this coupling is utilized to tune the medium parameters (ϵ *and* μ), producing a surface that is matched to the free space impedance, which enables full absorption of an incident electromagnetic wave within the metasurface. What is relevant to this chapter, however, is that the input impedance of each cell will depend not only in its self impedance but also on the mutual impedance of the surrounding cells. More importantly, this mutual impedance differs between the transmitting and receiving modes. In particular, the cells in metamaterials are tightly coupled, which makes the effects of mutual coupling more pronounced.

To illustrate the effect of mutual coupling on the impedance of metamaterial cells in both the transmitting and receiving modes, three different scenarios where studied numerically using CST Microwave Studio, as shown in Fig. 2.6. In each scenario the proposed unit cell or array of cells was tested in both the transmitting and receiving modes to gain an understanding of the input impedance in both modes.

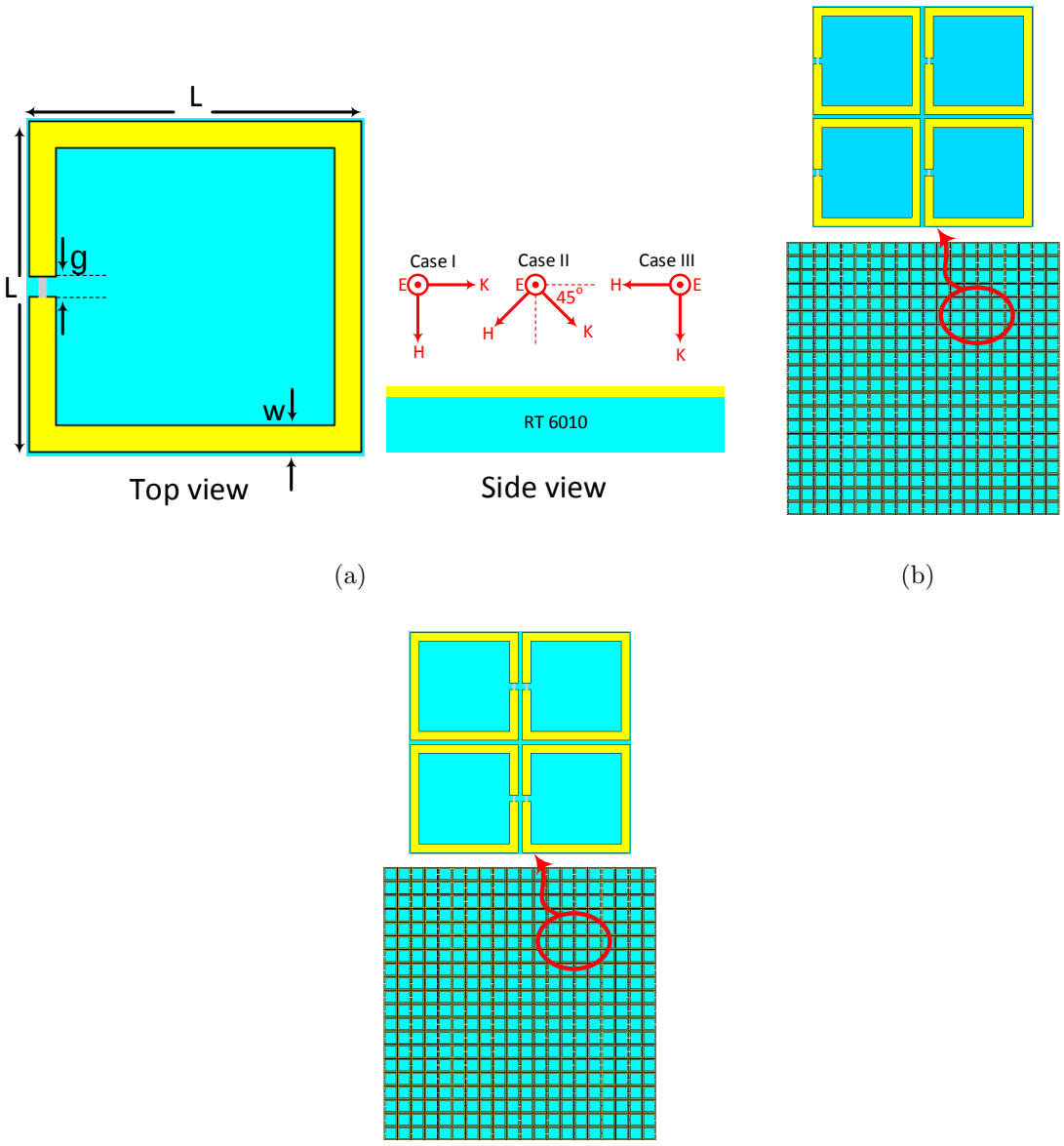

(a) (b)

(c)

Figure 2.6: A schematics showing the three proposed scenarios as explained in the text, where the sub-figures refer to (a) scenario 1, (b) scenario 2, and (c) scenario 3. The three cases for incident field polarization are shown in (a).

The first scenario investigates the input impedance of a single loop SRR isolated in free space. In the simulation, the SRR was placed on top of an RT6010 Rogers substrate material having a dielectric constant of $\epsilon_r = 10.2$ and substrate height of 2.54 mm. With reference to Fig. 2.6(a), the SRR has dimensions of $l = 5$ mm, $w = 0.8$ mm and $g = 0.3$ mm. In the transmitting mode, a voltage source was placed across the gap of the SRR, and the reflection coefficient along with the input impendence of the SRR looking into the gap of the SRR resonator was computed as shown in Fig. 2.7.

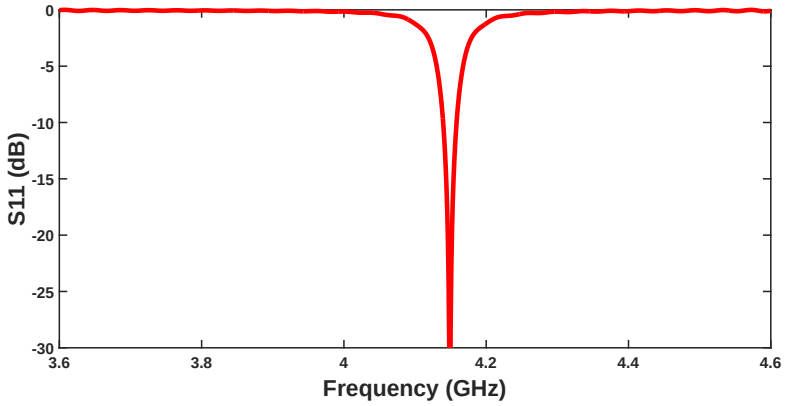

(a)

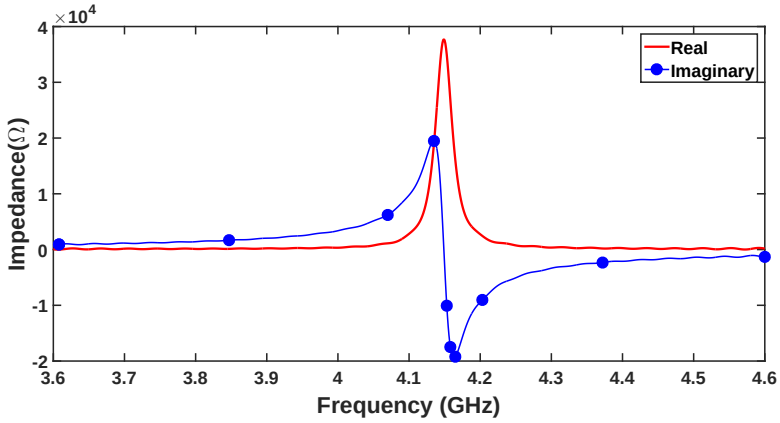

(b)

Figure 2.7: Simulation results for the transmitting mode of scenario 1 showing the (a) reflection coefficient, and (b) real and imaginary part of the input impedance of a single SRR fed by a voltage source at the gap.

It is clear from the results that the SRR has an input impedance of $R = 37.5\ k\Omega$, and when the SRR is excited by a voltage source having

a source impedance of $R = 37.5\ k\Omega$, a good impedance match can be achieved between the source and the SRR. This well matched condition is indicated by the reflection coefficient curve, which has a dip of -30 dB at the resonance frequency of 4.15 GHz, as shown in 2.7(b). Although the source impedance is impractical with such a high impedance, it was used here strictly for matching purposes, illustrating the reflected voltage seen from the gap of the SRR when the source impedance is matched to that of the input impedance of the SRR loop.

The same SRR loop was then analysed in reception mode, with a variable resistor placed across the gap of the resonator. The SRR was excited by a plane wave with three polarizations, as shown in 2.6(a). Plots of the received power with a sweep of different resistance values for all the proposed three polarizations are shown in 2.8. From the power curves, it is evident that the maximum power received for all polarizations occurs when the SRR is terminated by a resistance value of $R = 37.5\ k\Omega$ which is the same as the input resistance value obtained in the transmitting mode. This finding shows that, for a single isolated SRR, the input impedance is identical in both the transmit and receive modes. It also indicates that one can use the transmitting mode analysis to design a single isolated antenna in general.

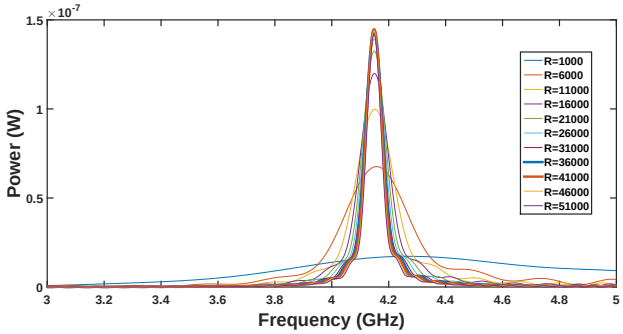

(a)

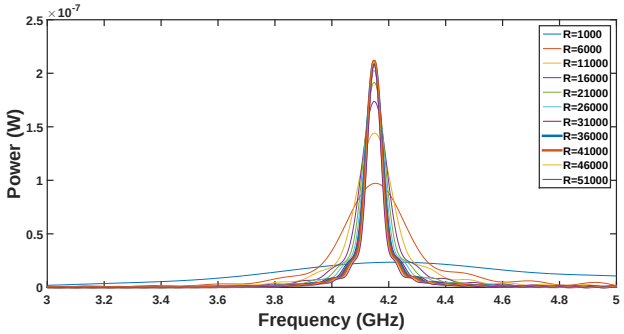

(b)

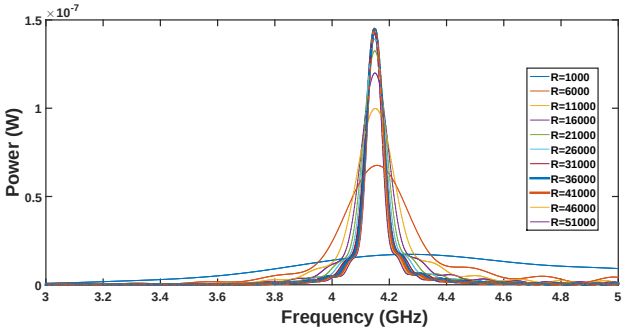

(c)

Figure 2.8: Simulation results for scenario 1 showing the power received as a function of frequency with a variable resistor varying from $R = 1\ k\Omega$ to $R = 50\ k\Omega$ for (a) Case 1, (b) Case 2, and (c) Case 3, respectively. The three cases refer to different incident field polarizations, as illustrated in 2.6(a).

The second scenario studies an array of 20 $\times$ 20 SRRs (please see Fig. 2.6(b)), in which each SRR has the same dimensions as the one described in scenario 1, with a spacing between adjacent unit cells of 0.2 mm . The SRR unit cell located at the center of the array was excited by a voltage source with an impedance of $R = 1.3\ k\Omega$, whereas the other SRRs were terminated by the same resistance of $R = 1.3\ k\Omega$. Here, the resistance value was found iteratively through a series of numerical simulations since the input impedance is not simply the impedance of the middle SRR loop only but rather a complex impedance that depends on the mutual coupling among all the cells in the array. Figure 2.9 shows the input impedance and the reflection coefficient looking into the middle SRR loop. From the results, we can be sure that the SRR is well matched to the source when the source resistance is $R = 1.3\ k\Omega$ at the resonance frequency of 2.55 GHz .

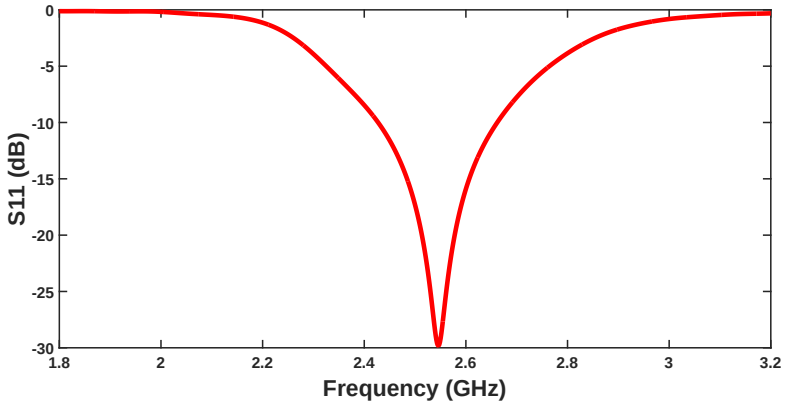

(a)

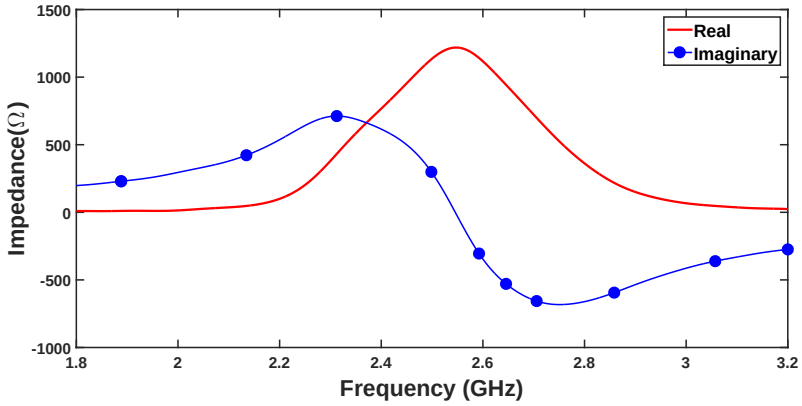

(b)

Figure 2.9: Simulation results for the transmitting mode of scenario 2, showing the (a) reflection coefficient, and (b) the real and imaginary parts of the input impedance of the middle SRR cell fed by a voltage source at the gap. The other SRR cells in the array were terminated by a load resistance of $R = 1.3\ k\Omega$.

The same array was then tested in reception mode by terminating all the

SRRs in the array with the same impedance obtained in the transmitting mode, with the exception that the middle cell is terminated by a variable resistor varying from $200\Omega - 2.6\ k\Omega$. The main goal of this particular numerical test was to see if the SRR would still possess the same input impedance in both the transmit and receive modes while surrounded by tightly coupled SRRs. Similarly, the incident wave was varied with the three proposed cases as shown in 2.6(a). Interestingly, the maximum power received was when the middle SRR cell was terminated by $R = 400\ \Omega$, $R = 400\ \Omega$ and $R = 1400\ \Omega$ for the three incident wave polarizations, respectively, as shown in Fig. 2.10. This finding is different from what we achieved in the transmitting mode. In addition, the maximum power was received at a frequency of 1.89 GHz for case 1 and case 2, and at 2.1 GHz for case 3, both frequencies differing from the resonance frequency found through transmitting mode analysis.

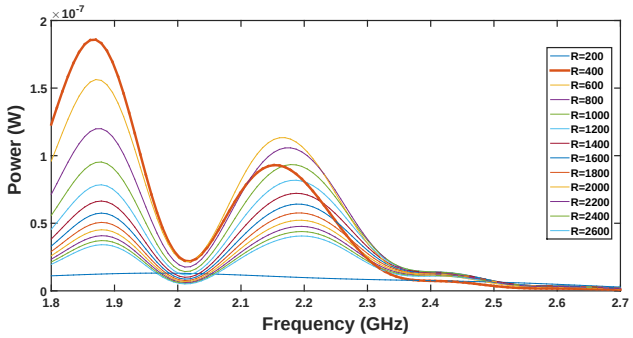

(a)

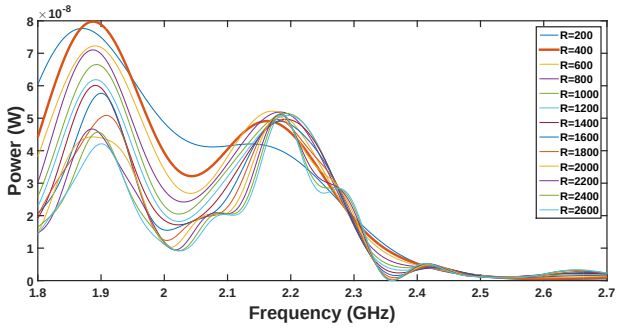

(b)

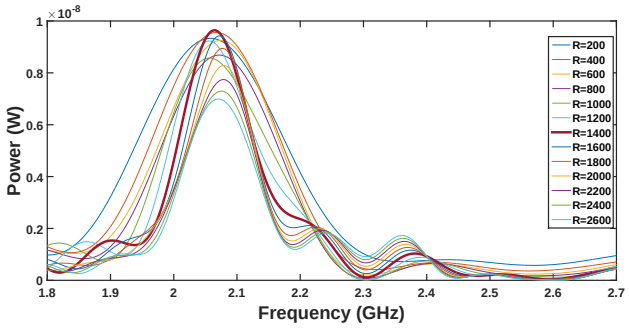

(c)

Figure 2.10: Simulation results for scenario 2 showing the power received as a function of frequency with a variable resistor varying from $R = 200\ \Omega$ to $R = 2.6\ k\Omega$ for (a) Case 1, (b) Case 2, and (c) Case 3, respectively. The three cases refer to different incident field polarizations, as illustrated in 2.6(a).

The last scenario experiments with an array of 20 $\times$ 20 SRRs, similar to the one used in scenario 2 except that the SRRs are back to back as shown in Fig. 2.6(c). Similarly, the SRR located in the middle of the array was excited in the transmitting mode by placing a voltage source with the matched impedance of $R = 400\ \Omega$. The reflection coefficient and the input impedance of scenario 3 (please see Fig. 2.11) shows that the middle cell is well matched at the resonance frequency of 3.7 GHz.

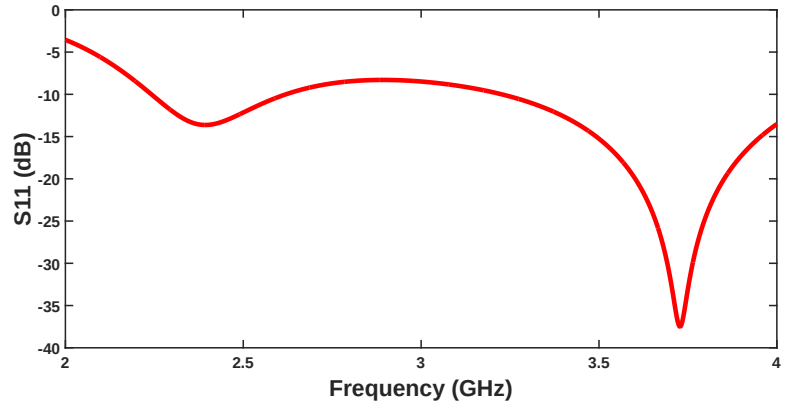

(a)

(a)

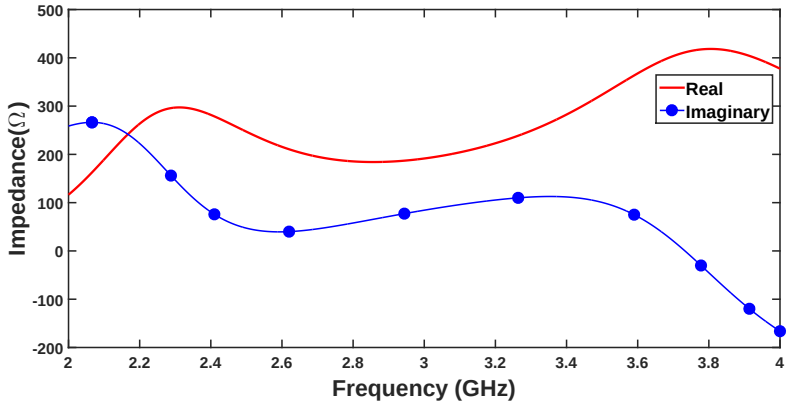

(b)

(b)

Figure 2.11: Simulation results for the transmitting mode of scenario 3, showing the (a) reflection coefficient, and (b) real and imaginary part of the input impedance of the middle SRR cell fed by a voltage source at the gap while the other SRR cells in the array were terminated by a load resistance of $R = 1.3\ k\Omega$.

The middle cell was then excited by a planewave, and the power across a

variable resistor (varied between $R = 200\ \Omega$ and $R = 1.4\ k\Omega$) placed across the gap was recorded for a sweep of frequencies using the three proposed polarizations. The maximum power occurred at resistance values different from the one obtained in the transmitting mode: $R = 200\ \Omega$, $R = 200\ \Omega$ and $R = 100\ \Omega$ for the three polarizations, respectively, as shown in Fig. 2.12. In addition, the peaks of the received power for all three, cases were 4.7 GHz, 5.6 GHz and 2.7 GHz, respectively. Both the optimal resistance value and the frequency where the peak occurs differ from those obtained in the transmitting mode.

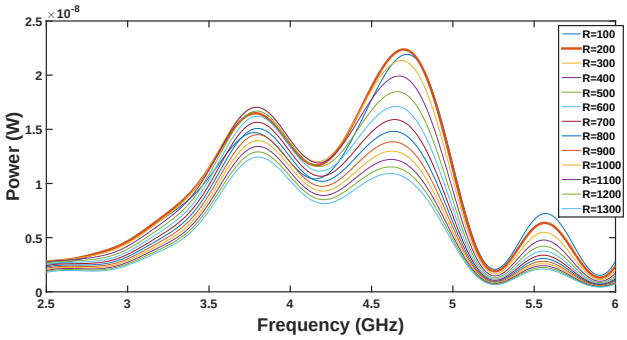

(a)

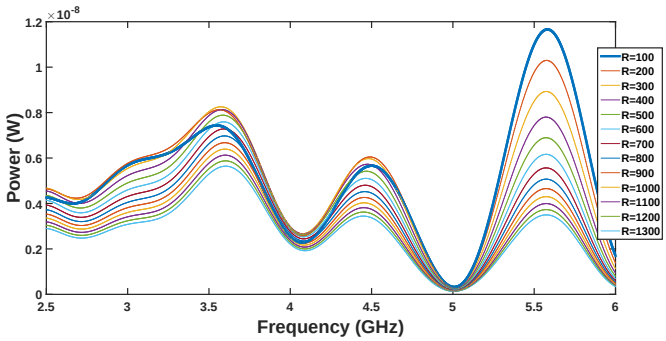

(b)

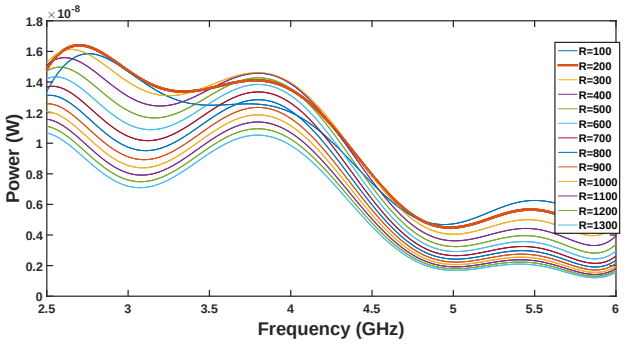

(c)

Figure 2.12: Simulation results of scenario 3 showing the power received as a function of frequency with a variable resistor varying from $R = 200\ \Omega$ to $R = 1.4\ k\Omega$ for (a) Case 1, (b) Case 2, and (c) Case 3, respectively. The three cases refer to different incident field polarizations, as illustrated in 2.6(a).

From the above simulations we can conclude that the reciprocity in regards to the input impedance of radiators holds only for an isolated radiator, as was observed in scenario 1. However, when an array of cells is used, the input impedance will no longer obey the reciprocity rule, and the array must be freshly designed independent from the transmitting mode analysis. In addition, the orientation of the cells can be changed to alter the input impedance as desired, as was observed in scenario 3.

In section 2.6, we show that by stacking 12 $\times$ 12 SRR loops, one can significantly reduce the input impedance of each cell to 150 Ω or another desired value by varying the distance among the SRR cells.

2.5 SRR Array vs. Patch Antenna Array

Before we can incorporate SRRs as energy collectors with rectenna systems, their performance must be compared to current energy collectors (i.e;patch antennas) in terms of radiation to AC conversion efficiency. Considering the efficiency definition introduced in [59], a demonstration is presented comparing the efficiency of an array of SRRs with that of an array of patch antennas, both placed on the same footprint, as shown in Fig. 2.13. The array of SRRs contained 81 SRR elements, all of identical size and designed

to resonate at around 5.85 GHz. An array of 3×3 identical patch antennas was placed on the same footprint, each resonating at the same frequency of 5.85 GHz. Both the SRR array and the patch antenna array were placed on top of a Rogers RT/duroid 5880 substrate having a dielectric constant of $\epsilon_r = 2.2$, loss tangent of 0.0009 and substrate thickness of $t = 0.787\ mm$. The total footprint area was $85 \times 85\ mm^2$.

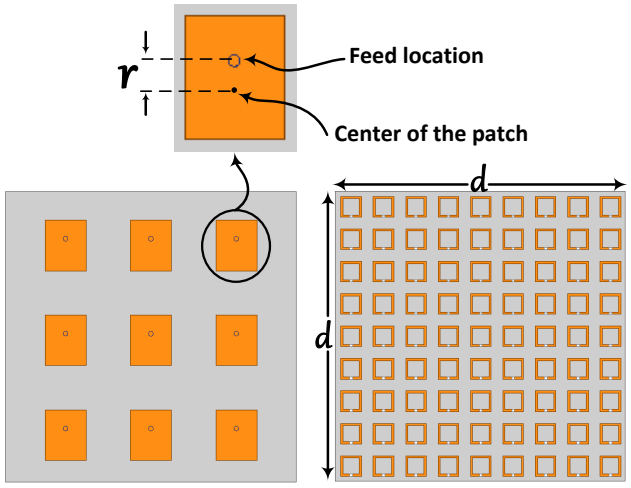

Figure 2.13: a 9×9 SRR array and a 3×3 patch antenna array occupying the same footprint.

To ensure that the footprint is utilized efficiently by the patch antennas, the maximum number of antennas that can be placed on the defined footprint while being able to deliver maximum power to the loads is studied. In other words, how many antennas can be placed on a defined footprint so

that the sum of the power developed across each load is maximum. In addition, each antenna must be terminated by a load that is equal to the input impedance of the patch antenna to ensure maximum power delivery to each load. Therefore, two essential numerical experiments were conducted.

First a patch antenna operating in the receiving mode was designed to resonate at around 5.8 GHz. The patch antenna has dimensions of width $x = 12\ mm$ and length $y = 14.8\ mm$ as showing in Fig. 2.13. The patch was excited by a horn antenna placed a distance of 120 cm away from it to ensure a plane wave excitation in close proximity of the patch antenna. The patch antenna was terminated by a coaxial line having an input impedance of 50Ω. The performance of a probe-fed patch antenna in terms of power collection efficiency is strongly dependent on the feed position. Hence, the feed position was analysed by varying the location of the coax with a distance r (see Fig. 2.13). Fig. 2.14 shows that the best performance of an isolated patch antenna was achieved when the probe was placed a distance of 2 mm away from the center of the antenna. Therefore, the optimal coax probe feed position was selected for all the patch antennas populating the footprint.

The second numerical experiment studies the maximum number (N) of antennas that can be placed on the defined footprint in such away that the

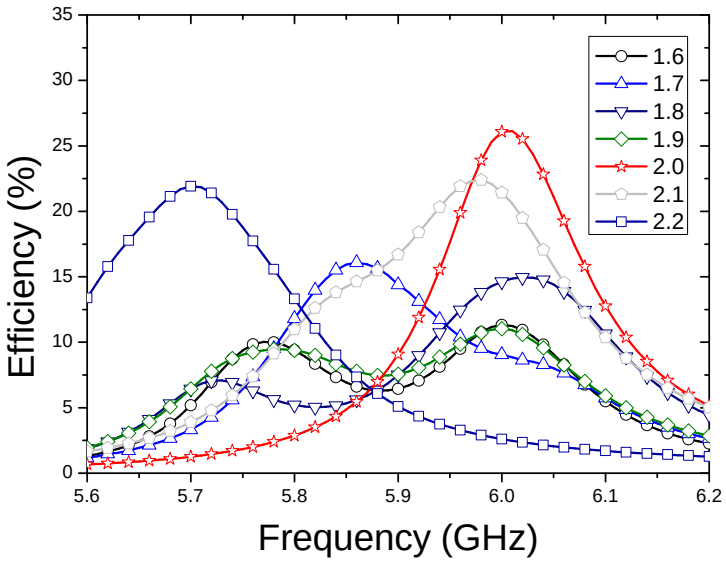

Figure 2.14: The efficiency of the patch antenna with different coax position (r) with reference to Fig. 2.13.

total power collected by the N antennas is maximum. We emphasize that our choice for the feed location for the patch antennas and the number of antennas was selected by inspecting a number of possible solutions with the goal of maximizing power collection across the loads of the antennas and then the best case was chosen. When antennas are placed in close proximity to each other, they interact, introducing mutual coupling, which in turn changes the current in the antenna from that if the antenna was isolated in free space. Mutual coupling changes the input impedance of the antennas and can affect their efficiency in both the receiving and transmitting

modes [98]. Typically, antennas need to be separated by approximately at least 1/2 of the free-space wavelength to retain their independent characteristics such as efficiency, radiation pattern and gain [99]. Five different configurations were studied to achieve maximum power reception. The possible configurations were limited by an a priori specified footprint. In each case, the antennas were placed in such a way that the distance between two adjacent antennas was maximized to reduce coupling and to achieve maximum power collection by each antenna. The five cases are shown in Fig. 2.15. The number of antennas were varied between 4 and 9. It was found through numerical simulation that the antenna configuration containing 9 antennas (see Fig. 2.16) resulted in the maximum power efficiency, and therefore was selected for comparison with the SRR array. Different from patch antennas, the coupling among SRR cells is very critical to the total amount of power absorbed by the SRR array. In addition, the distance between two adjacent SRRs indicated by the separation s in Fig. 2.21 plays a key role in controlling the input impedance of each SRR. This can be clearly understood by comparing the input impedance of a single SRR (14 kΩ) and an array of SRRs (150 Ω) as shown in Fig. 2.2(b) and Fig. 2.21 respectively. Therefore, the SRRs were densely stacked in the available footprint to maximize the absorbed power.

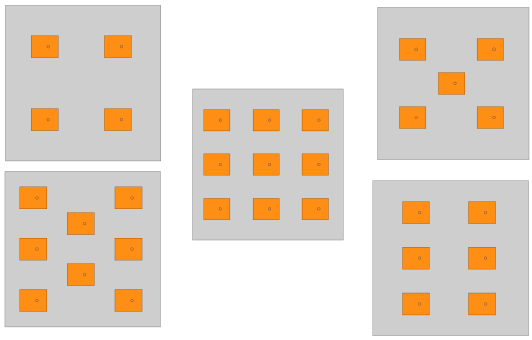

Figure 2.15: Various patch antenna array configurations.

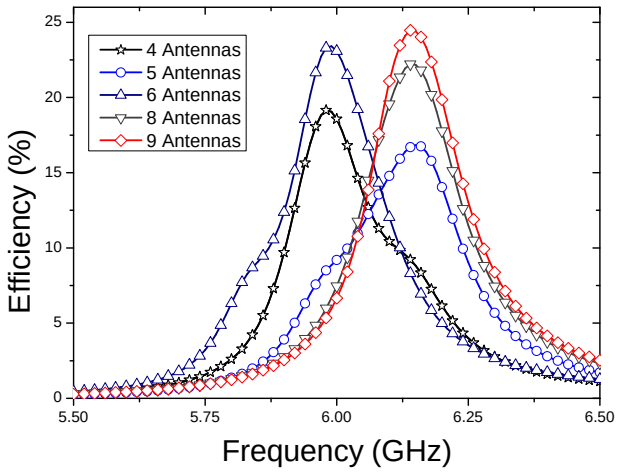

Figure 2.16: Energy harvesting efficiency of 4, 5, 6, 8, and 9 antenna array.

The efficiency performance of the 3 $\times$ 3 antenna array is compared to a 9 $\times$ 9 SRR array. The SRR array was made of SRR cells having the same dimensions as discussed above and with cell spacing of 3.5mm. For this particular spacing and total number of cells, a load resistance of 2.1 kΩ gave maximum efficiency. Each array is excited by a horn antenna placed

a distance of 120 cm away from the array to ensure that a plane wave is incident on the array (this type of excitation is the basis used for all the array simulations discussed in this section). The SRR receives maximum power when the H-field is normal to the plane of the SRR which is not the case for the patch antenna. Therefore, for a fair comparison, three tests were conducted for each array with incident field angles of 30°, 45°, and 60° (see Fig. 2.17 for the incident angle definition). The angle ϕ is measured with respect to the x-axis, as indicated in Fig. 2.17. Figures 2.18, 2.19, and 2.20 show the efficiency of the antenna array and the SRR array for incidence angles of 30°, 45°, and 60°, respectively. Table 2.1 summarizes the numerical simulation results. In the table, the bandwidth was calculated by considering the range of frequencies where the efficiency exceeds 40% and 10% for the SRR array and antenna array respectively.

From the results obtained the following observations can be drawn:

- The SRR array resulted in higher efficiency for all the incident field angles selected;
- The bandwidth of the SRR array is significantly wider than that of the patch antenna array. More specifically, the SRR array resulted in a bandwidth up to 3.10 GHz over which the efficiency exceeds 40% while the antenna array resulted in a bandwidth of only 450 MHz over which

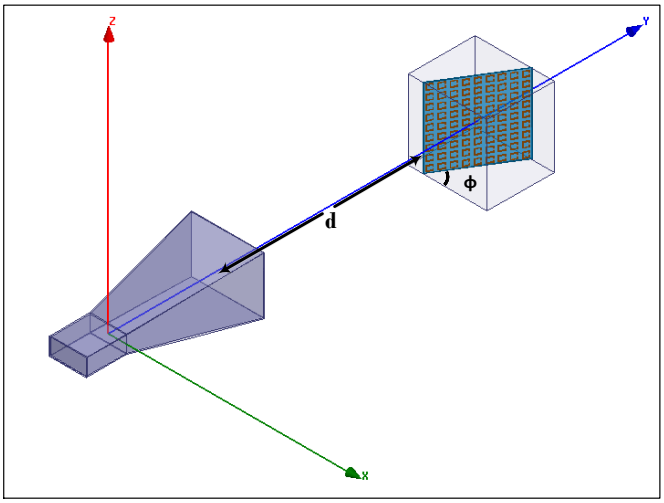

Figure 2.17: Numerical simulation setup for energy harvesting using a horn antenna as the source of radiation and an SRR array as the collector.

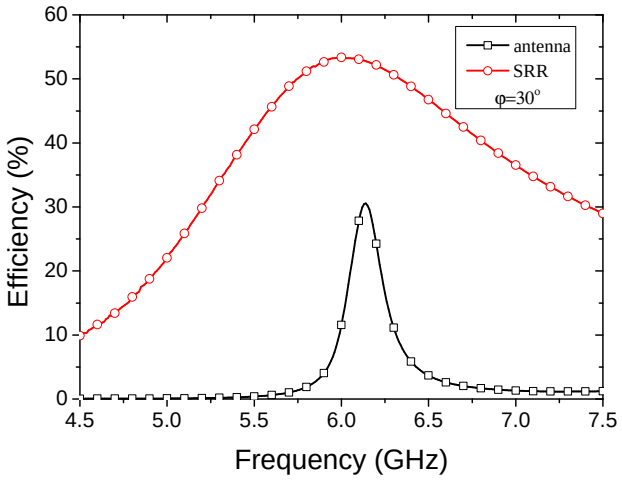

Figure 2.18: Energy harvesting efficiency of the 9×9 SRR array vs. a 3×3 patch antenna array both tilted at 30°.

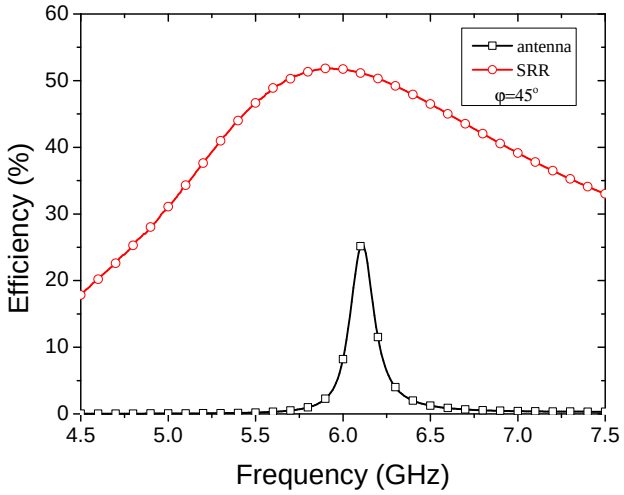

Figure 2.19: Energy harvesting efficiency of the 9×9 SRR array vs. a 3×3 patch antenna array both tilted at 45°.

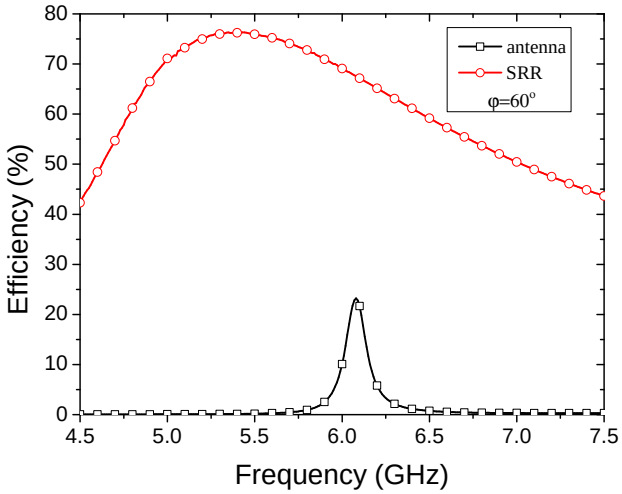

Figure 2.20: Energy harvesting efficiency of the 9×9 SRR array vs. a 3×3 patch antenna array both tilted at 60°.

Table 2.1: The performance of the SRR array as compared to the Antenna array

Collector Type	*Incident Angle*	*Max Efficency* (%)	*Bandwidth* (GHz)
SRR Array	30°	53.37	1.40
	45°	51.84	1.65
	60°	76.31	3.10
Antenna Array	30°	30.56	0.45
	45°	25.52	0.25
	60°	23.21	0.20

the efficiency exceeds 10%.

- For SRRs, the coupling between adjacent elements has a constructive effect of the total bandwidth of the collected power since the bandwidth of a single SRR (Fig. 2.2(a)) is only 200 MHz while the bandwidth of the SRR array has expanded to around 3.10 GHz.

2.6 Experimental Verification

In this work, the objective is to continue demonstrating the effectiveness of metamaterial arrays for converting the field energy into available AC power. Experimentally validating the precise structure considered above

is especially time consuming since the voltage needs to be probed at each SRR gap while sweeping over some range of frequencies. Here, we consider a single patch antenna and compare its energy harvesting performance with an array of SRR cells placed on the same footprint of the patch antenna. The patch antenna and the SRR array were redesigned to operate at 3 GHz. (Our choice of 3 GHz was purely due to the constraints of available test equipment). First a single square patch antenna with a side $a = 25.1$ mm was designed to resonate at 3 GHz as shown in Fig. 2.21. The patch antenna was placed on top of a grounded RO4350 substrate having a thickness of $t = 1.524$ mm, a dielectric constant of $\epsilon_r = 3.66$ and a footprint area of 60 $\times$ 60 mm^2. Then the same footprint was used to populate an array of 12 $\times$ 12 SRRs with each cell having dimensions of $l = 4.7$ mm, $w = 0.6$ mm and $g = 0.5$ mm (for SRR dimensions, see Fig. 2.1). The SRRs were separated by a distance of $s = 0.3$ mm as shown in Fig. 2.21. The SRR array was hosted by a 2.54mm thick TMM10i substrate with a dielectric constant of $\epsilon_r = 9.9$. The substrate type for both the patch antenna and the SRR array was selected to optimize the performance of each structure.

Then the single patch antenna and the SRR array were fabricated and terminated with the matched impedance as shown in Fig. 2.22. A 150 Ω surface mount resistor was placed across the gap of each SRR cell and 50 Ω

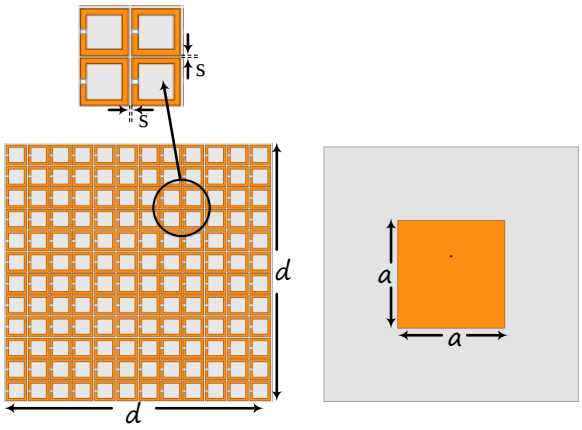

Figure 2.21: a 12 × 12 SRR array and a single patch antenna occupying the same footprint.

surface mount resistor was placed between a via soldered to the patch and the ground plane.

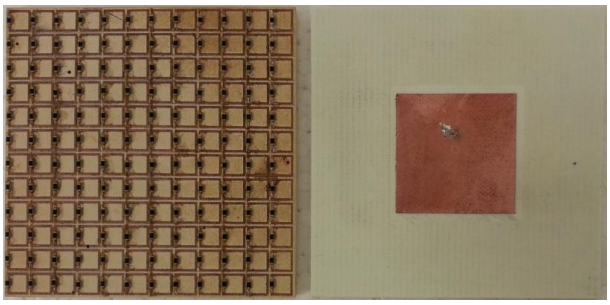

Figure 2.22: A photo showing the fabricated SRR array and the patch antenna both occupying the same footprint and loaded with the matched resistive load.

Using a commercially available 12 dB gain horn antenna, an incident field was generated having a center frequency of 3 GHz. Then the fabricated SRR array was placed a distance of 1 m away from the horn antenna to ensure a

Table 2.2: The measured output power captured by the patch antenna and the SRR array

Collector Type	*Frequncy* (GHz)	*PowerRecieved* (mW)
SRR Array	2.5	1.16
	2.75	1.29
	2.8	1.28
	3	1.07
Single Patch	2.9	0.43
	3.05	0.76
	3.10	0.74
	3.15	0.34

plane wave excitation as shown in Fig. 2.23. The SRR array was positioned such that the H-field is normal to the plane of the array. A 4 GHz Rohde and Schwarz RTO Digital Oscilloscopes equipped with a differential probe was used to record the voltage across each resistive load. It was found that the SRR was able to absorber 1.29 mW of the incident field at 2.75 GHz as shown in Table 2.2. The power collected by the SRR array in Table 2.2 was calculated by summing the measured power absorbed across the resistors of all 144 SRR cells at a certain frequency. The slight deviation of the resonance frequency is attributed to fabrication error. Similarly, the patch antenna was excited with the same setup except that the patch antenna was

positioned so that the E-field is parallel to the patch surface. It was found that the patch was capable of capturing a maximum power of 0.76 mW as indicated by Table 2.2. The type of field excitation was chosen such that both structures experience maximum incident field absorption. It is evident from the experimental results that the SRR is capable of absorbing more power per footprint when comparison to the patch antenna. In fact, the results show 70% improvement of the harvested power when using SRRs.

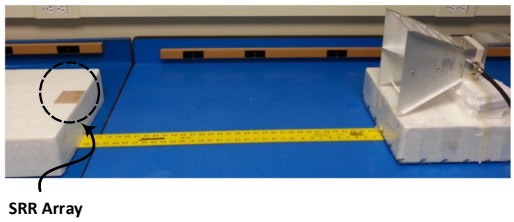

Figure 2.23: A photo showing the experimental setup used for both the SRR array and the patch antenna.

2.7 Conclusion

The feasibility of using SRRs to harvest microwave energy was studied through simulation by first placing a resistive load across the gap of a single loop SRR then calculating the power dissipated across the resistor. An experiment was then conducted to test the feasibility of SRRs to harvest microwave energy. The fabricated SRR cell was excited by an antenna placed

30 cm away, and then the voltage across the gap was measured using a high-frequency oscilloscope. A voltage of 611 mV was observed across the gap when 24 dbm power level was pumped into the transmitting antenna feed.

The efficiency of an array of SRRs was compared to that of an array of antennas occupying the same footprint. The numerical simulation results show that the SRR array is capable of electromagnetic energy harvesting efficiency of 40% or higher over a bandwidth of 3.10 GHz while the patch antenna array gave an efficiency of 10% or higher over a bandwidth of only 450 MHz. While we provided comparison to an array of patch microstrip antennas, other types of patch antennas could provide lower or possibly higher efficiency than the microstrip antenna array used here. It is evident from the numerical simulations presented that the SRR array provides significantly higher power harvesting efficiency and more critically wider bandwidth as compared to the antenna array. As a proof of concept, a single patch antenna and a 12 $\times$ 12 SRR array were compared in terms of maximum power output captured by each structure. It was found that the SRR array provided 60% more power per footprint than the patch antenna which verify the results obtained through numerical simulation. These results are expected to have strong impact on the viability and efficiency of

electromagnetic energy harvesting in general.

In the next chapters, a method to further increase the efficiency of the electromagnetic energy harvesting system is presented based on the perfect metamaterial absorption and vertical array stacking concepts.

Chapter 3

Electromagnetic Energy Harvesting Using Perfect Metamaterial Absorbers

3.1 Introduction

Metamaterials can be tailored to produce media that neither reflects nor transmits any power, thus enabling full absorption of incident waves at a specific range of frequencies and polarization [82]. A single unit cell of a metamaterial absorber typically contains a metallic inclusion and a dielectric substrate backed by a ground plane. Theoretically, full absorption can be achieved by tuning ϵ and μ such that the impedance of the metama-

terial is matched to the impedance of free-space. In addition to the perfect matched condition, introducing a loss in the medium along with a ground plane thicker than the skin depth of the wave increases the absorption further. Previous studies demonstrated various metamaterial absorber designs operating from the microwave [82] to the optical regime [100] with a number of features such as polarization independence [101], wideband [102,103], multiband [104] and ultrathin absorbers [105].

The fact that metamaterial absorbers are able to trap all the energy that impinges on its surface at a specific or range of frequencies is indicative of its ability to be used for energy harvesting. However, a critical distinction between metamaterial absorbers [82, 100–106] and metamaterial harvesters [59, 60, 63] is that metamaterial harvesters require not only full absorption but also maximum power delivery to a load to ensure that the absorbed power is dissipated across the load. Most of the previous metamaterial absorber designs show that a lossy dielectric substrate is an indispensable part of a metamaterial absorber [82,107], making it the main constituent responsible for dissipating the absorbed power. A number of articles have studied the integration of lumped ports into metamaterial absorbers; however these lumped ports aid in the process of absorption since the total absorbed power is mainly dissipated collectively between the

lumped ports and the lossy substrate [108, 109]. In recent works, a low loss dielectric substrate was used to design metamaterial absorbers for different applications. In [110, 111] an 11×11 metamaterial array with a low loss dielectric substrate was used as a metamaterial detector. A teflon-based low loss dielectric substrate was used in [112] to produce a flexible and elastic metamaterial absorber.

In this chapter, the design of a metamaterial harvester slab operating in the microwave regime based on an array of ELC (Electric-Inductive-Capacitive) resonators [113], that are capable of not only high absorption but also channeling almost all the absorbed power to a resistive load, is presented. The resistive load is a simple model for the input impedance of a rectification circuit which can be attached to each cell at its port as done in numerous works presented in the literature under rectenna systems (see [1, 34, 35, 38] and references therein).The emphasize that I present here is focused on maximizing the Radiation to AC conversion efficiency. Later in this thesis, I will touch upon other designs that focus in maximizing the Radiation to DC efficiency to form a full rectenna system.

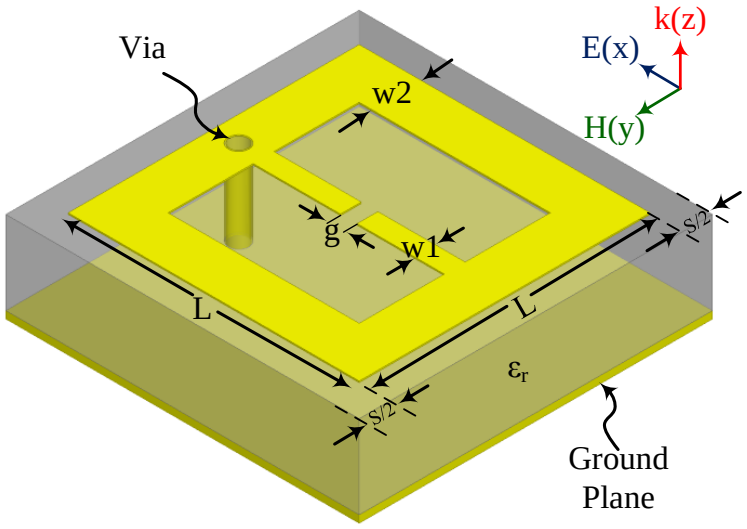

Figure 3.1: A schematic showing the proposed unit cell of a metamaterial harvester.

3.2 Design Methodology

A unit cell of the proposed energy harvesting media is shown in Fig. 3.1. It comprises two face-to-face split rings sharing the same gap, a dielectric substrate, a ground plane and a load connected between the top and bottom conductive layers through a via. The cell was designed to operate at 3 GHz with dimensions of $L = 7\ mm$, $g = 0.4\ mm$, $w1 = 0.5\ mm$, $w2 = 1.2\ mm$, $s = 0.5\ mm$ and copper thickness of $t = 35\ \mu m$. To minimize the dielectric loss, the unit cell was hosted on top of a 2.54 mm thick Rogers TMM10i dielectric substrate having a loss tangent of $tan\delta = 0.002$ and a dielectric constant of $\epsilon_r = 9.9$. A resistor was placed in shunt through a via to mimic

a load which can be replaced by a rectification circuit, having an input impedance matched to that of the unit cell at the center frequency of the operation band.

Using the electromagnetic full-wave simulator ANSYS® HFSS™, the unit cell was placed in a waveguide with Perfect Magnetic ($x-z$ plane) and Perfect Electric ($y-z$ plane) walls (see Fig. 3.1) to realize TEM mode excitation with polarization, as shown in Fig. 3.1. This particular boundary condition was chosen due to the electric symmetry in the constant x- and y-planes, which the unit cell exhibits. Both the position of the via and the resistance of the load were optimized to achieve maximum power delivery to the load, while maintaining full absorption of the unit cell. Using the scattering parameters, the absorption of the unit cell is expressed by $A(\omega)$=1-$|S_{11}|^2$-$|S_{21}|^2$. Figure 3.2 shows that the cell experiences full absorption at the designed frequency of 3 GHz. In addition, the optimal resistance value that corresponds to maximum power delivery to the load was found to be 82 Ω. It is interesting to note, that the input impedance of the cell (82 Ω) and the absorption of the metamaterial media are strongly affected by the periodicity of the cell. The space between adjacent cells, s, (see Fig. 3.1) can be varied to control the coupling among the cells and hence the input impedance of the metamaterial cell.

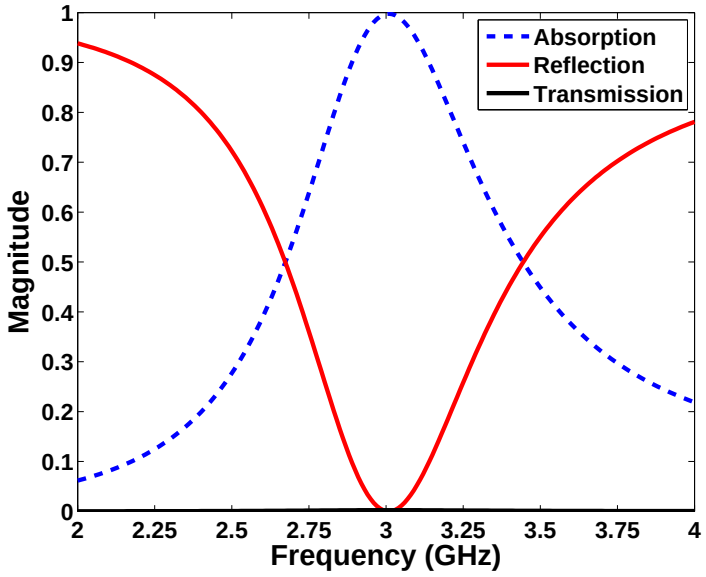

Figure 3.2: Simulation results showing the absorption, reflection and transmission for the metamaterial harvester.

3.3 Mechanism of Operation

To understand the distribution of the dissipated power within the unit cell, the power loss in the ELC resonator, the dielectric substrate and the resistive load were computed, using full-wave simulation over a range of frequencies. Figure 3.3 shows that 97% of the power was dissipated across the load and 3% was dissipated in both the substrate and the copper traces. The power distribution within the unit cell shows a significant difference from previously studied metamaterial absorbers, where most designs relied on the loss

in the dielectric substrates as the main contributor for power dissipation.

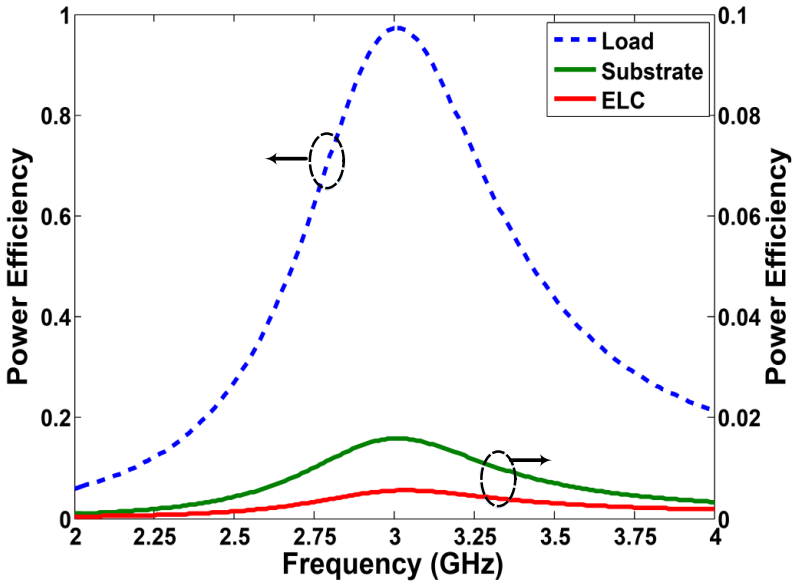

Figure 3.3: Simulation results showing the power distribution within the unit cell after it experiences full absorption.

In the proposed design, a number of factors played a key role in diverting the absorbed power to the resistive load instead of the dielectric substrate. First, a low loss dielectric substrate was used with a loss tangent that is one order of magnitude less than the commonly used FR4 substrate for microwave metamaterial absorber. Additionally, with reference to Fig. 3.4 and by placing the via hole at the optimal location, the surface current along the ELC resonator tends to channel through the via and dissipate across the resistive load. The two face-to-face rings generate anti-circulating

currents that merge at the top of the cell as shown in Fig. 3.4. Hence, by placing the via at the top of the ELC resonator as shown in Fig. 3.4, the via creates a path for the current to flow maximally to the load resistor. This can be clearly seen by the high intensity of the surface current at the via location as indicated by the red color in Fig. 3.4. Most critically, the value of load resistance is selected such that it equals to the impedance of the ELC resonator seen from the load. This allows for maximum power transfer from the ELC top layer to the resistive load. One can modify the dimensions of the ELC resonator, the substrate material and most critically the periodicity

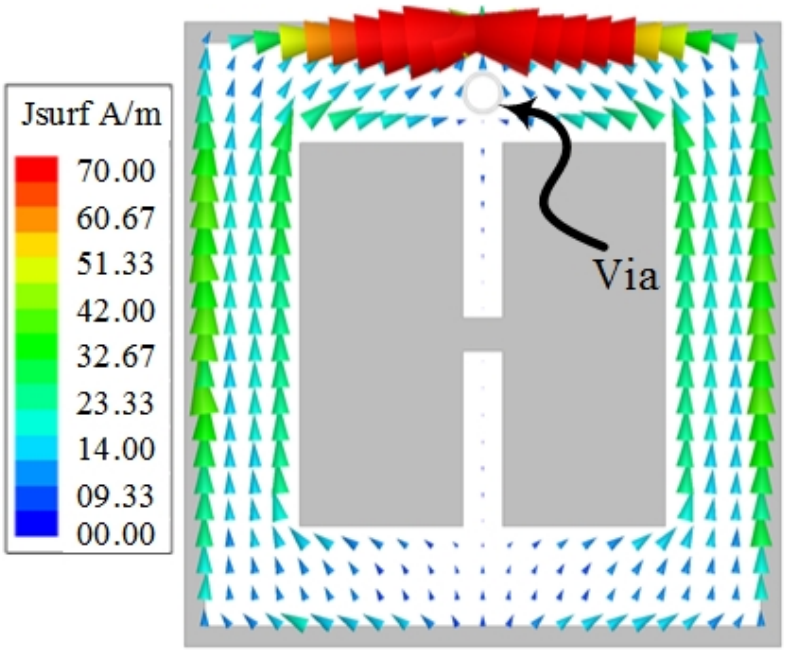

Figure 3.4: Simulated surface current distribution on the ELC cell at the resonance frequency.

of the cell to tune the optimal resistance of the load. Such tuning capability provides flexibility to the design, especially when a diode or rectification circuitry is attached to each unit cell. In fact, the ELC resonator can be designed to have an input impedance equals to the complex conjugate of the diode impedance, thereby avoiding altogether the need for a matching circuit between the absorber and the diode. This would reduce the total size of the energy harvesting system. It is important to emphasise here that the impedance seen from the load is different from the free-space impedance. When the unit cell was designed, the impedance of the metamaterial media was optimized to have an impedance equivalent to the free space impedance at the metamaterial interface to minimize any reflections. This was achieved by tuning ϵ (which is controlled by the ELC top layer dimensions and the periodicity of the cell) and by tuning μ, which is affected mostly by the anti-parallel current of the ground plane and the middle split bar of the top layer, as explained in detail in [114] . Under the assumption that all fields and sources have a time dependence of $e^{j\omega t}$, the extracted parameters at the resonance frequency were $\epsilon_r = 39.73 - j18.74$ and $\mu_r = 40.23 - j19.13$, yielding an impedance of $\eta = \sqrt{\frac{\mu_o}{\epsilon_o}}(1.01 - j0.003)$. It is evident that the medium is well matched to free-space, thus minimizing any reflections at the metamaterial interface [115].

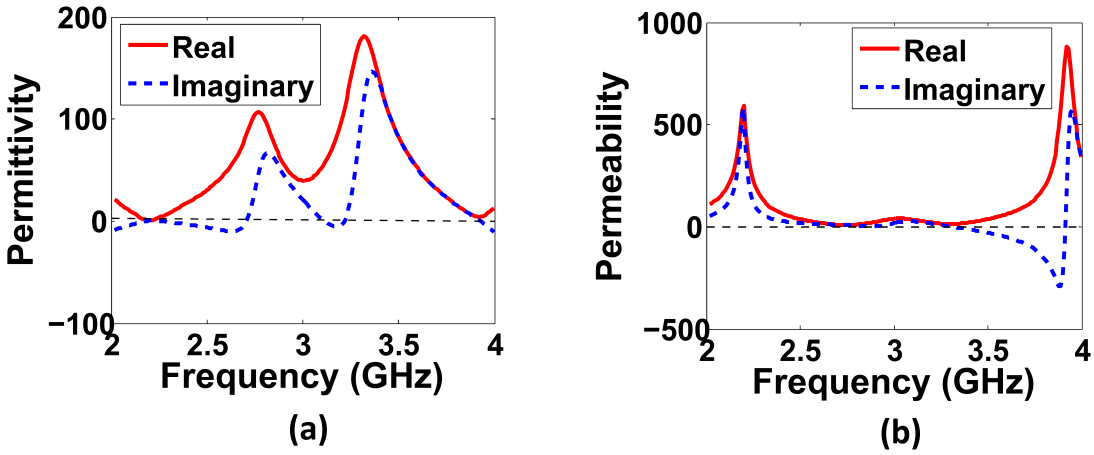

Figure 3.5: The extracted material parameters (a) permittivity and, (b) permeability.

3.4 Experimental Verification

A 13×13 metamaterial harvesting media was fabricated where each cell was loaded with 82 Ω resistor as shown in Fig 3.5. Using a high frequency signal generator, an 11.5 dBi gain commercially available wideband horn antenna was excited with power level of 24 dBm. The array of the energy harvesting media was placed a distance of $R = 3\ m$ from the source antenna to ensure the incident field at the array is a plane wave. The array was positioned such that the incident electric field is parallel to the gap of the ELC resonators as shown in Fig 3.1. The voltage developed across the load of a unit cell was measured using a high frequency probe. It is interesting to note, that high frequency probing requires careful measurement setup

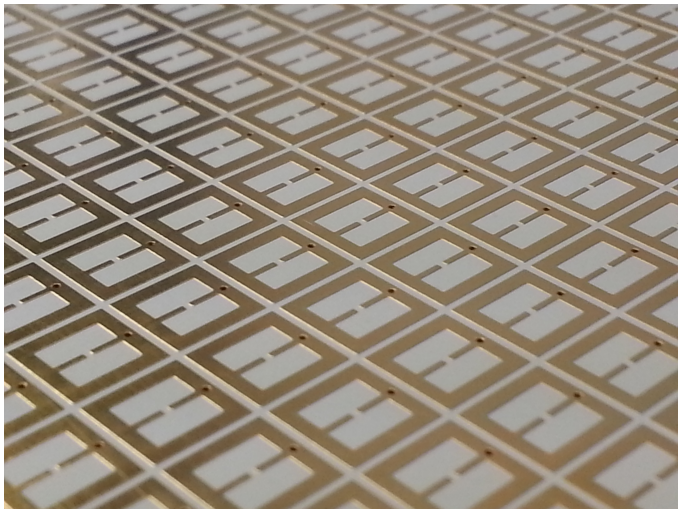

(a)

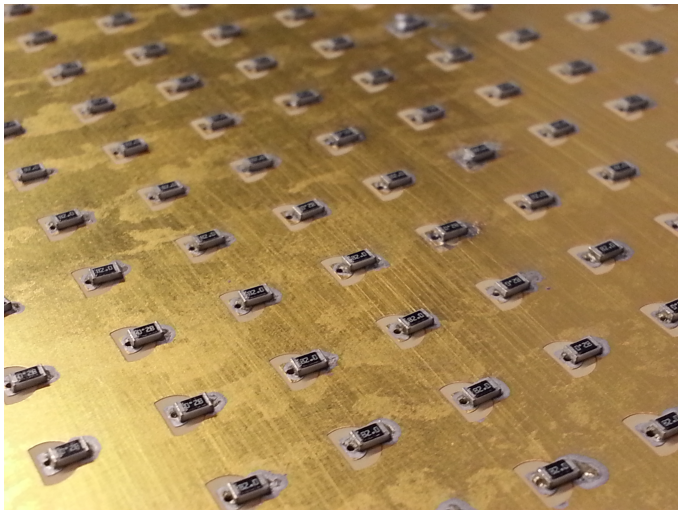

(b)

Figure 3.6: A photograph of the 13×13 array (a) top layer and,(b) bottom layer showing the surface mount resistors placed between the top layer and the ground plane through via holes.

for accurate readings. Unlike communication systems, where electromagnetic structures such as antennas and filters are based on 50 Ω systems, an energy harvesting system does not necessarily need to have a 50 Ω input impedance. In fact, it is desired to operate close to the diode impedance for maximum power efficiency. Therefore, using available 50 Ω measurement devices, such as spectrum analyzers and vector network analyzers, is not well-suited for our purpose due to impedance mismatch between the measuring device and the structure under test. Obviously, one can design a matching network to compensate this mismatch; however, this will add complexity to the measurement fixture, especially when a large array is to be measured. To overcome the issue of impedance mismatch between the measurement tool and the structure under test, a Rohde & Schwarz RT-ZS60 single ended probe was used to measure the voltage across the resistor. The active probe has relatively higher input resistance relative to the load impedance, and when it is connected in parallel across the load, it sees approximately the load impedance. The probe is then connected to a spectrum analyzer through an adaptor to read the voltage picked up by the probe, as shown in Fig 3.7. The function of the adaptor is to match the probe to the spectrum analyzer electrically and mechanically, and also to power the active circuit in the probe.

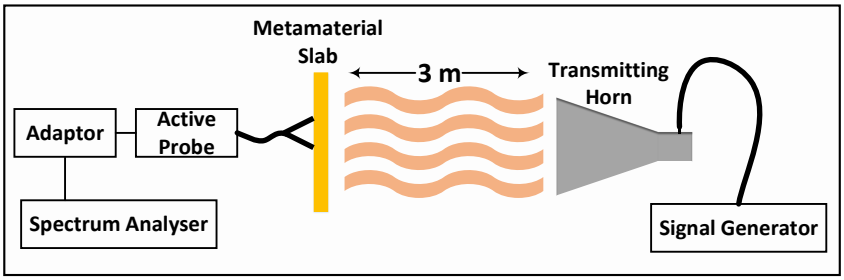

Figure 3.7: A schematic showing the measurement setup used in the experiment.

The efficiency of the unit cell was obtained by [59]:

$$\eta = \frac{P_{out}}{P_{inc}} \tag{3.1}$$

where P_{inc} is the total time-average power incident on the unit cell. Using Friis equation, P_{inc} was calculated as:

$$P_{inc} = P_T G_T \left(\frac{A_e}{4\pi R^2} \right) \tag{3.2}$$

where P_T and G_T are the power and gain of the transmitting antenna, respectively. The effective aperture A_e was approximated to be a short dipole given by [143] $(3\lambda^2/8\pi)$. Such approximation was made due to the type of excitation and the shape of the unit cell, where the largest dimension is $\approx \lambda_o/14$. In addition, P_{out} is the total time-average power developed across the resistive load (measured by the high frequency active probe). Figure 3.8 shows the efficiency of the unit cell obtained from simulation and measurement. The measured peak efficiency was 93% while the simulation

yielded 97%. Also a frequency shift in the center frequency of 6% was observed. Considering practical physical mechanisms of loss that were not accounted for in the simulation, the difference in peak efficiency between measurement and simulation of approximately 4% is satisfactory.

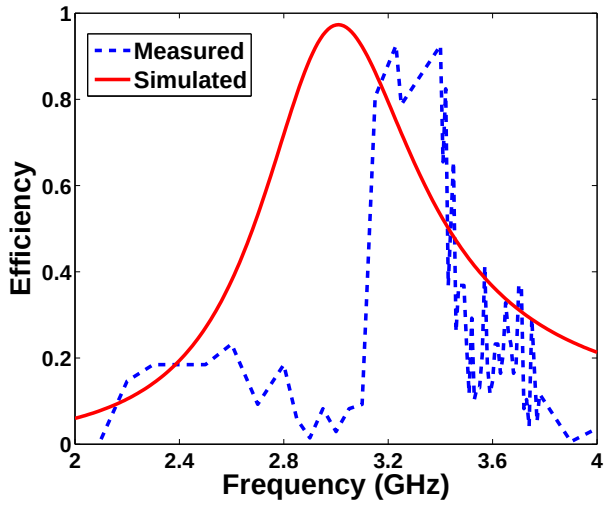

Figure 3.8: The simulated and measured power efficiency of the metamaterial harvester.

3.5 Conclusion

In conclusion, the design of metamaterial harvester inspired by the full absorption concept was presented. The proposed unit cell is capable of absorbing almost all incident power, and most importantly channelling almost all the absorbed power to a resistive load. The power is channelled max-

imally to the load by using a via hole and a resistor that is matched to the ELC resonator. It was found through numerical simulation, that 97% of the power absorbed was delivered to the load. As a proof of concept, a 13×13 ELC resonator array was fabricated and tested. The experimental results show that 93% of the incident power was channeled to the load resistance. Aside from the high power efficiency of the unit cell, The design provides a number of advantages such as the tuning capability of the load input impedance and appreciable size reduction of the unit cell ($\approx \lambda_o/14$) as compared to previous metamaterial absorbers such as the designs presented in [82, 102, 103, 106].

Chapter 4

Electromagnetic Energy Harvesting Using 3-Dimensional Metamaterial Arrays

4.1 Introduction

The design of 3-D metamaterial stacked arrays for efficient conversion of electromagnetic waves energy into AC is presented. The design consists of several vertically stacked arrays where each array is comprised of multiple Split-Ring Resonators. The achieved conversion efficiency is validated by calculating the power dissipated in a resistive load connected across the gap of each resonator. Numerical simulations show that using stacked arrays

can significantly improve the efficiency of the harvesting system, in comparison to a flat 2-D array. In fact, the per-unit-area efficiency of the 3-D design can reach up to 4.8 times the case of the 2-D array. Without loss of generalization, the designs presented in this chapter considered an operating frequency of 5.8 GHz.

4.2 Design Methodology

In this chapter, the design of vertically stacked SRR arrays [16] is presented. Here I show through numerical simulations that when metamaterial arrays are stacked, they significantly improve the total efficiency of the harvesting system. The focus in this chapter is on the radiation to AC conversion efficiency; however, one can extend the design to DC conversion by connecting a rectification circuitry at the feed of the collector without changing the conclusion achieved in this work [38, 116, 117] as will be presented in the next chapter.

Similar to what was presented in chapter 2, a single unit cell of the proposed 3-D metamaterial collector consists of a metallic loop with a gap, as shown in Fig. 4.1(a). The metallic ring is placed on top of an RO4003 substrate, having a thickness of $t = 0.813\ mm$ and a dielectric constant

of $\epsilon_r = 3.55$. The SRR was designed to resonate at around 5.8 GHz with dimensions of $L = 5.3\ mm$, $g = 0.5\ mm$, and $W = 0.5\ mm$ (see Fig. 4.1(a)). Using commercial electromagnetic full-wave simulator ANSYS-HFSS [118], the SRR was excited by a plane wave having different polarizations to test the ability of the resonator to capture the electromagnetic energy from various angles.

A resistive sheet is placed across the gap of the resonator which represents a load, as shown in Fig. 4.1(a). The resistance value is critical and has a great effect on the total efficiency of the resonator. According to the maximum power transfer theorem, maximum power is delivered to the load if the resistance of the load is equal to the Thevenin resistance seen at the gap of the resonator. To find such resistance value, a plot was generated using HFSS where the efficiency of a single resonator is calculated for a range of resistance values. Figure 4.1(b) shows that maximum power transfer to the load occurs when a resistor of $R = 3.5\ k\Omega$ is placed across the gap of the SRR.

A single-array of the 3-D metamaterial harvester is designed using 5 X 5 SRR cells with separation distance between any two adjacent unit cells of $s = 3.5\ mm$, as shown in Fig. 4.2(a). The array occupies a footprint of $a \times a$ where $a = 44\ mm$. An advantage of metamaterial particles over other

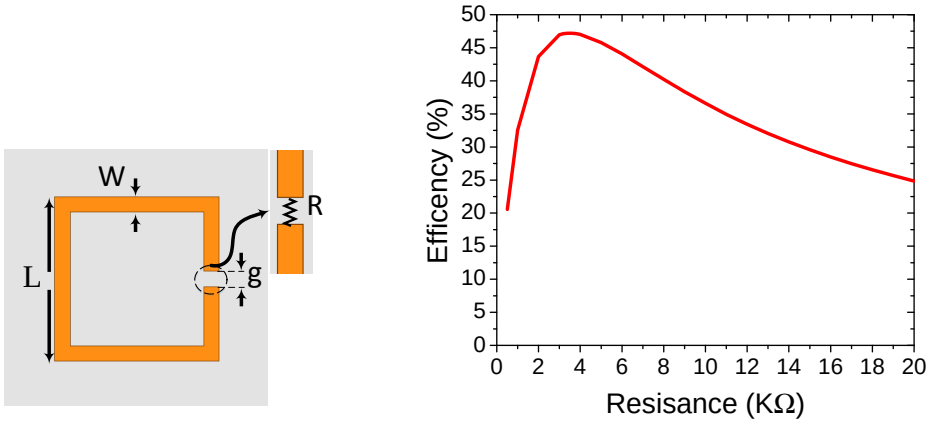

(a) (b)

Figure 4.1: (a) A unit cell of the proposed 3-D metamaterial energy harvesting structure, and (b) the efficiency as a function of the load resistance.

electromagnetic energy harvesters such as classical antennas is that the unit cell can be placed in close proximity to adjacent cells without degrading the total efficiency of the system. In fact, the coupling between SRR cells can indeed lead to improvements in both the efficiency and bandwidth. In the array, each SRR cell is loaded with a resistor of of 3.5 $k\Omega$. The array was illuminated by a plane wave and the efficiency of the array was numerically calculated for three incident angles $\theta = 0°, 30°, and\ 60°$ measured from a line parallel to the H-field vector, as shown in the Fig. 4.2(b). It is evident that the efficiency is higher for larger values of θ. This behaviour is expected as the H-field vector experienced by the resonators is higher for

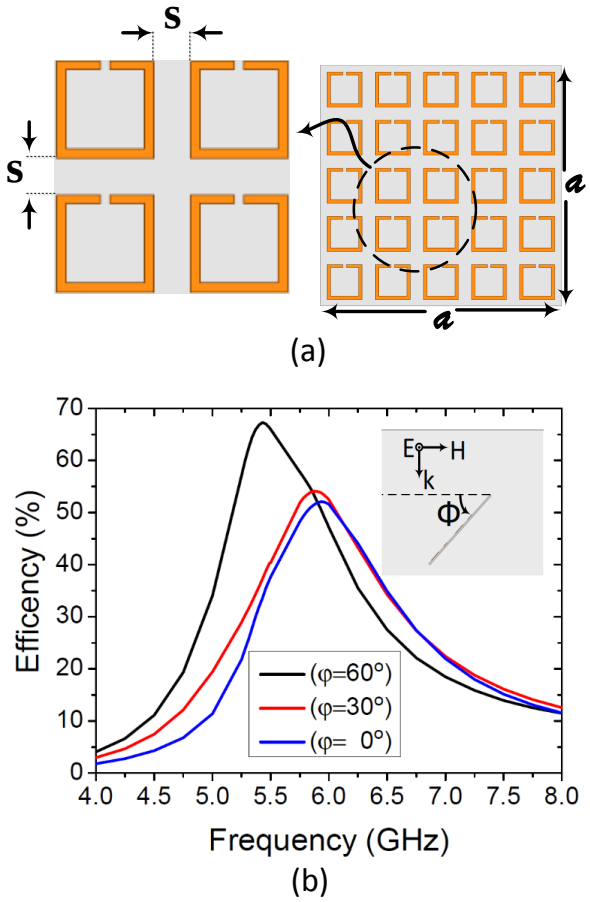

Figure 4.2: (a) A single array of the proposed 3-D metamaterial harvesting system, and (b) the efficiency of a single array with angles of $\theta = 0°, 30° and\ 60°$

larger angles [85].

4.3 The Efficiency of the 3-D Metamaterial Array

The 3-D structure is designed by stacking several 2-D arrays similar to the one discussed above. The key to this design is maintaining a fixed footprint while going vertical. The number of stacked arrays used here is not optimal as the main goal of this work is to present the concept of 3-D electromagnetic energy harvesting using metamaterials. However, one can extend the study to optimize the number of stacked arrays with the goal of maximizing the harvested power, while minimizing the cost of the structure. Four different cases were numerically studied, as shown in Fig. 4.3. Cases *a, b, and c* consist of 4 stacked arrays where each array is tilted with an angle $\theta = 0°, 45° and\ 60°$;respectively, as shown in Fig. 4.2. In case *d*, the arrays are oriented in a zigzag fashion where each two consecutive arrays are tilted with an angle $\theta = 45°\ and\ \theta = -45°$ (see Fig. 4.3). In all cases the cells were loaded with a resistor of 3.5 $k\Omega$ and illuminated by a plane wave with a polarization, as shown in Fig. 4.3.

In Fig. 4.4, a plot of the per-unit-area efficiency of the system for the four cases shows a dramatic enhancement in both the efficiency and the bandwidth. When compared to a single array with 60° illumination, the four cases experience power efficiency of 2.5, 3.47, 4.84, and 2.74 times the single case respectively. In all cases the frequency where the power is max-

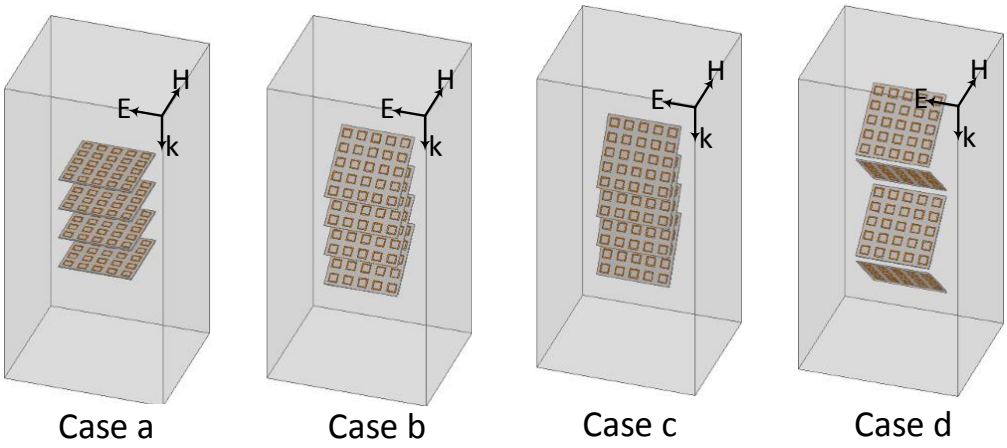

Figure 4.3: Schematic showing the four cases for the 3-D stacked metamaterial arrays.

imum has shifted from the operating frequency of 5.8 GHz for an isolated single cell due to the strong coupling among the cells. However, one can always scale the size of the cells to operate at the desired bandwidth. It is important to note here that the higher than 100% efficiency (see Fig. 4.4) is perfectly physical as per the definition given above. The efficiency here describes the ability of the proposed 3-D metamaterial structure to capture the electromagnetic energy *available* on a 2-D plane. An efficiency of 100% implies the capture of all the power incident on the specified footprint. Therefore, efficiencies higher than 100% indicate that the 3-D structure is capturing more power than the maximum available on a 2-D plane occupying the specified footprint. Please note here that from the discussion on the input impedance provided in section 2.4, the input impedance of the unit

cells will differ for various incident angles of the incoming planewave. Here the resistance was fixed for all cases as in a practical system, the impedance of the load is fixed. This assumption, however, does not change the conclusion achieved as all the cells were compared under the same source of excitation and placed in the same footprint area.

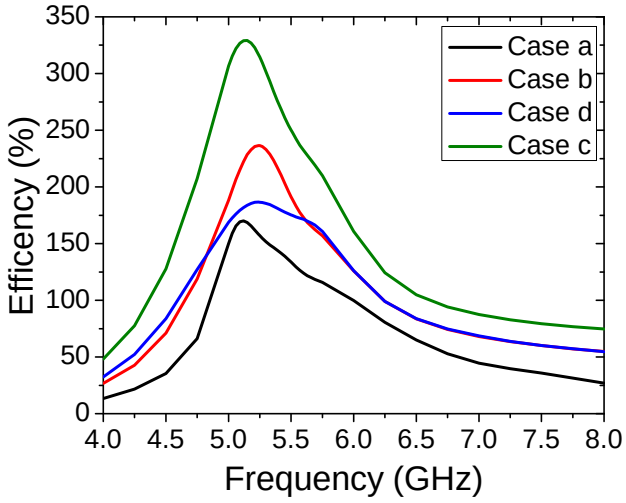

Figure 4.4: The efficiency as a function of frequency for the four cases described in Fig. 4.3.

The electric distribution (projection on the array plane) for case c is shown in Fig. 4.5. It is evident from the field plot that each array has contributed to the total efficiency of the system. In fact, all the cells received certain amount of power even for the cells that are covered by the layers above. This is different from the case when solar cells are used for the 3-D electromagnetic energy harvesting, as the arrays must all be exposed to

sun light as in [119]. The SRR cells on each array were placed periodically and uniformly. It is possible that higher efficiency can be realized if the orientation of the SRR cells is optimized [87].

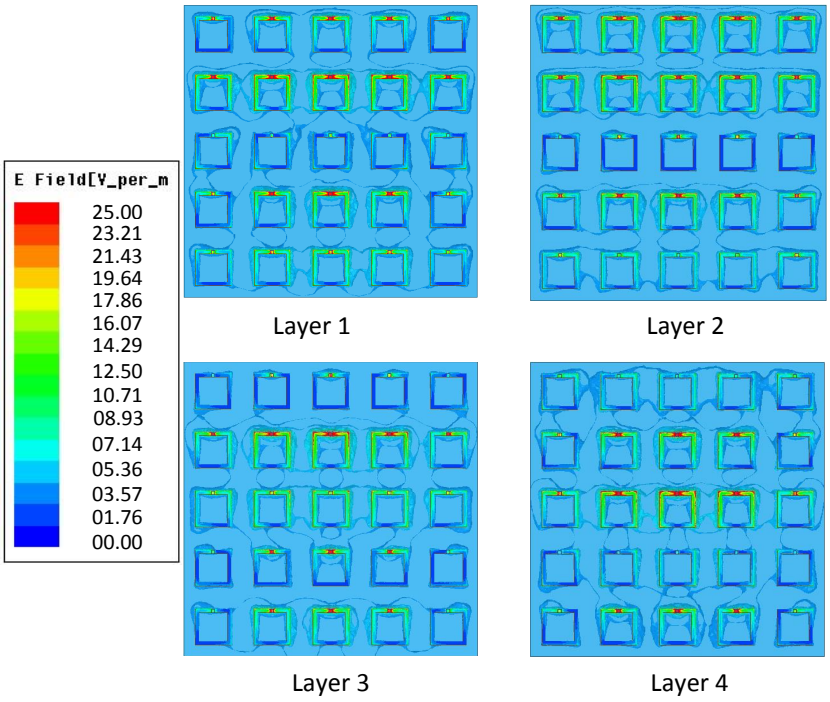

Figure 4.5: Electric field distribution in the plane of the 4 layers of case c.

4.4 Conclusion

In summary, the concept of electromagnetic energy harvesting in 3-D using metamaterial arrays is presented. The model demonstrated here consisted of 4 stacked arrays, each with 5 X 5 SRR cells. The energy was collected

by means of a resistor placed across the gap of the resonator. It was found that using a 3-D stacked array results in per-unit-area efficiency reaching up to 4.8 times that of a 2-D structure. I expect the 3-D array concept to have strong impact not only on energy harvesting systems but also on energy transfer systems such as Wireless Power Transfer (WPT) [116] and Space Solar Power (SSP) systems [65, 120].

Chapter 5

Electromagnetic Energy Harvesting Using 3-Dimensional Antenna Arrays

5.1 Introduction

In electromagnetic energy harvesting, the performance of the rectenna system is measured, most meaningfully, by its power efficiency per footprint which it occupies. A number of articles have studied various ways to improve the total efficiency of the rectenna system such as using more efficient collector, minimizing the total rectenna size, or use of various rectifier types. We have seen in the work presented in Chapter 4 [121] that the total efficiency of an electromagnetic energy harvesting system can be significantly improved by using a stacked Split-Ring Resonator (SRR) arrays. While occupying an

identical footprint, the power collected by 4 vertically stacked SRR arrays was compared to that of a single SRR array [121]. Specifically, the work in Almoneef et al. [121] showed that the stacked configuration achieved 4.8 times the power received by a single array. The vertical stacking concept has been used for antenna applications to improve the bandwidth of the system [122], enhance the total radiation efficiency [123], and reduce the sidelobe levels [124]. In [125], two orthogonal linearly-polarized rectenna arrays backed by a reflecting mirror were used to capture two polarizations. The work in Brown et al. [22] presented two vertically stacked layers where dipole antennas were placed on one layer and the matching networks were placed at a different layer with a spacing distance of $\lambda/2$.

In this chapter, a 3-D stacked folded dipole arrays for electromagnetic energy harvesting is presented. It is shown below that when antenna array panels are vertically stacked and all the panels are connected to a rectification circuitry, the total DC power across the load experience a significant enhancement over a single panel for the same excitation and power levels. In previous work, rectennas were designed in a single or two-dimensional array formations occupying two-dimensional space. In addition, vertically stacked layers were used to capture dual polarizations as in [125]. Here, a 3-D rectenna system that can increase the captured power per footprint is

presented where each array work collectively to leverage the power incident on a 2-D footprint. All rectenna panels are designed to receive maximum energy at the same frequency and polarization.

5.2 Results and Discussion

A single rectenna of the proposed electromagnetic energy harvesting system is shown in Fig. 5.1. It consists of a folded dipole operating at 3 GHz, a pair of DC block capacitors, an HSMS2860 Schottky diode connected in parallel across the antenna feed terminals, and a quarter wavelength coplanar transmission line terminated by a 150 pF capacitor to reduce the ripple level before reaching the load. The input impedance of the Schottky diode was obtained from a diode model [1]. When terminated with a load of 300 Ω, the diode has an input impedance of $Z_d = 187 - j39\ \Omega$ at 3 GHz [1]. To avoid the insertion of a matching network between the antenna and the diode and to minimize the total size of the rectenna, the folded dipole was designed (by careful control of the dipole arms width and length) to have an input impedance equal to the complex conjugate of the diode impedance. The folded dipole was optimized using the electromagnetic full wave simulator ANSYS® HFSS™, having a dipole length $L = 41.8\ mm$ and an arm width $w = 3.6\ mm$, as shown in Fig. 5.1.

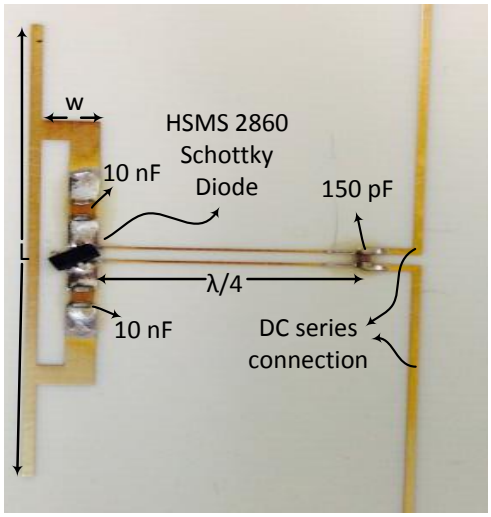

Figure 5.1: Components of a single rectenna unit.

Since its input impedance is matched to that of the antenna, the Schottky diode was integrated right at the feed of the antenna (in parallel). With this design, the two arms of the dipole antenna create a short circuit at DC for the positive and negative leads of the diode, thus, the DC signal will not reach the load but will be trapped in the least resistive path of the loop. Therefore, the two arms of the folded dipole were loaded with two 10 nF chip capacitors to maintain low impedance path for the AC signal at 3 GHz while acting as an open circuit for any DC current generated by the diode. This ensures that the generated DC current does not short the cathode and anode leads of the diode.

To verify its performance, the antenna was fed by a lumped source having

a source impedance equals to the conjugate of the diode impedance Z_d. The simulated return loss and the input impedance of the antenna at the resonance frequency (not shown here for brevity) are -62 dB and $Z_A = 187 + j39\ \Omega$, respectively. In addition, the simulated gain and radiation efficiency of the antenna at the resonance frequency are 1.73 dBi and 0.99, respectively. This shows that the antenna is well matched to the diode. To test the ability of the designed folded dipole to convert radiation to AC power, a 4×4 array was designed where each dipole was separated by a distance of $\lambda/2$ from adjacent elements. The antennas were terminated by a load impedance equals to the diode impedance of Z_d. The antenna array was excited by an incident planewave with three polarizations, as shown in Fig. 5.2b. Then the power dissipated across the load impedance of each folded dipole antenna was computed.

In addition, a 4×4×4 antenna array comprising 4 panels as shown in Fig. 5.2a was excited by a planewave with the same polarizations of the single panel excitation. The power across the loads of the 64 antennas was computed. A figure of merit that reflects the improvement of the power collected by the stacked panels compared to the single panel for the three proposed polarizations is given by the Power Absorption Enhancement (PAE),

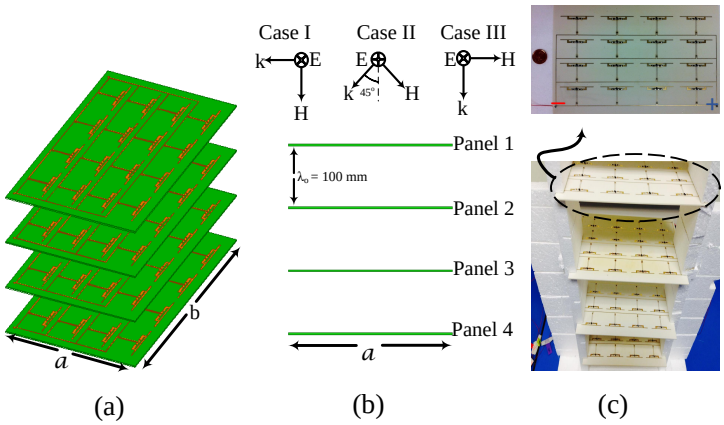

Figure 5.2: Schematic for (a) the 4 vertically stacked panels, (b) the polarization of the incident planewave, and (c) photograph showing the stacked panels held by a styrofoam where a single 4×4 rectenna panel is showing in the inset.

where PAE is obtained by:

$$PAE = \frac{P_{stacked}}{P_{single}} \tag{5.1}$$

where $P_{stacked}$ and P_{single} is the total power delivered to the loads of all collectors (AC or DC power) of the stacked panels and single panel, respectively. We emphasize that our primary goal here is to show the improvement in the power absorption between a single panel and stacked panels both occupying the same footprint.

Figure 5.3a and 5.3b show the simulated $P_{stacked}$ and P_{single} for all three cases, respectively. It is evident form the results that by vertically stacking antenna arrays, the PAE can be higher than 5 around the designed reso-

nance frequency for specific incident wave polarization. It is of interest to note that the maximum power collected for the three cases differ from the power collected at the designed frequency (3 GHz) of a single element (single folded dipole antenna). This is due to mutual coupling between the antennas within a single panel and the coupling due to the close proximity of vertical panels. In addition, we note that the coupling between the antennas in the 4 panels depends greatly on the polarization of the incident angle which affects the total resonance frequency of the system. Therefore, there is a slight deviation of the power collected peaks for all the three proposed polarizations. Since this chapter targets energy transfer applications where the polarization of the energy source is known, we focused our study on the polarization of Case I. However, if the target is energy scavenging where the goal is to maximize energy collection from all polarization angles, one can design a wideband antenna and rectifier to cover a wider frequency bandwidth of power collection.

It is important to note the coupling effect among antennas as it alters the input impedance of each antenna and introduces mismatch loss between the antenna and the diode. A sub array of 4 antennas within the second panel (please see Fig. 5.2b) was numerically studied to minimize the mismatch loss. The 4 antennas shown in the inset of Fig. 5.4b were ex-

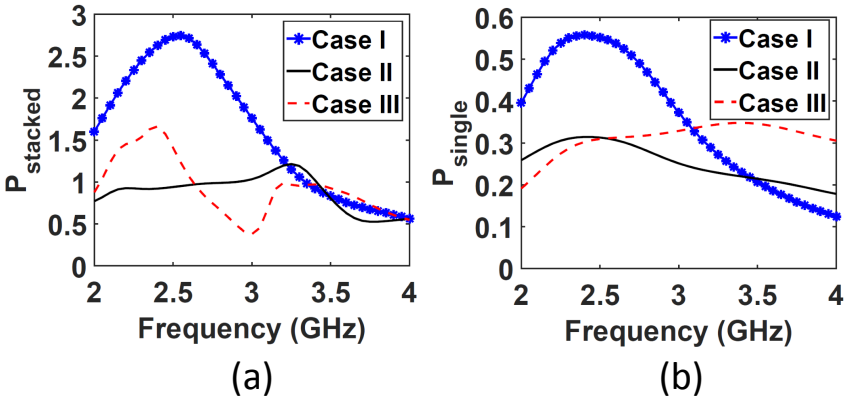

Figure 5.3: Simulation results of the power collected for (a) 4 stacked panels, and (b) a single panel.

cited by a lumped port having an impedance equals to the conjugate of the diode impedance Z_d. In addition, all other 60 antennas within the 4×4×4 system were terminated by the diode impedance. Figure 5.4a shows that antennas 1-4 have a return loss of more than 10 dB between 2.6 GHz and 3.2 GHz. This indicates that the antennas were well matched to the diode impedance. This can be attributed to the $\lambda/2$ spacing among antennas which minimizes the coupling effect among antennas. Please note that the resonance frequency of antenna 1 and 4 (shown in the inset Fig. 5.4b) are slightly shifted from the resonance frequency of antenna 2 and 3 due to their location within the panel being at the edge, resutling in a slight difference in the coupling effect. In addition, Fig. 5.4b shows the strength of the mutual coupling between the 4 antennas along the length of the dipole

L and along the direction of the incident wave of Case I which is perpendicular to the length of the dipole. It is clear from the simulation results that the coupling is more pronounced along the direction of the incident wave denoted by $S14$ and $S23$ due to the nature of the radiation pattern of the dipole antenna. One can lower the coupling effect by increasing the separation distance among the antennas within one panel and the vertical distance separating two panels.

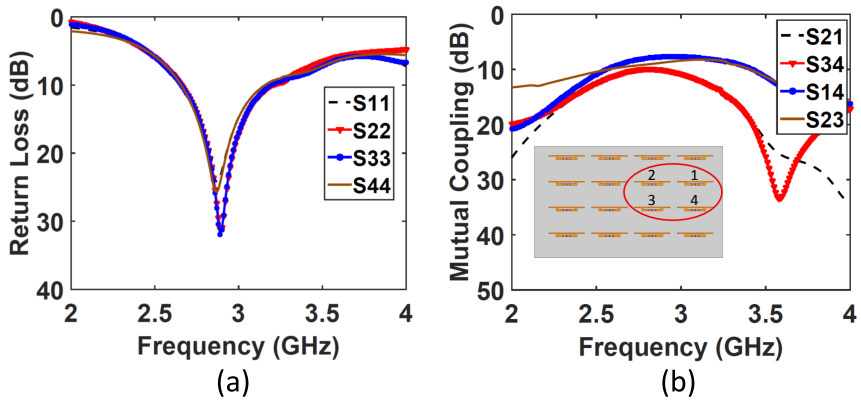

Figure 5.4: A simulation study of the coupling effect within a 4 antenna sub array.

Next, 4 rectenna array panels were fabricated as shown in Fig. 5.2c. The panels were etched on RO4003 Rogers material, having a dielectric constant of $\epsilon = 3.55$, a loss tangent of 0.0027, a substrate thickness of $t = 1.524\ mm$ and a copper thickness of $tc = 17\ \mu m$. A Schottky diode was mounted at the feed of each antenna and connected to a 150 pF through a quarter wavelength two-wire transmission line. The capacitor at the end of the line

acts as a short for the AC signal at the operating frequency which in turn provides an isolation between the AC and DC signal at the feed position. The rectennas were connected through DC lines in a 4 stage series and parallel connection. Then the power is tapped from the two ends of the DC lines indicated by the positive and negative polarities, as shown in the enlarged inset of Fig. 5.2c. With reference to Fig. 5.2a, all the panels are identical having an area of a $\times$ b where the length of a and b are 130 mm and 220 mm, respectively.

An experiment was carried out to test the performance of the 3-D stacked antenna arrays and the results were compared to that of a single panel array, occupying identical footprint. The stacked panels were separated by one free-space wavelength (corresponding to 10 cm at 3 GHz to minimize any coupling effects among the antennas that can create non-uniformity in the input impedance of all antennas). The antennas were excited by a planewave with polarization, as shown in Fig. 5.2b of Case I. The panels of the stacked case were connected using the following three configurations: (a) all panels connected in series, (b) all panels connected in parallel, and (c) a hybrid of series and parallel connections. In the hybrid configuration and with reference to Fig. 5.2b, the outputs of Panel 1 and Panel 2, and the outputs of Panel 3 and Panel 4 were connected in series. Then the outputs

of the 2 groups were connected in parallel.

In the measurement, a 25 dBm signal generator was used to excite an 11 dB gain wide band horn antenna through a 42 dB gain power amplifier. The experiment was carried out in an anechoic chamber where the receiving rectenna 3D array was placed 5.5 m away from the source antenna to ensure planewave illumination, as shown in Fig. 5.5. For each configuration considered, the load impedance was first scanned to find the optimal resistance which delivers maximum power to the load at the resonance frequency. In addition, the power at the receiving end was swept to find the input power that results in maximum power collected across the DC load. Figure 5.6a shows that the rectenna arrays achieve maximum power across the load when illuminated by a power level of around 0 dBm. The output power across the optimal load was then recorded for multiple frequency points around the resonance frequency at the optimal load resistance and power level.

The experimental results for single 2-D panel and the stacking structure with all configurations are shown in Fig. 5.6b and summarized in Table 5.1. The resonance frequency of the receiving system for a single panel has shifted to 2.86 GHz, mainly due to fabrication tolerance and coupling between adjacent antennas within each panel. It is clear that the stacked

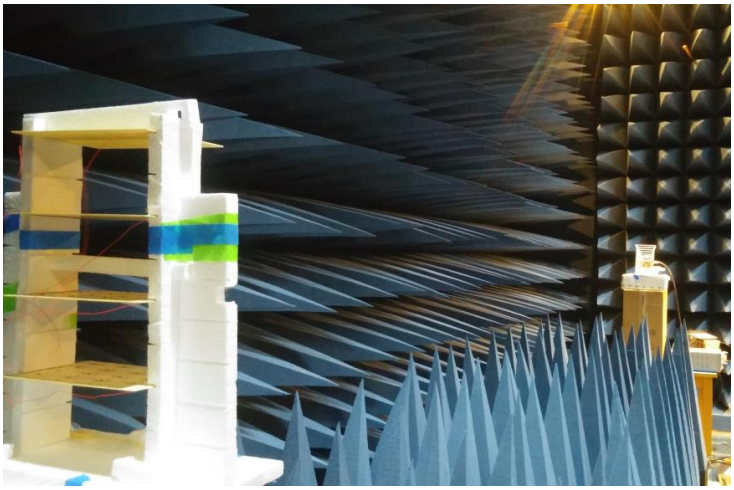

Figure 5.5: Measurement setup at the anechoic chamber, showing the transmitting horn antenna and the stacked 4 panel antenna-array separated by a distance of 5.5 meters.

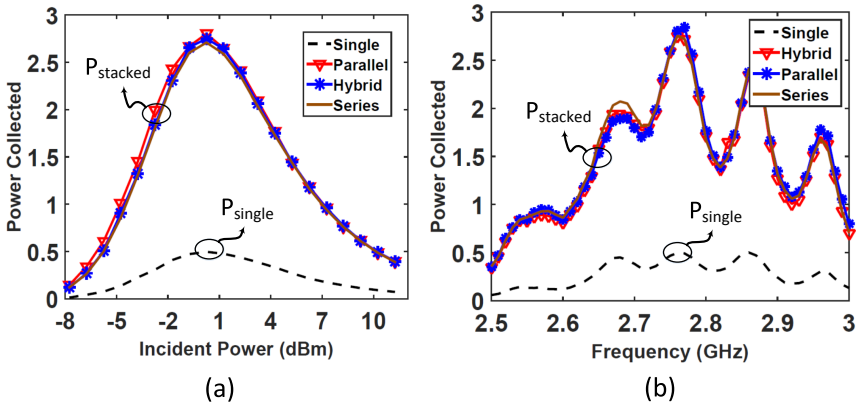

Figure 5.6: Measurement results for the power collected for the single panel and the 4 stacked panels as a function of (a) incident power and (b) frequency.

3-D structure with all various configurations showed a significant enhancement of the received power when compared to a single panel. In fact, a PAE of up to 5 can be obtained over a single 2-D panel which agrees strongly

Table 5.1: Summary of the simulated and measured results

PAE ResultsPAE Results					
SimulationSimulation			MeasurementMeasurement		
Type	Collected Power	PAE	Type	Collected Power	PAE
Single	0.56	–	Single	0.50	–
			Series	2.41	4.82
Stacked	2.74	4.89	Parallel	2.38	4.76
			Hybrid	2.35	4.70

with the PAE obtained from the simulation results. In addition, the measured results for all configurations were very close to the results obtained from the simulations with an error of 2.7% , 3.9% and 1.4% for the parallel, hybrid and the series configurations, respectively. While an improvement of 5 times is achieved when using the stacked panels, this does not set an upper limit to this harvesting methodology as other configurations might lead to even higher power collected. Here, the 3-D vertically stacked structure was studied with only 4 panels as a proof of concept; however, the number of stacked panels can be increased depending on the allowed vertical space available above the footprint under study.

The rectenna arrays presented in the literature commonly use AC chan-

Table 5.2: Optimal load resistance for the configurations under study

Load ResistanceLoad Resistance	
Connection Type	Resistance (Ω)
Single element	300
Single panel	700
Parallel	200
Series	1960
Hybrid	500

neling networks to combine the power output from each antenna element [38, 39, 126, 127]. This can be achieved by utilizing AC combining networks where antennas are connected through cooperative feeds to combine the power and channel it to a single or a number of rectification circuitry. In this method, the input impedance after the power combining circuit is approximately 50 Ω. This will require an AC filter to be inserted between the antenna array and the diode to match the diode with the antenna array which adds loss to the system and increase the total size of the rectenna. In this work, we utilized a DC power combining circuitry [34, 71]. Folded dipoles were used for their high input impedance which allow for impedance tunability so that diodes with matched impedances can be mounted right at the feed of the antennas. This provides ease of power combining as an-

tennas can be easily connected after filtering out any remaining AC power by using shunt capacitors, as shown in Fig. 5.1. In addition, the power output of each antenna can be configured in parallel, series or combination of both to boost the total output current through or voltage across the load resistance.

Although the delivered power levels for the hybrid, parallel and series connections are almost equal, the load resistance vary significantly from one type of connection to the other. The parallel and hybrid connections show much lower resistance values than the series connection, as shown in Table 5.2. Nevertheless, for all connection types, each diode sees identical resistance. The choice of the connection type can play a significant role, depending on the type of load to be connected if it has low, moderate or relatively high resistance.

5.3 Conclusion

The feasibility of a vertically stacked folded dipole antennas for electromagnetic energy harvested was demonstrated. A case study was experimentally studied where 4 stacked folded dipole antenna panels were compared to a single panel both occupying the same flat 2-D footprint in terms of PAE

ratio. The results show that the stacked system can enhance the power absorbed by up to 5 times when compared to a single panel.

Chapter 6

Electromagnetic Energy Harvesting Using Tightly Coupled Antenna Arrays

6.1 Introduction

In chapter 3, a metasurface comprised of 13×13 electrically small resonators was used as an efficient antenna capable of converting 97% of the energy of an incoming plane wave to ac power. However to convert the collected ac energy to dc, a diode has to be connected at the feed of each resonator. In addition, the dc power requires a channeling mechanism where the dc power contribution from all resonators is channeled towards a single load. Also,

a dc filter needs to be inserted between the diode and the load in order to filter out the high frequency components of the waveform to achieve approximately constant dc power across the load. Since the resonators are closely spaced, the placement of the dc power channeling circuitry amongst the resonators remains a challenge and can add additional cost if multiple layers are used. In this chapter, we strive to solve the aforementioned issues by introducing antenna surfaces where the size of each unit cell is comparable to the operating wavelength.

6.2 Tightly Coupled Antennas and their Potential for Energy Harvesting Applications

A new class of antennas referred to as Tightly Coupled Antennas (TCA) was introduced in a number of articles for communication applications [128–130]. In traditional antenna arrays, antennas are separated by a distance of approximately $\lambda/2$ to reduce the undesired mutual coupling between the antennas that affects the input impedance of the antenna. In TCA, however, the antennas are closely spaced over a ground plane thus providing strong coupling. The capacitive coupling is utilized to negate the inductive effect of the ground plane thus widening the bandwidth of the antenna array.

When infinite periodic elements are used, the array effectively mimics a uniform current sheet [128, 131]. The TCA arrays presented in the literature were mainly analysed in the transmitting mode with the goal of designing a frequency wideband 50 Ω system since the arrays were primarily intended for communication applications [132, 133]. The fact that the antennas in a TCA array are tightly spaced adds a very critical design feature where the surface impedance of the array can be modified by varying the separation distance between adjacent antennas to obtain an impedance equal to the wave impedance. This feature can be exploited to fully absorb an incoming wave. It is interesting to note that a wideband frequency response can be also achieved by using electrically-small unit cells such as split-ring resonators [59] and complementary split ring resonators [63].

In this chapter, we present a TCA surface consisting of Vivaldi shape antenna array for electromagnetic energy harvesting and wireless power transfer. The TCA surface is capable of capturing almost all the energy impinging upon it and delivering it maximally to a load. Due to its large electrical length compared to metasurfaces, the proposed design can provide cost effective solutions for large scale energy harvesting applications. In addition, a simplified dc channeling mechanism is presented where the collected dc power is channeled to a single resistive load through the use

of series lumped inductors, avoiding the use of bulky and lossy microstrip based filters.

6.3 The Proposed TCA Unit Cell

A unit cell of the proposed TCA surface is shown in Fig. 6.1. It consists of a Vivaldi shape antenna hosted on top of a 3.175 mm thick RT5880 Rogers substrate backed by a ground plane. The unit cell has a side length of $a = 50$ mm and a separation distance between adjacent cells of $S = 0.3$ mm. Here, S is kept very small ($\approx \lambda_o/300$) to ensure strong capacitive coupling between the unit cells. A Schottky diode was inserted in the gap ($g = 0.5$ mm) between the arms of the Vivaldi antenna where the captured field is highly localized.

The unit cell was simulated using the electromagnetic full-wave simulator ANSYS® HFSS™. In the simulation, the unit cell was placed in a waveguide where the top side of the waveguide was excited by a Floquet port with a power level of 1 W. Periodic boundary condition was applied to the lateral walls of the waveguide to numerically realize an infinite array with a TEM planewave excitation having polarization as shown in Fig. 6.1. The diode was modeled with a resistive sheet in series with a capacitive sheet

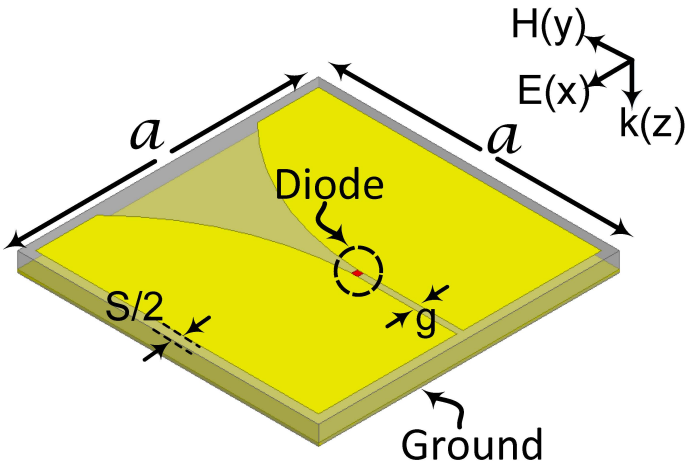

Figure 6.1: A schematic showing the proposed unit cell of a TCA harvester.

to form a series RC load (since the input impedance of the diode is capacitive). The values of the resistance R and the capacitance C of the diode at the operating frequency of 2.84 GHz was obtained from the available diode model [1]. Using the diode model, the efficiency of the diode with a range of load resistances connected across the diode and the corresponding diode resistance are shown in Fig. 6.2. For an HSMS2860 Schottky diode, the input impedance of the diode is $Z_d = 160 - j29\ \Omega$ when operating at a frequency of 2.84 GHz and terminated by a load of $R_L = 250\ \Omega$. At these conditions, the diode gives an ac to dc conversion efficiency of 80%.

The absorption of the unit cell, $A(\omega)$, was computed as $A(\omega) = 1\text{-}|S_{11}|^2$ since the transmission coefficient $T(\omega) = |S_{21}|^2$ is zero due to the presence of

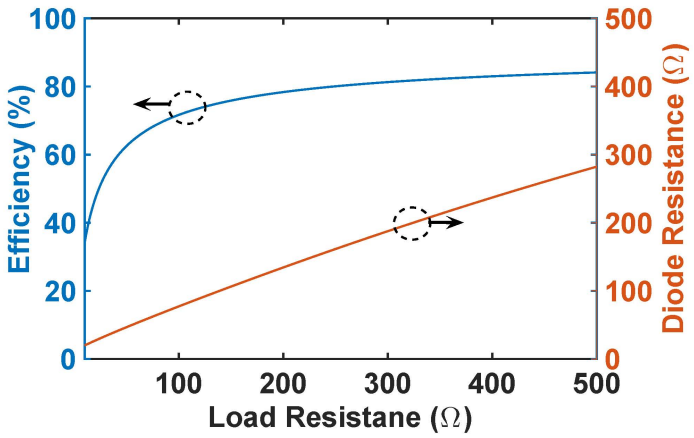

Figure 6.2: Simulation results using the diode model presented in [1]. The load resistance was varied from 0 to 500 Ω at 2.84 GHz.

the ground plane. Figure 6.3(a) shows that the unit cell, when present in an infinitely periodic ensemble, is capable of fully absorbing an incoming plane wave. This is because the effective impedance of the TCA surface is matched to the free-space impedance of 120π Ω at the resonance frequency (see Fig. 6.3(b)). We emphasize, however, that for energy harvesting application, it is critical to ensure that all the absorbed power within the unit cell is mostly channeled to and consumed by the resistive load instead of the dielectric substrate. In fact, this is the main and crucial difference between a surface absorber and a surface harvester. The power consumed across the load resistor in Fig. 6.3(c) shows that 99% of the absorbed energy is channelled across the load instead of the dielectric host material. This is

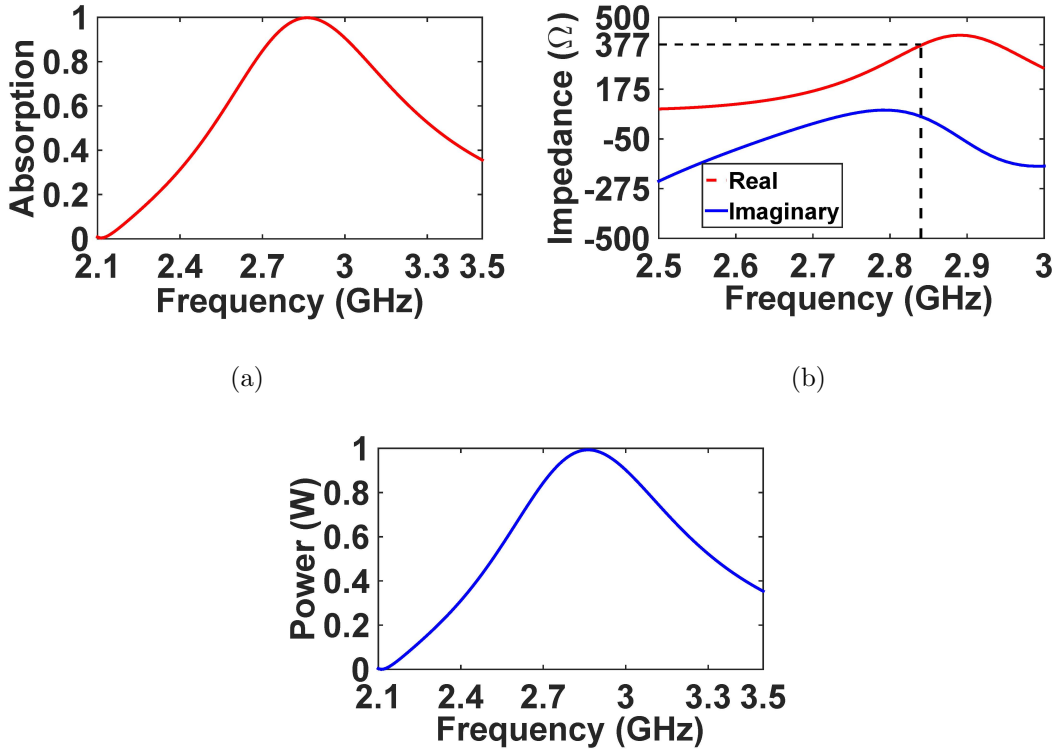

(a) (b)

(c)

Figure 6.3: The simulation results of the TCA unit cell showing (a) the absorption, (b) input impedance, and (c) the power across the load resistance as a function of frequency.

attributed mainly to the low loss dielectric material used ($tan\delta = 0.00019$) and the value and the position of the resistor used across the gap.

Circuit Analog Absorber (CAA) approach has been widely used to explain the absorption mechanisms of periodic absorber surfaces [134–138]. Accordingly, a plane wave interaction with the proposed tightly coupled Vivaldi array can be modeled with a transmission line equivalent circuit as

depicted in Fig. 6.4. In the circuit model, Y_o denotes the free space admittance, Y_A signifies the equivalent circuit model of the Vivaldi antenna along with the diode and Y_1 represents the transmission line equivalent admittance of the RT-5880 substrate. The ground plane backing is modeled as a short circuit termination of the transmission line. The equivalent circuit of the proposed periodic surface is modeled with lumped elements where R and C_1 denote the lumped components representing the diode impedance placed across the feed terminals of the antenna. The capacitors C_2 and C_3 represent the total capacitance between the two arms of the Vivaldi antenna with C_2 accounting for the frequency dependent nature of the gap in between [139]. The total inductance of the Vivaldi arms is represented by L. The substrate material RT5880 with thickness of $d_1 = 3.175$ mm and $\epsilon_r = 2.2$ was modeled as a transmission line with electrical length of 16.1° and characteristic impedance of $377/\sqrt{\epsilon_r} = 254\Omega$.

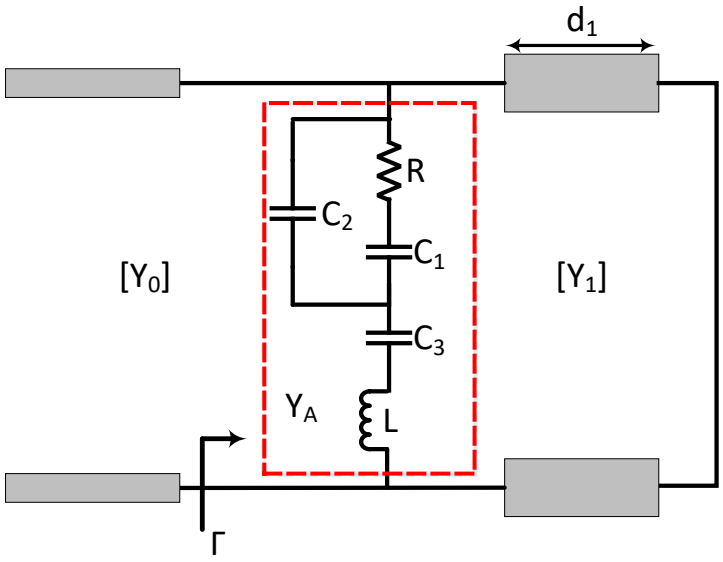

Figure 6.4: A schematic showing an equivalent circuit model of the proposed tightly coupled Vivaldi array. The parameters of the circuit are as follows: C_1 = 1.89 pF, C_2 =1 pF, C_3 =2.2 pF, L =0.2 nH, and R = 160 Ω.

For ideal absorption, the equivalent circuit at resonance must match the free space wave impedance of 377 Ω and the short termination is required to be located at quarter wave length distance, simultaneously. However, in practice both of these criteria can be compromised to obtain a wider bandwidth and lower profile structure. The proposed Vivaldi array achieved near unity absorption with only 3.175mm substrate thickness which is less than 1/33th of the free space wavelength at resonance frequency of 2.84 GHz. The lumped element values in the equivalent circuit were first esti-

mated using a microstrip line model that estimates the total inductance and capacitance of a given strip line [140], and then optimized using ADS. A comparison of the reflection coefficient (Γ) at the surface of the Vivaldi antenna obtained using full-wave simulation (HFSS) and that of the unit cell equivalent circuit is shown in Fig. 6.5. Excellent agreement was obtained between the absorption characteristics of the two models.

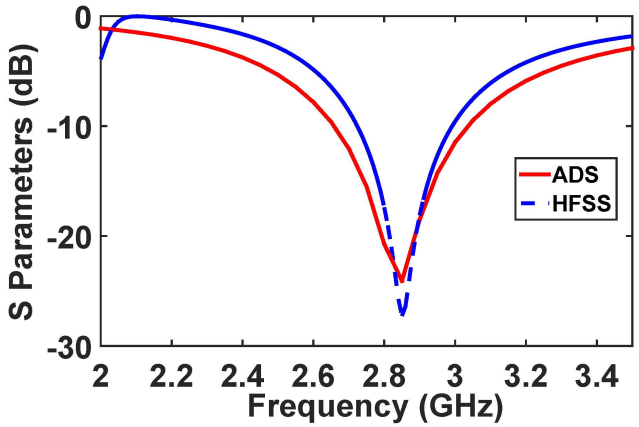

Figure 6.5: The reflection coefficient of the tightly coupled Vivaldi infinite array obtained from full-wave simulation in HFSS compared to the results obtained from the equivalent circuit model.

It is interesting to note here the Electric field (E-field) variation before and after the power absorption occurs. At a distance of $\lambda/2$ above the unit cell, the E-field is constant with magnitude of 500 V/m as illustrated in Fig. 6.6(a). Here, the E-field is referred to as the total field at each point

in the square sheet as depicted in Fig. 6.6. However the E-field close to the TCA surface ($\approx \lambda_o/20$ above the TCA surface), is redistributed depending on the shape of the antenna as depicted in Fig. 6.6(b). The E-field is concentrated along the gap between the two arms of the Vivaldi antenna in addition to the spacing between two adjacent antennas with a maximum magnitude of 2000 V/m. The plot of Fig. 6.6(c) shows the E-field variation right at the surface of the antenna. Interestingly, the E-field is concentrated across the resistive part of the diode with a maximum magnitude of 70000 V/m. This shows the ability of the antenna to capture the energy from an incoming wave and concentrate the energy within the diode with an E-field magnitude that is 140 times larger than the applied E-field. Hence, maximum power delivery to the load can be achieved as almost all the energy is dissipated across the terminals of the Vivaldi antenna (or the diode location).

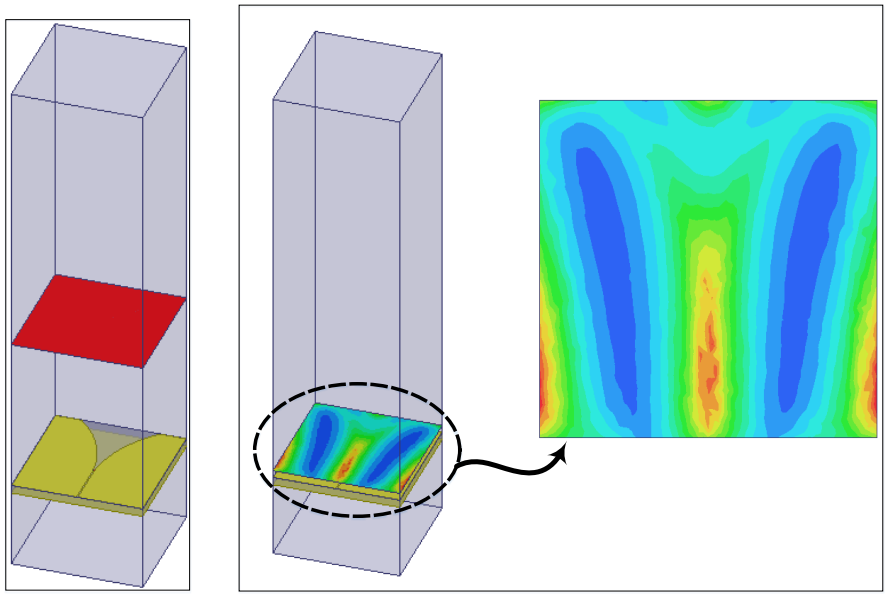

(a) (b)

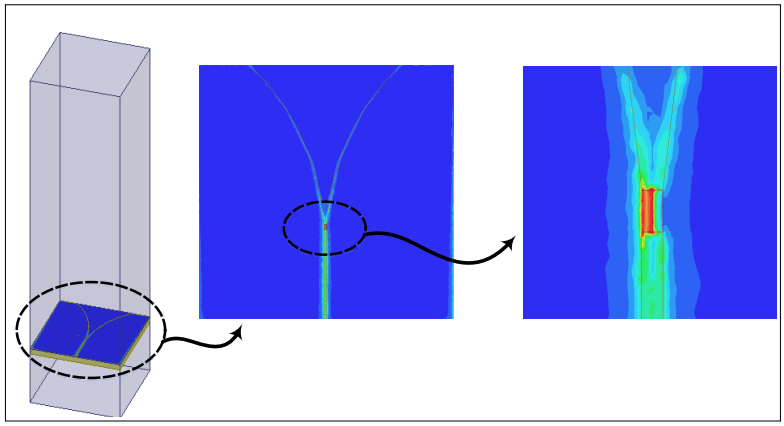

(c)

Figure 6.6: The simulation results of the TCA unit cell showing the field variation at a distance above the cell of (a) $\lambda/2$, (b) $\approx \lambda_o/20$, and (c) right the surface of the unit cell. The maximum magnitudes of the E-field (indicated by the red color) are (a) 500 V/m, (b) 2000 V/m and (c) 70000 V/m

6.4 Numerical Study of a 4×4 TCA Array

To validate the proposed concept, a finite 4×4 Vivaldi antenna array with the same dimensions as the unit cell illustrated in Fig. 6.1 was designed, as shown in Fig. 6.7. The array was simulated with a plane wave excitation having polarization identical to the unit cell excitation discussed above. The array occupies a footprint area of 400 cm^2. The radiation to ac efficiency of the array was computed by [59]

$$\eta_{Rad-ac} = \frac{P_d}{P_{in}}, \tag{6.1}$$

where P_d is the summation of the total real ac power developed across all the 16 resistive loads which also will appear across the diode terminals and P_{in} is the total time-average power incident on the footprint of the array calculated as

$$P_{in} = S \times A, \tag{6.2}$$

where S is the power density on the TCA surface and A is the footprint area of the TCA finite array.

The total radiation to ac efficiency of the array is shown in Fig. 6.8 (red dashed line). From the results, we observe that the total simulated radiation to ac efficiency of the array is 90% with a slight shift of 60 MHz from the resonance frequency of the unit cell. This slight degradation of the

efficiency is due to the non uniform coupling across the elements of the finite array as opposed to the case when the array is infinite. The cells located at the periphery of the array experience less mutual coupling than the cells located in the middle of the array, thus affecting their impedance (referring to Fig. 6.7, cells 6, 7, 10 and 11 experience the highest mutual coupling).

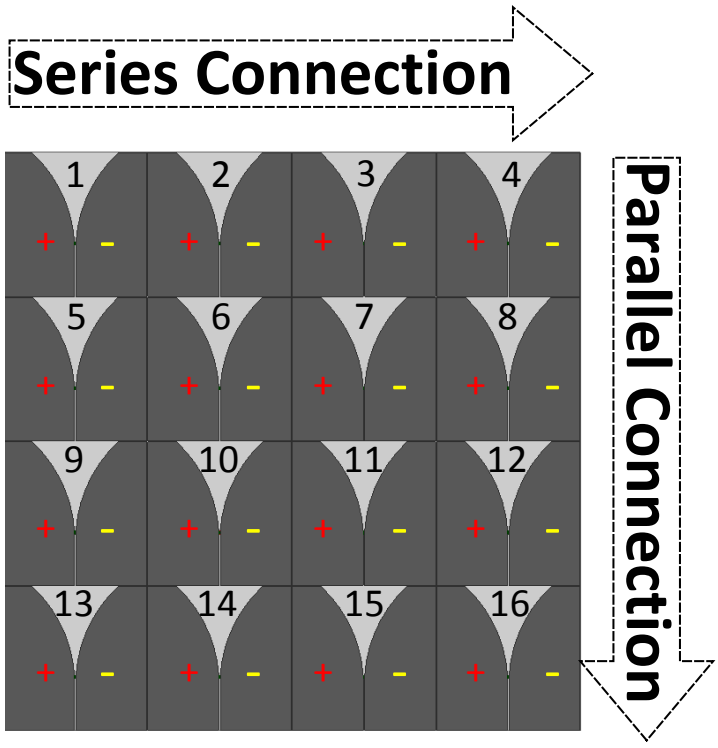

Figure 6.7: A schematic showing the 4×4 TCA array. For the purpose of clarifying the dc channeling, negative and positive polarities are assigned to each cell as shown.

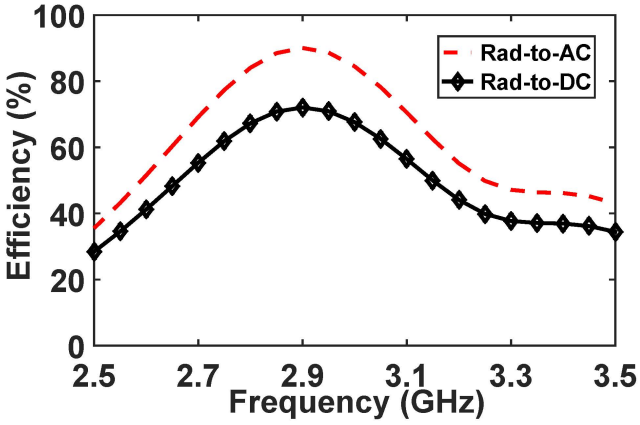

Figure 6.8: The simulated radiation to ac power conversion efficiency (red dashed line) and simulated radiation to dc efficiency (solid black line with diamonds).

The ac to dc efficiency can then be found as:

$$\eta_{Rad-dc} = \frac{P_{dc}}{P_d}, \tag{6.3}$$

where P_{dc} is the total rectified dc power across the resistive load. Here, the resistive load is referred to the load connected after the diode and the dc filter. Hence, the total radiation to dc efficiency can be obtained by taking the product of the η_{Rad-ac} and η_{Rad-dc} as follows:

$$\eta = \eta_{Rad-ac} \times \eta_{Rad-dc} \tag{6.4}$$

The total simulated radiation to dc efficiency is shown in Fig. 6.8 (black

solid line with diamonds). The efficiency peaks at a frequency of 2.9 GHz with a maximum efficiency of 72%.

6.5 Experimental Validation of the 4×4 TCA Array

The fabricated 4×4 TCA surface array is shown in Fig. 6.10. An HSMS2860 diode was mounted across the feed of each unit cell. This type of diode was chosen for its low turn on voltage of $V_{ON} = 0.28$ V, high power handling capability having a breakdown voltage of $V_B = 7$ V, and junction capacitance of $C_j = 0.18$ pF. To channel the collected energy, a dc filter was connected after each diode to filter out the ac components and reduce the ripple of the rectified dc power. However since the antennas are closely spaced, one solution is to place the channeling network on a third layer isolated from the top layer. Using three layered board, however, will increase the cost and weight and add losses to the system. Here we propose a channeling scheme where an inductor is placed between each two unit cells. The value of the inductor (L=68 nH) was chosen carefully such that the inductor acts as an open circuit for high frequencies to maintain an antenna array behavior and a short circuit for dc to provide channeling of the rectified power. The self resonance frequency of the inductor is 10 times the operation frequency to ensure that the inductor behaves as an ac filter at 2.84 GHz. For the dc

component of the rectified waveform, the two arms of each Vivaldi antenna act as a positive and negative leads, as shown in Fig. 6.7. The dc power was channelled in 4 series and 4 parallel stages. With reference to Fig. 6.7, antennas 1-4 , 5-8, 9-12, and 13-16 are connected in series by placing an inductor in between the negative arm of one antenna and the positive arm of the adjacent antenna (see the inset in Fig. 6.10). To merge the series collected power, the negative arms of antennas 4, 8, 12 and 16 were dc shorted by three inductors. Similarly, the positive arms of antennas 1, 5, 9, and 13 were dc connected by three inductors. Hence, the total dc power of the 4×4 panel can be tapped from the positive lead of antenna 13 and the negative lead of antenna 16. The scheme can be generalized to larger arrays.

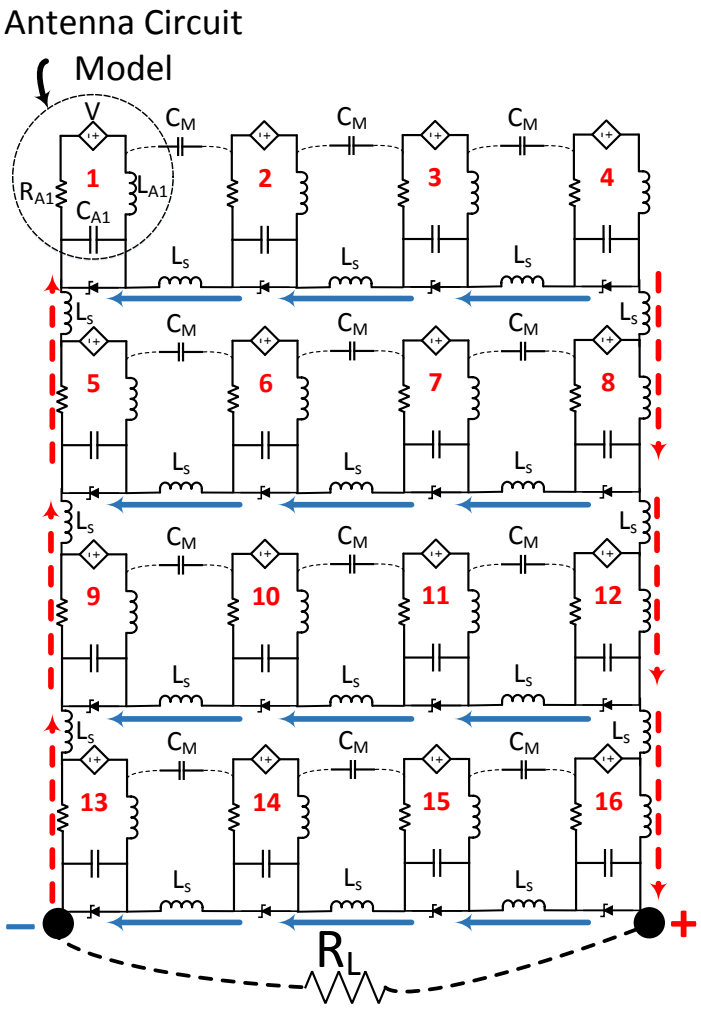

Figure 6.9: The equivalent circuit of the 4×4 TCA array for the purpose of illustrating the series and parallel current path.

A characteristic circuit model for the 16 unit cells is shown in Fig. 6.9. The Vivaldi antenna can be modeled as a dependant voltage controlled voltage source in series with the total resistance R_A, capacitance C_A and

inductance L_A of the antenna. Here the voltage developed across the feed is dependant on the frequency of operation and the angle and the polarization of the incident wave. The mutual coupling is mostly capacitive and is represented by C_M. The rectified power is channeled by using an inductor L_S between the cells. We emphasize that the circuit model is presented here merely for the purpose of illustrating the dc current path rather than for design purposes. In the circuit design, the solid lines (blue in the colored version) running through cells 4-1, 8-5, 12-9 and 16-13 represent the series current where each current sees 4 individual Vivaldi unit cells. The 4 series currents are combined in 4 parallel connections as illustrated by the dashed lines (red in the colored version). The value of the connected resistor R across the 4×4 TCA surface is expected to be the same as the optimal resistance connected across the diode of an individual cell (as obtained in Fig. 6.2). This merely due to the fact that the number of current combining stages being the same for the series connection and the parallel connection.

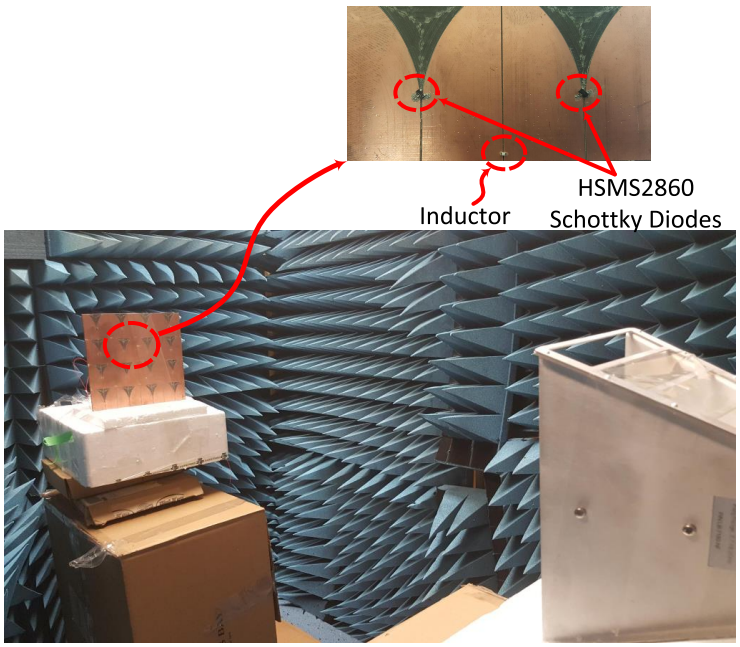

Figure 6.10: The experimental setup showing the transmitting antenna and the TCA surface in an anechoic chamber. The inset shows the position of both the series inductor and the Schottky diode.

The 4×4 TCA surface was tested in an anechoic chamber with the experimental setup shown in Fig 6.10. A horn antenna was excited by a signal generator through a ZHL-16W-43-S Mini-Circuits power amplifier. The TCA surface was placed at a distance of 1 m ($\approx 10\lambda_o$) from the horn antenna to ensure a highly plane wave excitation. Since the diode impedance is a function of the load resistance, the incident power level and the operating frequency, three different tests were conducted to ensure the diode operated at its optimal condition. First, the load resistance across the TCA

surface was varied at the resonance frequency and a fixed input power level, as shown in Fig 6.11 . It was found that the maximum efficiency of the array was achieved when terminated by $R_L = 250\ \Omega$ which agrees well with the load resistance obtained by the diode model. Figure 6.12 shows the radiation to dc efficiency when the power level is swept while keeping the operating frequency and the optimal load resistance fixed. The efficiency of the array peaks when the incident power level at the TCA surface is P_{in}=75 mW. Here, the power level is computed by taking the product of the power density at the surface of the antennas and the surface area of the TCA array.

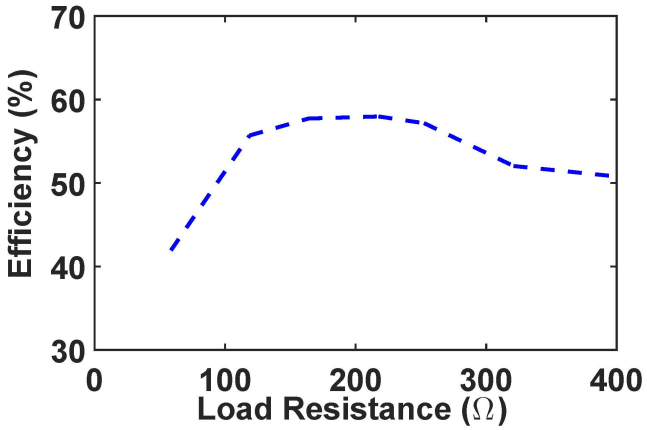

Figure 6.11: The simulated radiation to dc power conversion efficiency with varying load resistances connected across the 4×4 TCA array.

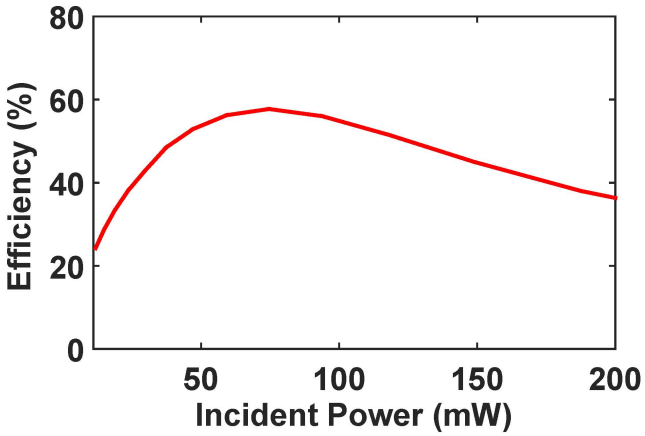

Figure 6.12: Measurement results for the radiation to dc efficiency as a function of incident power.

Finally, the efficiency of the TCA surface as a function of frequency was recorded at the optimal load resistance and incident power level. A maximum radiation to dc efficiency of 60% was recorded at a frequency of 2.75 GHz as shown in Fig. 6.13.

A frequency shift of 90 MHz is observed between the measured and simulated results which we partially attribute to fabrication errors. In addition, it is evident from the results shown in Fig.6.13, 30% of the energy is lost during the rectification process. This can be addressed by studying the efficiency of the rectification circuitry along with selecting the type of diode that will result in low ac to dc energy conversion loss. One possible factor that resulted in this degradation in the measured radiation to dc efficiency

is energy loss of higher order harmonics due to the nonlinearity of the diode. The estimated radiation to dc efficiency obtained from simulation (please see Fig.6.8) did not account for the possible harmonic generation by the diode. One can design a harmonic rejection filter to suppress the harmonics and possibly redirect the energy back to the diode for second rectification process. However, this study is beyond the scope of this chapter since the goal here is to introduce TCA surfaces for electromagnetic energy harvesting.

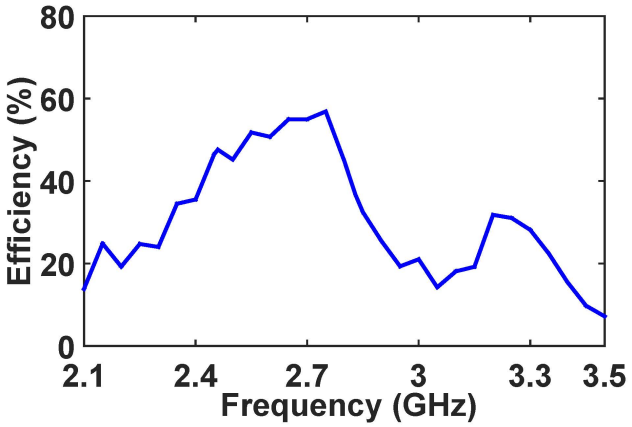

Figure 6.13: The measured radiation to dc power conversion efficiency of the 4×4 TCA array.

6.6 Discussion

Different from a metamaterial surface, a TCA surface is made of electrically *large* unit cells where their size is approximately half of the free-space wavelength at the operating frequency ($\lambda_o/2$). A metamaterial surface, on the other hand, can be made by densely stacking an array of electrically *small* unit cells with a size of ($\approx \lambda_o/10$) [141]. While both surfaces can provide full electromagnetic wave absorption, a TCA surface provides cost effective and simplified ac/dc power channelling solutions when used for electromagnetic energy harvesting applications. As an illustration, if a footprint of an area of (λ_o^2) is used to leverage the electromagnetic energy impinged upon it, one can roughly fit a 2×2 TCA surface or a 10×10 metasurface as shown in Fig. 6.14(a) and Fig. 6.14(b), respectively.

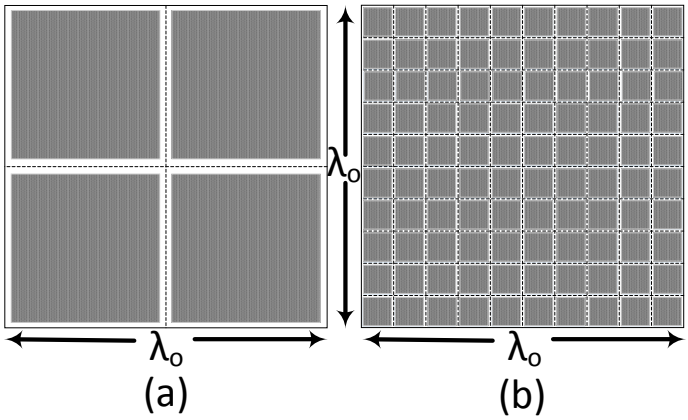

Figure 6.14: An illustration showing a footprint of area λ_o^2 filled by (a) 2×2 TCA unit cells and (b) 10×10 Metamaterial unit cells. The details of the unit cell topology are not shown.

Since the collected energy is tapped from each unit cell, the TCA surface requires a channelling network that can guide the ac energy from the cells to multiple or a single rectifier. In the metasurface however, the channeling network required is more intricate since the energy is tapped from, as in the case of the example illustrated in Fig. 6.14(b), 100 unit cells [61]. This adds losses and complexity to the design as impedance matching has to be maintained throughout the traces leading to the rectifier. In another channeling method, the diodes can be placed right at the feed of each resonator where the channeling network guides all the dc power contribution directly to a load. Here, the TCA surface can provide cost effective design since the

TCA surface in the 4×4 array example discussed in this chapter requires 4 diodes only while the metasurface requires 100 diodes for the same footprint. Therefore, a TCA surface can be an excellent candidate for energy harvesting applications.

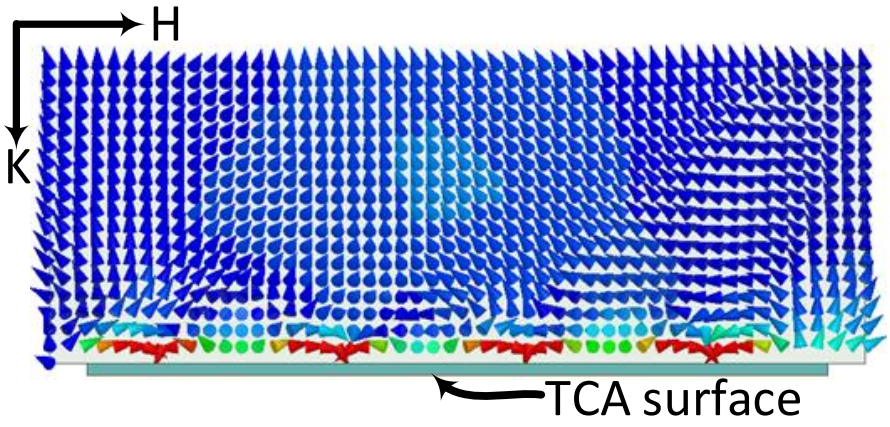

(a)

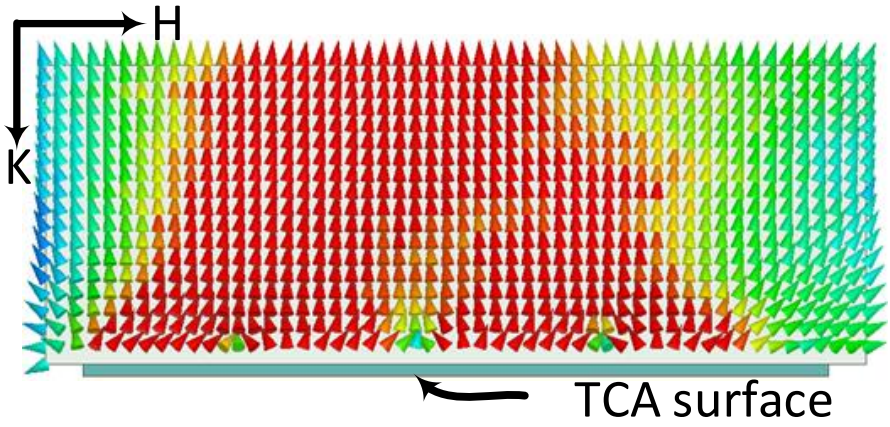

(b)

Figure 6.15: The simulation results of the 4×4 TCA array showing the Poynting vector distribution over a rectangular cross section perpendicular to the plane of the array (a) at the resonance frequency of 2.84 GHz, and (b) at the frequency of 3.5 GHz (away from resonance).

It is well known in antenna theory that the absorption of an antenna(s) from an incident plane wave is related to the scattering from that particular antenna(s). In fact, scattering from antennas is the fundamental reason that allow antennas to absorb energy from an incident planewave [142,143]. It is shown in a number of articles that to absorb half of the energy from an incoming wave, an antenna must scatter at least half of the energy. This sets an upper limit to the maximum amount of energy that antennas can absorb [144]. Interestingly, in the proposed antenna surface, however, the antennas are tightly coupled providing a surface that is impedance matched to the incoming planewave, allowing for almost all the incident energy to be absorbed within the TCA surface. We emphasise here that this condition is true for a single incident polarization at the resonance frequency of the antenna surface. As an illustration, a rectangular cross section of the Poynting vector over the 4×4 Vivaldi array is shown in Fig. 6.15. In the Figure, the magnitude of the energy flux ranges from 0 $\mathrm{mW/m^2}$ (blue) to 1 $\mathrm{mW/m^2}$ (red). At the resonance frequency of 2.84 GHz (Fig. 6.15(a)), the surface scatters very minimal energy as illustrated by the blue arrows with a direction pointing away from the surface. In addition, close to the periphery of the 4 Vivaldi antennas, the magnitude peaks out as the energy is absorbed within each Vivaldi unit cell. When the same is plotted for a

frequency outside resonance such as 3.5 GHz, almost all the energy incident on the TCA surface is scattered away from the surface with minimal energy being absorbed within the Vivaldi unit cells, as shown in Fig. 6.15(b). This is due to the fact that the TCA surface is mismatched to the free-space impedance when operating away from the resonance frequency.

6.7 Conclusions

A demonstration of the potential to use a TCA surface for electromagnetic energy harvesting was presented. It was shown that by using a TCA surface, it is possible to reduce the cost of the total energy harvesting system and simplify the channeling network as compared to a metamaterial surface. It is important to note, however, that a TCA surface is a better choice for energy harvesting applications where the available antenna array footprint is not constrained. In applications with severely constrained areas such as in implantable devices for biomedical applications or remote sensing, metamaterial cells are more suitable because of their sub-wavelength dimensions. Furthermore, while certain metasurface energy harvesters provide similar radiation to ac conversion efficiency to the TCA surface presented in this work, a critical advantage provided by the TCA topology is maximizing the power density per diode which is a critical consideration considering that

sufficient power is needed to turn on the diode.

Chapter 7

Energy Harvesting of Multi-polarized Electromagnetic Waves

7.1 Introduction

In chapter 3 , a metamaterial surface inspired by the perfect absorption concept was introduced for electromagnetic energy harvesting [64]. The metasurface, consisting of an array of 13 $\times$ 13 electrically-small Electric Inductive-Capacitive (ELC) [113] unit cells, was used to fully absorb an incoming plane wave at 3 GHz. Unlike metamaterial absorbers, here the absorbed energy is mainly dissipated across resistive loads placed at the feed of each resonator. However, the work was focused on maximizing the radiation to AC conversation efficiency. The array was also sensitive to

the polarization of the incoming wave, maximizing the efficiency for only one single polarization. What is important for electromagnetic microwave energy harvesting/scavenging is to maximize the captured ambient energy from all polarizations. Moreover, instead of resistive loads, a rectification circuit has to be implemented to maximize the radiation to DC efficiency, forming a full rectenna (rectifying antenna) system [1, 34, 38, 47, 116].

In this chapter, we propose a dual polarized electromagnetic energy harvester, using an array of ELC resonators to form a metamaterial medium. The radiation to AC and the AC to DC conversion efficiencies of the array are studied numerically and experimentally.

7.2 Design Methodology

A unit cell of the proposed dual polarized harvester is shown in Fig. 7.1. The unit cell consists of 4×4 cells forming a super cell. The super cell is hosted on top of a 3.175 mm thick RT/duroid 5880 Rogers dielectric substrate, having a loss tangent of $tan\delta$=0.0009 and a dielectric constant of ϵ_r=2.2. The super cell is backed by a ground plane to block the incident wave from transmitting through the cell. Each cell contains a load resistance placed between the ground plane and the top layer through a via. The

position of the via is alternated for each adjacent cell to allow for capturing the incoming wave from various incident angles, as shown in the inset of Fig. 7.1. Each cell has dimensions of d = 17 mm, w_1=0.6 mm, w_2= 1.85 mm, s=0.5 mm and copper thickness of t = 35 μm. The side length of the super cell is P = 70 mm, having a footprint area of A=49 cm^2.

The choice of the number of cells contained within the super cell is specifically important for the feeding network. One can choose a super cell that contains only two cells as showing in the inset of Fig. 7.1. However, by doing so the channeling circuitry (which will be discussed later in further detail) will be different and more intricate. The main advantage of grouping cells within a super cell is to reduce the feeding ports. By designing a super cell that contains 16 cells where each 8 cells are responsible for capturing one single polarization, the 16 cells can be fed by only 2 feeding networks, simplifying the channeling mechanism of the collected AC power significantly.

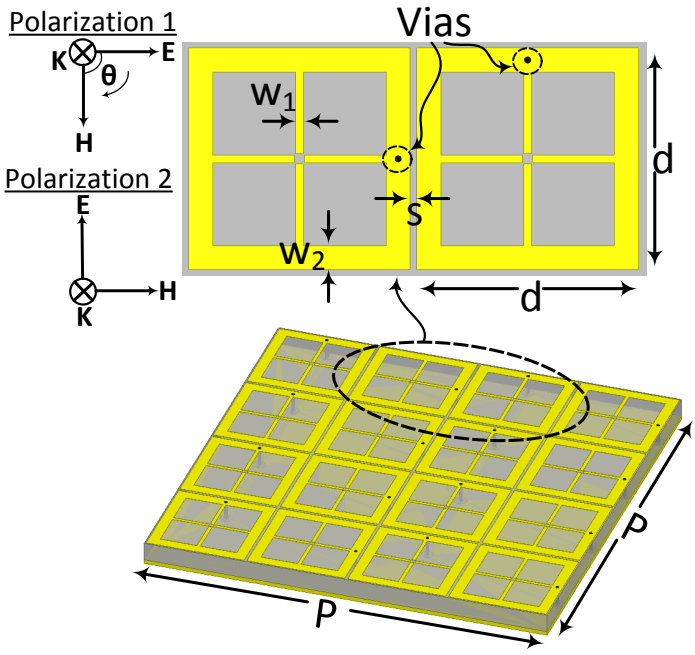

Figure 7.1: A schematic showing the proposed super cell of the metamaterial harvester. The inset shows two cells with different via positioning. The inset also shows the two proposed incident wave polarizations referred to in all sections of the chapter.

7.3 Numerical Analysis of The Radiation to AC Conversion Efficiency

The unit cell was studied using the full wave simulator HFSS [118]. The super cell was placed in a waveguide where the lateral walls were assigned periodic boundary conditions in order to simulate an infinite periodic surface. The waveguide was excited by a Floquet port having a power level of 1

W and two incident wave polarizations, as shown in Fig. 7.1. The scattering parameters for each polarization were extracted to compute the power absorption of the super cell. The absorption of the super cell can be obtained by $A(\omega)$=1-$|S_{11}|^2$-$|S_{21}|^2$ where the transmission coefficient $|S_{21}|^2 = 0$ due to the presence of the ground plane. Figure 7.2(a) shows the absorption of the unit cell as a function of frequency.

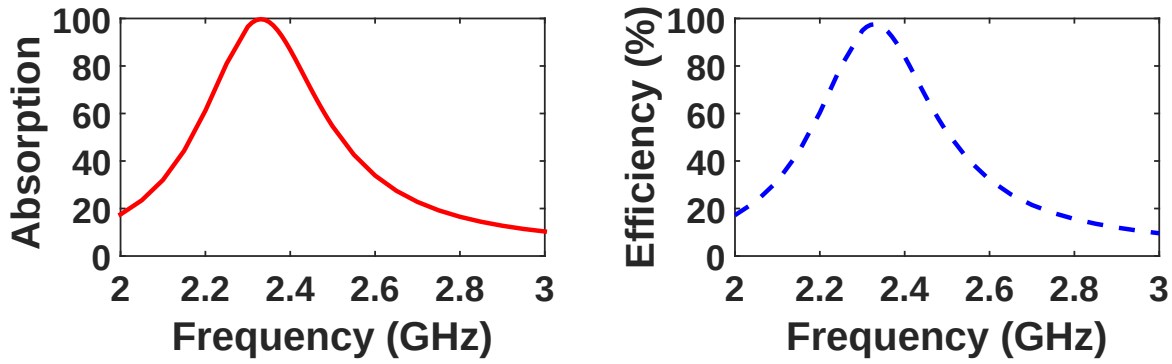

(a) (b)

Figure 7.2: A simulation study of the super cell showing (a) the absorption and (b) the power across the resistive load both as a function of frequency. At the resonance frequency of around 2.4 GHz, 98% of the power is trapped within the resistive load. Both figures represent the results obtained for the two polarizations shown in (fig. 7.1). However, since both curves perfectly overlap due to the high symmetry of the super cell, only one curve is shown in each sub figure.

When each cell is terminated by a load resistance of R = 175 Ω, the super cell experiences full absorption of the incoming wave at the resonance

frequency of around 2.4 GHz. It is also critical to concentrate the loss within the load rather than the substrate material for energy harvesting applications. This trapped energy is later to appear across the leads of a diode or a rectification circuitry for AC to DC power conversion. To achieve such condition, the host material must have a very low loss (i.e. low $tan\delta$) at the operating frequency to minimize the dielectric losses. In addition, a load resistance must be used to mimic a rectification circuit and to allow for a dissipation mechanism for the absorbed energy within the cells. This load resistance is selected carefully such that the input impedance of the cell seen from the feeding port or the load location is matched to the impedance of the cell. This is similar to the input impedance of a probe-fed patch antenna where the input impedance of the antenna depends on the location of the via, except that here the cells are highly coupled where the input impedance can be modified by controlling the coupling effect in addition to the feeding location. The choice of this impedance is also critical for the rectification circuitry as it dictates the impedance of the channeling network and the matching network between the diode and the energy collector.

Figure 7.2(b) shows the efficiency of the super cell as a function of frequency. For both the absorption (Fig. 7.2(a)) and the efficiency (Fig. 7.2(b)) of the super cell, the curves represent both polarizations, as shown in

Fig. 7.1. This efficiency is calculated by taking the ratio of the total energy dissipated across all the 16 resistors of each cell to the incident power. It is interesting to note here that 98% of the incident power is dissipated across the load resistors. However, only 8 resistors are responsible for absorbing the energy for each polarization. This can be understood by the electric field plot across the surface of the super cell, as shown in fig. 7.3(a) for polarization 1 and Fig. 7.3(b) for polarization 2. It is interesting to note here that for each polarization, only 8 cells contain vias at the arms that are parallel to the incident electric field direction. Thus, one expects the cells to absorb half of the total incident energy at each polarization. This is true if the cells were weekly coupled. However, since the cells are strongly coupled, the energy from the cells that contain vias in the arms that are orthogonal to the direction of the incident electric field is coupled to the other 8 cells which contain vias in the arms that are parallel to the electric field direction. This is true for both polarizations, thus the super cell experiences full absorption at each polarization. This is clear from the field plots where the 8 cells that contain vias in the arms that are parallel to the electric field experience high field concentration for both polarizations, as indicated by the red color.

To channel the energy to the desired load, each cell can be terminated

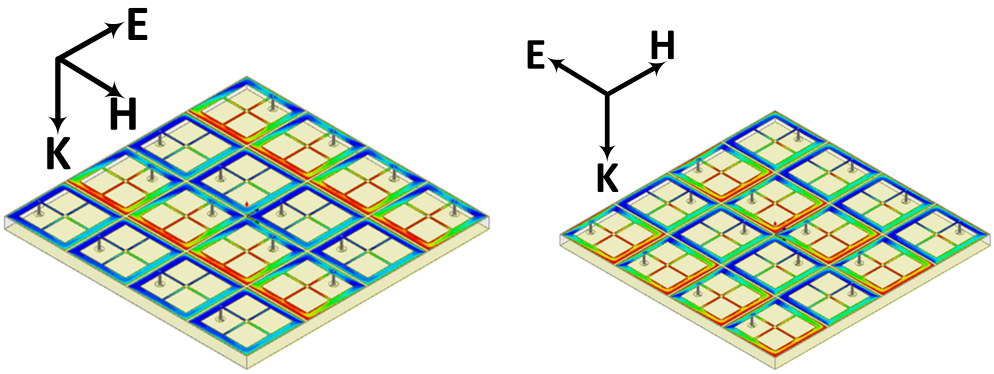

(a) (b)

Figure 7.3: The E-field magnitude plot across the surface of the super cell for (a) polarization 1, and (b) polarization 2.

by a diode instead of the resistor. Thus, each individual cell converts the incident electromagnetic energy directly to DC. Then the DC power contribution from each cell can be combined through DC buses to a single load as was done in a recent work [47]. In this method [47], the number of diodes were equal to the number of cells in the system. This can be in the range of hundreds depending on the size of the harvester, thus the total cost of the system increases. In addition, the AC to DC conversion losses increase linearly with the number of diodes. Other channeling mechanism reported recently use a feeding network to channel all the collected AC power to a single diode or rectification circuitry [61]. In these methods, the AC losses of the feeding network, especially for large footprints, can be significant.

In this chapter, we propose a new channelling mechanism that combines both AC and DC channeling networks, as shown in Fig. 7.4. The AC power collected by the 8 cells for each polarization is combined in three stages to one single feed. The two resulting feeds are to be connected to two separate rectifiers for AC to DC power conversion. The AC power combining circuit for each polarization is not necessarily the same due to the limited space available for each super cell.

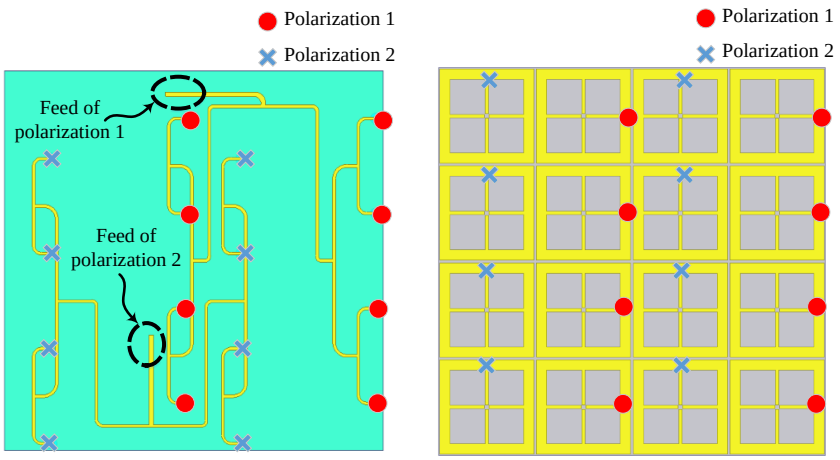

(a) (b)

Figure 7.4: A schematic showing the proposed feeding network for the super cell. The feeding networks for the two orthogonal polarizations, 1 and 2, are not identical to allow for sufficient space for the rectifiers to be integrated on the same layer. (a) Back view. (b) Front view. The o and x marks show the location of the vias used for polarization 1 and 2.

The feeding network is placed on top of an RO4003 Rogers dielectric

substrate having a thickness of 1.524 mm, loss tangent of $tan\delta$=0.0027, and a dielectric constant of ϵ_r=3.55. The feed network was attached at the bottom of the super cell material, forming three separate layers with two different substrate materials. The ground plane is sandwiched between the two materials and the cells are connected to the feed network through via holes. The feed network along with the super cell were simulated as one system. Each feed location (shown in Fig. 7.4) was assigned a lumped source with an impedance of R=175 Ω. The periodic boundary condition was applied to the lateral walls similar to the boundary condition assigned for the super cell except that the top and bottom sides of the waveguide were assigned absorbing boundary conditions instead of excitation ports to analyse the system in the transmitting mode. The transmitting mode analysis is performed to find the directional input impedance of the super cell looking from the feed location, as showing in Fig. 7.4. This impedance is used later to match the rectifier with the super cell for each polarization.

The simulated scattering parameters are shown in Fig. 7.5(a), where S_{11} and S_{22} are the reflection coefficients of polarizations 1 and 2, respectively. Both reflection coefficients show good matching at the resonance frequency with a value of less than -20 dB for each polarization. The transmission coefficient S_{21} between the two feeds is almost negligible, indicating that the

cross talk between the two feeds is minimal. This is critical so that the feeding transmission lines for each polarization does not effect the impedance of each feeding network, thus the rectifier will always experience the same input impedance from the super cell side.

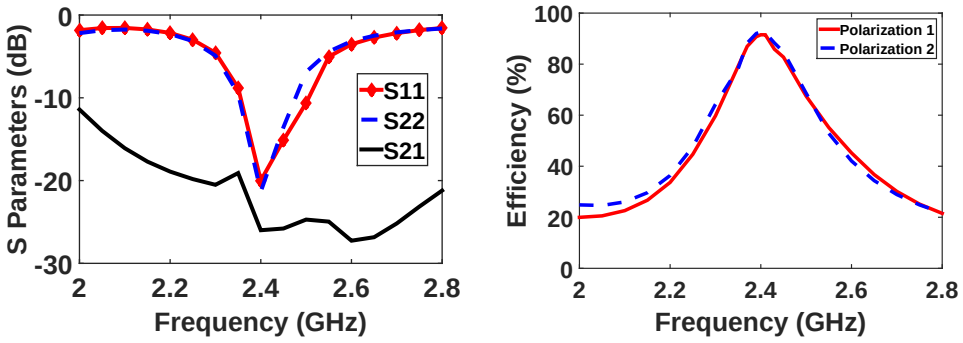

(a) (b)

Figure 7.5: A simulation plot of (a) the scattering parameters showing the reflection coefficient of each polarization (S_{11} and S_{22}) and the transmitting coefficient (S_{21}) between the two feeds(see Fig. 7.4) and (b) the radiation to AC efficiency of the super cell when connected to the feeding network through via holes for both polarizations.

The complete system is then analysed in the receiving mode to test the amount of energy captured from each incident polarization. The two feeds where terminated by R=175 Ω and the super cell was excited by an incident wave having a normalized power of 1 W. The radiation to AC efficiency of both polarizations is shown in Fig. 7.5(b). For both polarizations, the radiation to AC efficiency of the unit cell was 92% at the resonance frequency

of 2.4 GHz. This shows that the loss of the feeding network was 5% since the radiation to AC efficiency of the super cell without feeding is 97% as reported earlier.

7.4 Numerical Analysis of The AC to DC Conversion Efficiency

Taking into consideration the results obtained for the radiation to AC power conversion, a rectification circuitry was designed to build a full rectenna system. A rectifier circuit was simulated in ADS for each polarization. In the simulation, the Z parameters that were obtained from the full-wave numerical simulation for each polarization were extracted and imported into ADS. Then a 1-tone frequency power source was used to mimic the super cell looking from the feeding location (see Fig. 7.4) for each polarization. The Z parameters were inserted into a Data Access Component (DAC) and then it was assigned as the input impedance of the power source. This way the power source will have a different impedance at every frequency to mimic the real impedance of the super cell for each polarization. The rectifier circuit schematic built in ADS is shown in fig. 7.6. The rectifier circuit designed for each polarization has the same circuit layout but with

different transmission lines length and width. The length (L) and width (W) for each transmission line is given in Table 7.1 where the subscript number refers to the transmission line numbering in accordance with Fig. 7.6.

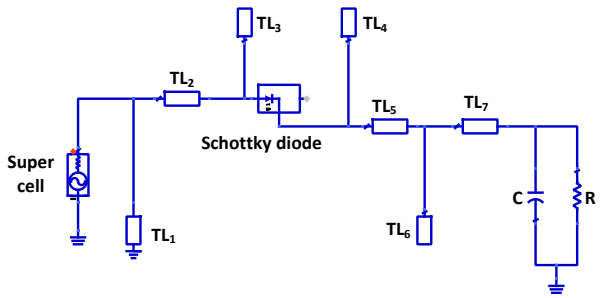

Figure 7.6: A circuit schematic showing the rectifier circuit designed in ADS. The layout is for both polarizations but with different parameters for each polarization as listed in Table 1. There is a total of 7 microstrip transmission line segments where TLn refers to the nth segment.

In the simulation, the Harmonic Balance (HB) simulator was used to analyse the rectifiers due to the presence of the nonlinear diodes. The circuit contains a series transmission line, shorted stub and open circuited stub between the super cell and the diode. A series HSMS 2860 Schottky diode was used for its low turn on voltage of 0.28 V and fast switching speed at the frequency of operation of 2.4 GHz. In addition, two open circuited stubs and two series transmission lines were used between the diode and the RC circuit to ensure a good match between the diode and the load resistance and to filter out all the higher order components of the waveform

Table 7.1: The rectifier parameters of the circuit layout of fig. 7.6 for both polarizations. All the listed parameter are in (mm)

Parameter	**Polarization 1**	**Polarization 2**
L1/W1	3.20/0.50	5.00/0.50
L2/W2	2.01/1.00	1.02/0.97
L3/W3	6.56/4.98	7.28/2.45
L4/W4	1.23/3.00	0.40/4.50
L5/W5	1.34/0.57	8.93/0.40
L6/W6	4.24/1.70	1.98/2.98
L7/W7	3.70/1.94	2.02/3.83

before reaching the load. A shunt capacitor of 120 pF was selected to appear as a short circuit for higher frequencies and an open circuit for the rectified DC power. The rectifier was designed to have an impedance conjugate to that of the super cell for each polarization in order to maximize the power transfer between the energy collector and the rectifier. The Large Signal S-Parameters (LSSP) simulator was used in ADS to analyse the reflection coefficient of the rectifier for each polarization, as shown in Fig. 7.7(a). The diode's input impedance and performance are significantly dependent on the input power level. For low power levels, small signal analysis can be used to obtain accurate results of the diode's response. However, once higher power levels are used to drive the diode, LSSP analysis must be used

for accurate prediction of the diode's behaviour. The reflection coefficients of the rectifier for both polarizations show a well matched condition around the resonance frequency. The obtained profile for both rectifiers shown in Fig. 7.7(a) are similar to the one obtained by the full-wave simulation (see Fig. 7.5(a)) for the super cell. This is due to the fact that the 1-tone frequency power source in ADS was assigned a frequency dependant input impedance that mimics the input impedance of the super cell.

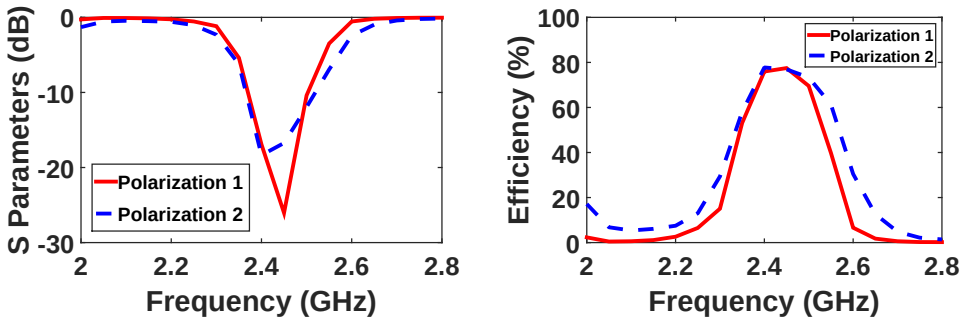

(a) (b)

Figure 7.7: Simulation results showing (a) the reflection coefficient of the rectifier for each polarization (S_{11} and S_{22}) using the LSSP simulator in ADS, and (b) the AC to DC conversion efficiency of the rectifier for each polarization as a function of frequency.

In addition, the AC to DC power conversion of the rectifier was analysed for each polarization as shown in Fig. 7.7(b). The efficiency was calculated by taking the ratio of the power dissipated across the load to the input power assigned at the 1-tone frequency power source. The simulated efficiency

shows that the rectifiers for both polarizations were capable of converting around 80% of the AC power collected by the super cell to DC power across the load resistance of R=1500 Ω. Furthermore, there is at least 10% of an inevitable intrinsic losses attributed to the power conversion process by the diode.

The effect of the input power level for both rectifiers on the AC to DC efficiency was also analysed to ensure that the rectifiers perform at their maximum efficiency. The rectifier was fed by a sweep of input power to analyse the magnitude of the AC to DC power conversion as a function of the input power. The simulated input power sweep as a function of AC to DC efficiency is shown in Fig. 7.8 for both polarizations. From both curves, the rectifiers experience the highest efficiency at around 9 dBm of input power.

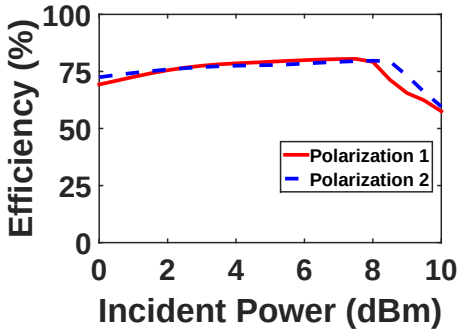

Figure 7.8: Simulation results showing the efficiency of the rectifier for each polarization as a function of input power level.

7.5 Experimental Verification

In light of the results obtained from the full-wave simulation for the radiation to AC analysis and the results obtained from ADS for the AC to DC analysis, a full rectenna system was built as shown in the photos of Fig. 7.9(a) and (b). Nine super cells were built with a total of 144 cells on RT 5880 Rogers duroid substrate material. The feeding networks along with the rectifiers were built on an RO 4003 material. Both materials were stacked together to form a system with three layers and two substrates. The middle super cell was terminated by a Schottky diode, a shunt capacitor and a variable resistor for each polarization. The other 8 super cells were terminated by the matched load resistance of R = 175 Ω. The experiment was performed in an anechoic chamber with a setup as shown in Fig. 7.9(c). A photo of the measurement setup is shown in Fig. 7.9(d).

In the measurement, a 10 dBi gain horn antenna was used as a transmitting antenna. The horn antenna was fed with an E4438C keysight ESG Vector Signal Generator having a maximum power and frequency of 25 dBm and 6 GHz, respectively. To control the amount of power fed to the horn antenna, a Mini Circuits High Power Amplifier ZHL-16W-43-S is connected between the horn antenna and the signal generator. The metasurface was placed 1 m away from the transmitting horn antenna. The voltage across

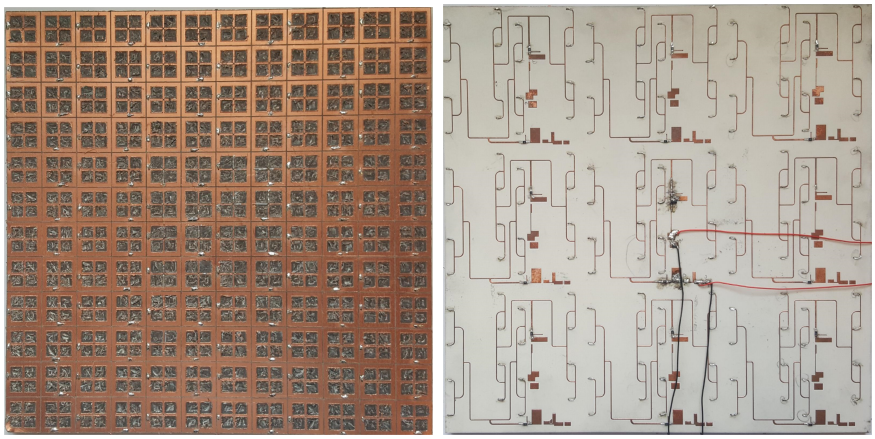

(a) (b)

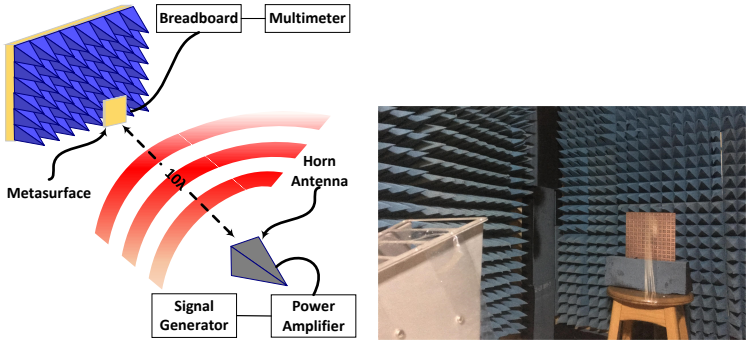

(c) (d)

Figure 7.9: A photograph of the fabricated rectifying metasurface (a) top layer and (b) bottom layer showing the feeding network along with the rectifier for both polarizations. Sub-figure (c) shows a schematic of the experimental setup used in the experiment hosted in side an anechoic chamber. Sub-figure (d) shows the experimental setup inside an anechoic chamber.

each variable resistor for each polarization was measured separately using a multi-meter. The radiation to DC power conversion efficiency of the super

cell was calculated by the following equation [59, 64]:

$$\eta = \frac{P_{out}}{P_{in}} \tag{7.1}$$

where P_{in} is the total time-average power incident on the super cell. P_{in} was calculated as:

$$P_{in} = P_T G_T \left(\frac{A}{4\pi R^2} \right) \tag{7.2}$$

where P_T and G_T are the power and gain of the transmitting antenna, respectively, and A represents the entire footprint or area of the super cell which is A = 49 cm^2. In addition, P_{out} is the total DC power developed across the resistive loads of each rectifier. It is critical to ensure that the rectifier is operating at its optimal incident power level and load resistance for maximum power delivery between the super cell and the rectifier. Therefore, the load resistances across the rectifier of polarization 1 and 2 were swept and the radiation to DC power conversion efficiency was measured at each input power level. Figure 7.10(a) shows that both polarizations experience a peak efficiency at approximately 250 Ω.

The incident power was then swept as a function of efficiency while both rectifiers are terminated by the optimal resistance of 250 Ω. The curves for both polarizations in Fig. 7.10(b) show that the efficiency is maximum

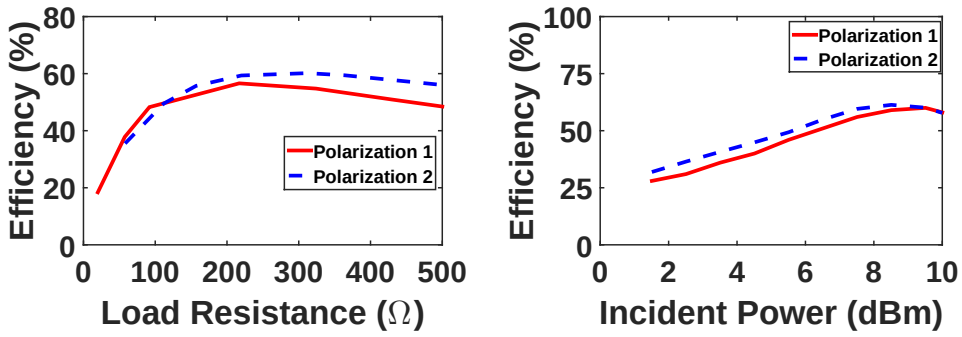

(a) (b)

Figure 7.10: Measurement results showing (a) the efficiency of the rectifier for each polarization as a function of load resistance (b) the efficiency of the rectifier for each polarization as a function of input power level.

when the incident power was around 9 dBm. Here, the incident power is referred to as the real power falling on the surface of the middle super cell which is calculated by the product of the footprint area (A) and the power density at the surface of the harvester.

The efficiency of the rectenna system is then analysed as a function of frequency. In this measurement step, the incident power and the load resistance were fixed at the optimal values obtained above. In addition to the two incident polarizations proposed in Fig. 7.1, four additional incident angles of 15°, 30°, 45° and 60° were also tested. The angle θ is measured with respect to the clockwise rotation of the E field vector of polarization 1 as shown in Fig. 7.1. Figure 7.11 shows the radiation to DC efficiency as

a function of frequency for six incident angles. In the figure, polarization 1 and 2 are referred to as 0° and 90°, respectively. It is evident from the plot that the super cell is capable of capturing the microwave energy and converting around 70% of the collected energy to usable DC power across the load resistance. Moreover, the profile of the efficiency curves for all incident angles overlap having a peak efficiency at a frequency of 2.1 GHz. This is very critical as the main goal of a multi-polarized harvester is to capture the incident energy maximally from different angles at a specific or a range of frequencies. The measured optimal frequency has a slight deviation from the designed one due to fabrication errors. Although the measured optimal power level of 9 dBm was identical to the simulated one, the measured optimal load resistance was different from the one obtained through simulation. This is attributed mainly to the slight frequency shift experienced at the measurement. Due to the nonlinearity of the diode, the efficiency of the rectenna system is a function of the operating frequency, the incident power level and the load resistance. The variation of the optimal resistance when a slight shift of the operation frequency occurs is indicative of the sensitivity of the efficiency of the system due to any change in the resonance frequency. This was not the case for the input power as the input power did not experience significant changes when the operating frequency

was changed. However, since the load resistance and the incident power level were swept for maximum efficiency during the measurement, the diode was ensured to operate at its maximum operation point.

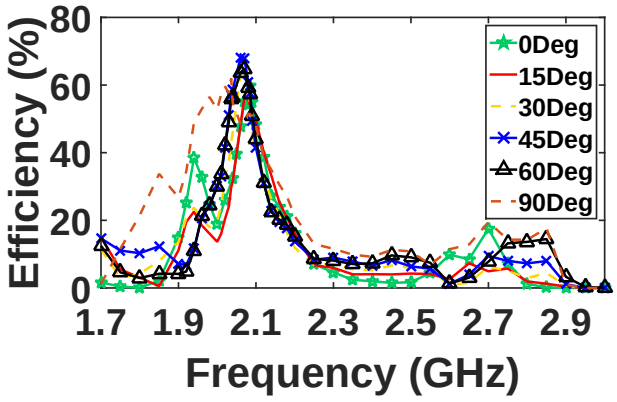

Figure 7.11: Measurement results showing the efficiency of the rectifier as a function of frequency for various incident angles.

7.6 Discussion

When an infinite array of the super cells shown in Fig. 7.1 is arranged in a periodic fashion, a surface is created with an impedance matched to the free-space impedance. Such feature is the key advantage to the current design and the main reason that enable metasurfaces to be an excellent candidate for electromagnetic energy harvesting. When an incident planewave strikes a metasurface that is matched to the free-space impedance, almost

all the energy is absorbed within the metasurface harvester with minimal energy scattered away from the interface of the structure. To illustrate this concept, 12×12 cells with nine super cells were simulated numerically. In the simulation, the metasurface was excited by a planewave with two polarizations as depicted in Fig. 7.1. The metasurface was enclosed by a absorbing boundary condition to ensure no power is reflected back to the metasurface from the boundary walls. Figure 7.12 shows a rectangular cross section of the Poynting vector perpendicular to the metasurface array for both polarizations. The range of colors represents the magnitude of the energy flux ranging between the lowest of 0 $\mathrm{mW/m^2}$ (deep blue) to the largest of 1 $\mathrm{mW/m^2}$ (deep red). When the plane wave hits the metasurface at the resonance frequency of 2.4 GHz (see Fig. 7.12(a) for polarization 1 and Fig. 7.12(c) for polarization 2) , the energy is absorbed by the cells as depicted by the red color close to the metasurface interface. In addition, minimal energy is scattered/reflected away from the surface as illustrated by the blue colored arrows pointing away from the surface. This indicates that the energy is absorbed within the metasurface array at the resonance frequency. Away from the resonance frequency (i.e., 4 GHz), however, the metasurface acts as a reflector as depicted by the red colored arrows pointing away from the metasurface as shown in Fig. 7.12(b) for polarization 1

and Fig. 7.12(d) for polarization 2.

Although the designed metasurface at the resonance frequency experiences full absorption, this does not necessarily qualify it as an energy harvester. This is due to the fact that the absorbed energy can be lost within the dielectric substrate as the case in previous metasurface absorbers presented in the literature [82]. In metamaterial absorbers, the main goal is to absorb the energy regardless of where the absorbed energy is lost. However, in metamaterial harvesters, the metasurface must be able to: (1) absorb all the energy from the incoming wave, (2) deliver all the absorbed energy to the load, and (3) replace the load with a rectification circuitry and convert the collected AC energy to DC. From Fig. 7.2(a) and (b) it is evident that point (1) and (2) are satisfied. Minimizing the rectification losses (point (3)) remains a challenge due to the inevitable losses of the diode during the turn on process. In addition, the generation of harmonics from the nonlinearity of the diode is another source of losses. Although it is beyond the scope of the present study, it is suspected that such losses can be minimized by introducing filters to suppress the energy lost due to higher order harmonics.

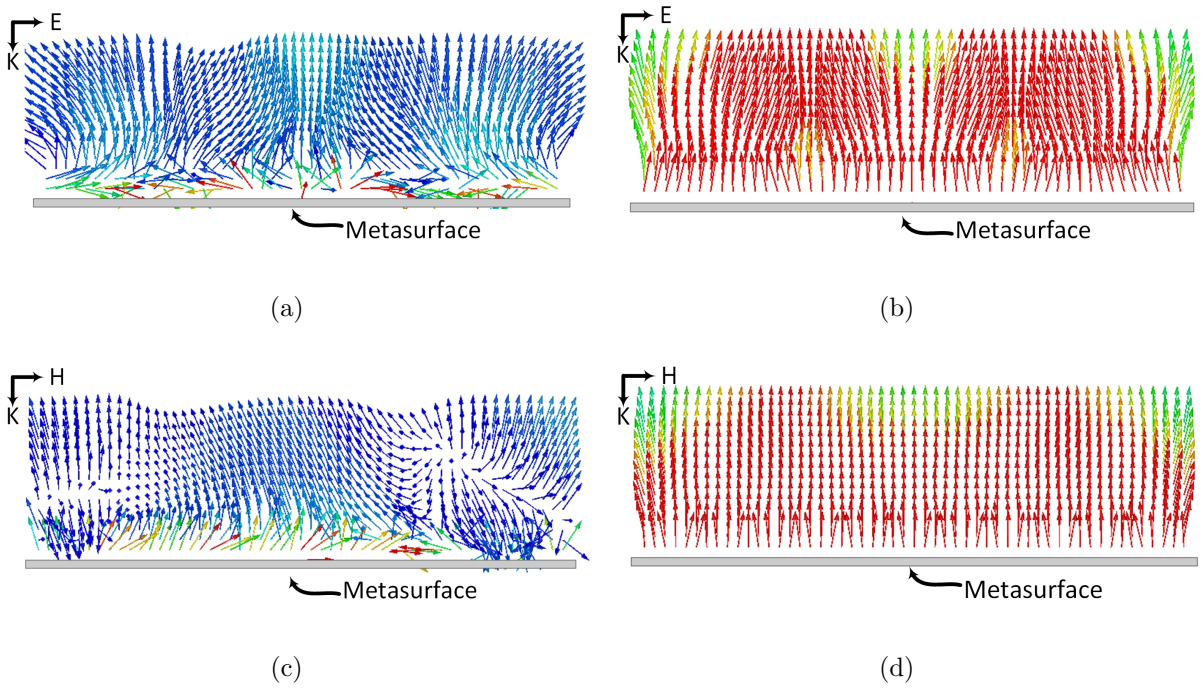

Figure 7.12: The simulation results of the 12×12 cells array showing the Poynting vector distribution over a rectangular cross section perpendicular to the plane of the array for (a) polarization 1 at the resonance frequency of 2.4 GHz (b) polarization 1 at a frequency of 4 GHz (away from resonance).(c) polarization 2 at the resonance frequency of 2.4 GHz, and (d) polarization 2 at a frequency of 4 GHz. Darkest blue corresponds to 0 mW/m^2 and darkest red corresponds to 1 mW/m^2.

7.7 Methods

Simulation: The radiation to ac efficiency simulation of the super cell was performed using the full-wave numerical simulation tool HFSS. In the simulation the super cell was placed inside a waveguide with periodic boundary

condition assignment on the lateral walls. Master and slave periodic boundary condition was used for the four lateral walls to simulate the super cell in the presence of an infinite array as shown in Fig. 7.13. The top and bottom sides of the waveguide were assigned with Floquet excitation ports with modes that support the two proposed polarizations illustrated in Fig. 7.1. The load resistors were modeled as a lossy sheet and the energy dissipated across each resistor was calculated using the surface loss density formula embedded in the simulator's calculator. The simulations were performed in two stages: first, with reference to Fig. 7.1, each cell was terminated by a resistor having a resistance value of 175 Ω. Then, the super cell was studied in terms of power absorption and power dissipation across the total 16 resistors. Then, a feeding network was placed at a different layer and the energy from each cell was channelled to the feeding networks through via holes running through the two substrates and the ground plane. The second stage of the simulation was performed on the super cell including the feeding network. The energy captured by each 8 cells (having the same polarization) was channelled to one feeding network. Hence, each super cell contains two channeling networks, one network for each polarization as depicted in Fig. 7.4. At the end of each feeding network, a resistive sheet is placed between the end of the feeding line and the ground plane. The

super cell along with the feeding network was simulated in the transmitting mode by replacing the Floquet excitation ports in Fig. 7.13 with absorbing boundaries. In addition, the two resistive sheets at the end of each feed line were assigned excitation lumped ports with input impedance of 175 Ω.

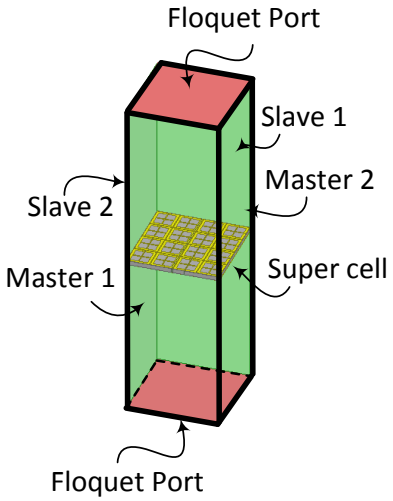

Figure 7.13: An illustration to clarify the periodic boundary condition simulation setup of the super cell in HFSS.

The AC to DC simulation of the rectifier was performed using the circuit simulator ADS. First, the impedance matrix of the super cell obtained for each polarization in the transmitting mode analysis from the full-wave simulation was extracted and saved in a citi file format. Here the Z matrix is refereed to as the directional impedance at the feed location circled in Fig. 7.4 for each polarization. Then the file is imported in ADS and saved

in a DAC component. A single tone frequency power source was used with an internal frequency dependant impedance identical to that of the super cell for each polarization. This will ensure that the rectifier is energized by a source that has the same impedance as the super cell's input impedance and hence impedance matching between the super cell and the rectifier can be performed. The HSMS 2860 Schottky diode chip can be modeled with its series resistance R_S in series with a parallel combination of the diode's junction capacitance C_j and junction resistance R_j as illustrated in Fig. 7.14(a). However, to account for the parasitic capacitances and inductances due to the bondwire, leadframe and the diode packaging, the diode model can be extended to the circuit shown in Fig. 7.14(b). In the circuit model, L_L is the leadframe inductance, C_L is the leadframe capacitance and L_B is the inductance due to the bondwires [2]. The rectifier was analysed using the LSSP and HB simulators to account for the nonlinearity effect of the diode. Then two different rectifiers were designed accordingly and the traces for the rectifier were added after the feed location for each polarization (see Fig. 7.4) before the fabrication stage.

Fabrication: In the fabrication stage, a 3×3 super cell array was fabrication which contains 12×12 cells. The full system consists of 3 different layers and two substrates, as shown in Fig. 7.15 for an exploded view of a

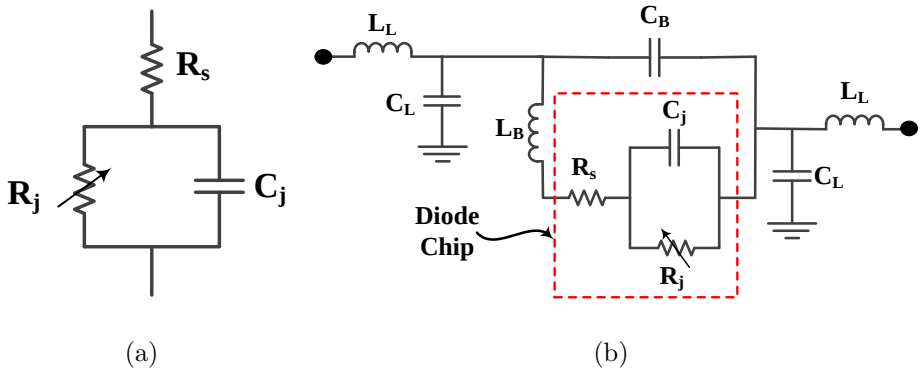

Figure 7.14: Circuit model for (a)the diode chip, and (b) the diode chip including the parasitic inductances and capacitances of the packaging, leadframe and the bondwires [2].

single super cell. The first layer consists of the resonators which are hosted on top of the RT5880 Rogers dielectric material. Then a ground plane is sandwiched between the two dielectric materials (RT5880) and (RO4003). The feeding network along with the rectifiers were placed at the third layer hosted at the bottom of the RO4003 dielectric substrate. The ground plane contains circular holes to ensure that the vias running through the holes (connecting the resonators at layer 1 to the feeding network at layer 3) do not touch the ground plane. The final fabricated system is shown in Fig. 7.9(a) and Fig. 7.9(b).

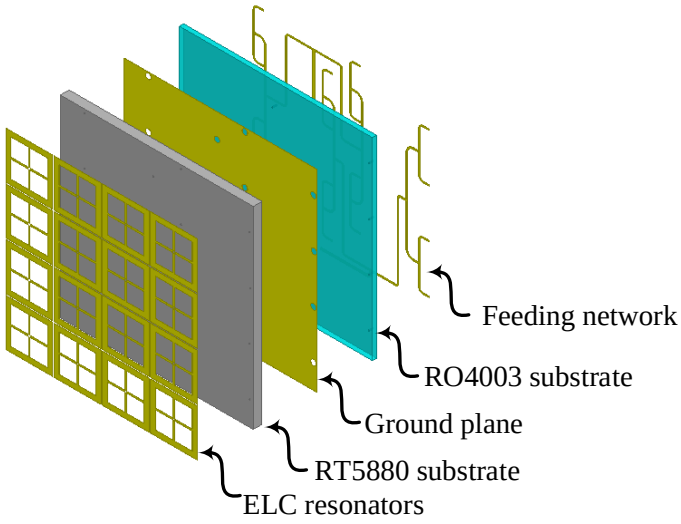

Figure 7.15: A schematic showing an exploded view of the 3 layers and the two substrates within a super cell.

7.8 Conclusion

We demonstrated the design of a microwave energy harvester that is capable of scavenging energy from multiple polarizations. A super cell consisting of 4×4 cells was designed and analysed for maximum radiation to ac conversion efficiency. The collected energy was guided to the load resistance through a hybrid channeling mechanism that combines AC and DC channeling networks. A rectifier was then designed and attached along with a feeding network at a different layer to convert the collected AC power to DC. The obtained measurement results agree well with the simulated ones

aside from a slight shift in the resonance frequency due to fabrication error. Although the proposed energy harvester showed excellent ability to capture the incoming energy from various polarizations, it suffers from a narrow bandwidth. Future work will address this issue.

Chapter 8

Infrared Energy Harvesting using Metasurfaces

8.1 Introduction

The growing demand of electricity around the globe due to population and economic growth coupled with the scarcity and environmental impact of conventional energy resources such as fossil fuels are the main drives for the increasing interest in renewable clean energy. Harvesting solar radiation holds a great promise to solving the current energy crisis due to its abundance at sealevel [66]. Solar radiation spans a wide spectrum including ultraviolet, visible and infrared regimes. The infrared radiation is the chief contributor accounting for 52% of the total solar energy reaching the

earth [145].

Photovoltaics are the most commonly used devices to harvest solar radiation [146]. To excite an electron and allow it to jump from the valence band to the conduction band, a photon with energy slightly greater than the band gap energy is required. However, a great portion of the solar spectrum provides energies much greater than the band gap energy of commonly used semiconductor materials. Thus, the solar cell utilizes a portion of the photon energy to create an electron-hole pair and the rest of the energy is lost through lattice vibration [147]. This limits a single-junction solar cell to a maximum theoretical conversion efficiency of $\approx 31\%$ [148]. To overcome this limitation, multi-junction solar cells are used to create multiple bandgaps that respond to different wavelengths providing efficiencies slightly above 40% [149].

As an alternative means to harvest solar energy with higher efficiencies, Bailey theorized the use of nano-scale rectennas operating at optical frequencies [150]. An optical rectenna consists of a nano antenna to capture solar radiation and a rectifier, Metal Insulator Metal (MIM) diode [151], to convert the captured energy to useful DC power. The recent advancements in nanotechnology enabled the possibility to fabricate optical antennas [152]. The fact that optical rectennas can capture solar energy during

the day and night with wideband reception and higher theoretical conversion efficiency make them advantageous over photovoltaic technology. A number of articles demonstrated full rectenna systems operating at optical frequencies [67, 153]. However, the reported efficiencies were less than 1% due to the large mismatch between the MIM diode and the antenna. In a recent article, a novel rectenna design involving an MIM diode with a small contact area and a very thin oxide layer is used to offer low zero bias resistance that can be easily matched to the antenna and hence increase the overall rectenna system conversion efficiency [153].

The efficiency of the rectenna system depends on the rectification circuitry but more critically on the electromagnetic collector which is the primary wave-to-signal energy transducer in the system. Most of the articles that presented the design and fabrication of optical antennas focus on enhancing the localized field within the feeding point of the antenna [154]. Such measure is indicative of the ability of the antenna to localize the electric field from an impinging planewave within a small area to create a hot spot. For optical antennas used for electromagnetic energy harvesting, it is more meaningful to analyse the antenna in terms of the power conversion efficiency per unit area of the antenna or energy collecting structure. This quantifies the ability of the antenna to capture and channel the electromag-

netic energy to the feeding point of the antenna from an incoming wave, and also facilitates comparison with other system [59].

In this chapter, we focus in the first link of the optical rectenna system. We present a metasurface made of electrically-small resonators based on the perfect absorption concept that is capable of capturing the electromagnetic energy from an incoming planewave and channeling the energy to a resistive load. This concept were proven successful in earlier work where a near unity energy harvesting metasurface comprising 13 $\times$ 13 electrically-small resonators was shown to provide 97% radiation to AC conversion efficiency at the microwave regime [64]. Here, we show through full-wave numerical simulation that a metamaterial medium operating at the infrared regime can achieve conversion efficiencies higher than 90%.

The proposed metamaterial infrared energy harvester design is inspired by the concept of perfect absorption. Infrared metasurface perfect absorbers consist of an array of sub-wavelength unit cells that is capable of absorbing all the energy from an incoming wave [155–157]. This is achievable by simultaneously minimizing the reflectivity and transmissivity from and through the medium. By tailoring the effective μ and ϵ, the metasurface impedance can be matched to the free space impedance, thus minimizing reflections. Wave transmission through the surface can be minimized by plac-

ing a backed ground plane thicker than the skin depth of the incoming wave. In addition, a lossy substrate can be used to dissipate the absorbed energy; therefore, all the energy from an impinged plane wave is absorbed and consumed within the medium. This fact is the initial impetus to use such medium as infrared energy harvesters. However, it was shown in reported metasurface absorbers that a lossy substrate is the main component responsible for consuming the absorbed energy [158]. A metamaterial harvester consisting of split-ring resonators arranged in symmetric and asymmetric configurations were used to capture infrared energy at around 500GHz [87]. In this work, we design of a metamaterial absorber such that the absorbed energy is channelled and delivered to a resistive load, hence it can be used to energize a load instead of being lost in the dielectric substrate.

8.2 Results and Discussion

The proposed metasurface harvester comprised of H-shaped electrically-small resonators is shown in Fig. 8.1. A number of H-shaped resonators with various configurations were introduced in the literature as a building block for metamaterial media [159, 160]. However, The proposed H-Shaped cell is modified to fit the targeted application. The resonator was designed to operate at 30THz with dimensions of L=0.9μm, w=0.14μm, g=0.13μm,

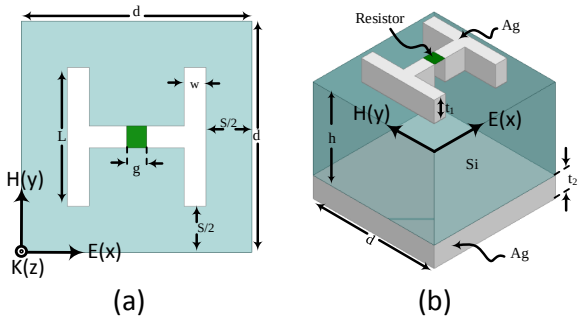

Figure 8.1: A schematic showing the proposed H-shaped metamaterial harvester (a) top view and (b) prospective view

s=0.6μm, t1=0.07μm and a unit cell size of d=1.5μm. The resonator was placed on top of a silicon substrate with a height of h=3.55μm and a dielectric constant of $\epsilon_r = 11.9$. The silicon substrate was chosen to minimize dielectric loss as it experiences low energy absorption at the operating frequency since the bandgap energy of silicon is much higher than the photon energy at infrared regime. The unit cell is backed by a ground plane having a thickness of t2=0.07μm to minimize energy transmission through the medium. Both the H resonator and the ground plane were made of sliver because its low conductive loss at the resonance frequency. The frequency of the H resonator was designed to capture energy during day and night. In addition, to the energy absorption from the sun radiation, the earth re-emits a large amount of infrared energy when it cools off at night. This re-radiated energy peaks at around 30THz, hence the design frequency chosen in this

work.

Using CST MICROWAVE STUDIO, [161] the unit cell was numerically excited by a waveguide having perfect magnetic ($x-z$ plane) and perfect electric ($y-z$ plane) boundaries to ensure TEM mode excitation as shown in Fig. 8.1. Both the H resonator and the ground plane were modeled as silver using a Drude model having a plasma frequency of 2174THz and damping frequency of 4.35THz [162]. A resistive load was placed within the gap of the resonator to mimic a full rectification circuitry. The resistance of the load was selected such that it equals to the input resistance of the resonator when looking from the port of the gap. It was found from the simulation results that the resonator absorb maximum energy when terminated by a resistance of 90 Ω. The scattering parameters of the resonator is extracted when the resonator is terminated by the optimal load resistance. Plots of the absorption, reflection and transmission (Fig. 8.2) show that the resonator experiences full absorption at the operating frequency of 30THz. Although full energy absorption by the resonator is achieved, it is critical to analyse the energy distribution within the resonator as this energy can be dissipated anywhere within the unit cell.

The energy consumed within the unit cell is analyzed as shown in Fig. 8.3. From the Figure, we can observe that 96% of the energy is dissipated by the

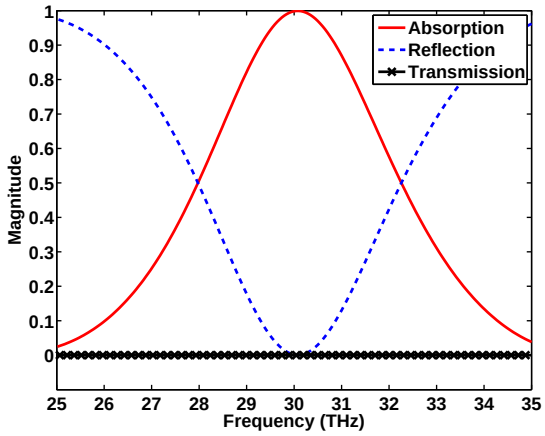

Figure 8.2: Simulation results showing the absorption, reflection and transmission for a single H-resonator unit cell.

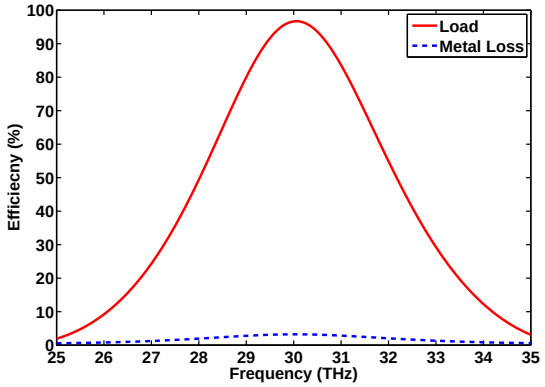

Figure 8.3: Simulation results showing the power distribution of the absorbed energy within a single H-resonator unit cell.

terminated load impedance. This is different from the power distribution within the reported infrared metasurface absorbers where the energy was mostly consumed within the dielectric host material [158]. This is due to

the fact that silicon is a poor absorber at the operating frequency and it was used as a dielectric substrate to minimize dielectric loss. In addition, the inserted load resistance created a different means to dissipate the absorbed energy within the unit cell. By placing a resistive load across the gap of the resonator, a path for the current is created to flow from one arm of the resonator to the other. This can be clearly seen from the surface current distribution plot shown in Fig. 8.4(a) where high concentration of surface current is flowing across the connected load. However, when the load resistance is not present, the maximum magnitude of the surface current within the arms of the resonator reduces by half as shown in Fig. 8.4(b). In addition to the high absorption efficiency of the proposed metasurface harvester, the optimal load impedance connected across the gap can be tuned to match the desired rectification circuitry. The optimal load impedance strongly depends on the resonator dimensions and most critically on the periodicity of the cell denoted by d in Fig. 8.1. Therefore, by varying the resonator dimensions along with the periodicity of the cell one can tune the resonator to the desired load resistance. This can be critical when a low input impedance MIM diode is connected across the gap of the resonator such as the diode presented in [153].

The design was extended to provide energy reception from two orthog-

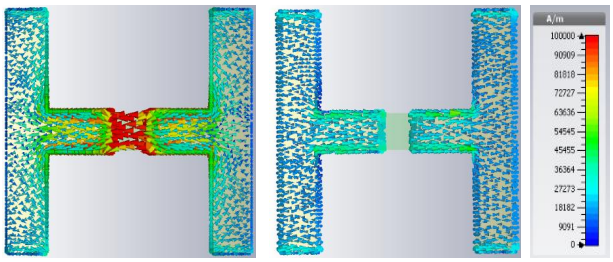

Figure 8.4: Surface current density on the H-resonator (a) with a load and (b) without a load. Dark blue corresponds to 0 A/m and dark red corresponds to 10000A/m.

onal polarizations. The sun emits energy that is randomly polarized in addition to the fact that the angle of maximum solar radiation intensity changes with time. In addition, the re-emitted infrared energy from the earth surface during the earth cooling period at night ranges in wavelength between approximately $7\mu m$ - $14\mu m$ [67]. Hence, it is critical to maximize energy reception within this frequency range from different angles.

Two cross polarized H-resonators with identical dimension and material to the one presented above was designed as shown in Fig. 8.5(a). The top and bottom resonators were hosted on a silicon substrate of heights h1=$4.54\mu m$ and h2=$4.63\mu m$, respectively. The metasurface harvester was backed by a ground plane with a thickness of $t2 = 0.07\ \mu m$ as shown in Fig. 8.5(b). The 5-layer unit cell was excited by a waveguide with two different polarizations to test the ability of the resonators to capture infrared

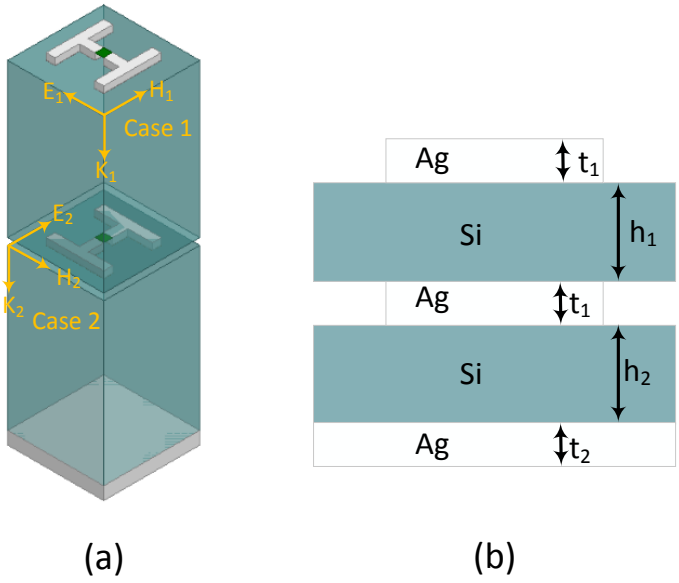

Figure 8.5: A schematic showing the proposed dual polarized H-shaped metamaterial harvester (a) prospective view and (b) side view.

energy from various angles. The polarization of the two excitation cases are shown in Fig. 8.5(a). For each case, the scattering parameters were extracted to plot the energy absorption within the unit cell. Figure 8.6 shows that the unit cell experiences full energy absorption at both polarization cases. In addition, full absorption occurs at multiple bands in particular 25THz, 30THz, and 34THz. All the 3 operating bands were carefully designed to lie within the range of the earth emitted infrared energy at night time. If different bands were desired, one can change the resonator size, substrate thickness and the periodicity of the unit cell to operate at different

frequency bands.

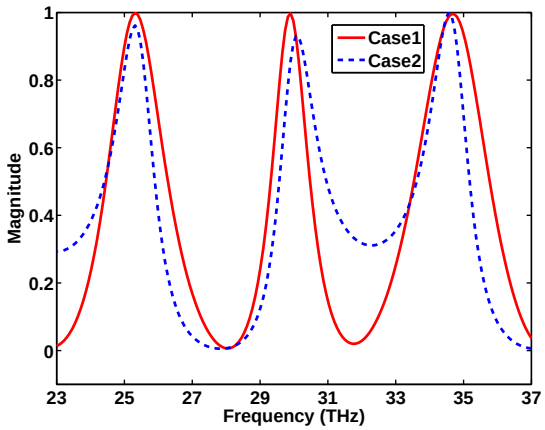

Figure 8.6: Simulation results showing the absorption of the two proposed polarization cases.

The power distribution of the absorbed energy within the 5-layer energy harvester is shown in Fig. 8.7. For the polarization of case I, the unit cell dissipated more than 92% of the absorbed energy across the load resistance. The top resonator is the main contributor to the absorbed energy at the polarization of case I. For case II, the unit cell consumed more than 88% of the absorbed energy across the load of the bottom resonator. In both cases, the unit cell showed energy absorption and channelling to the connected load at the same three bands. This can be attributed to the multi-resonances of the unit cell due to the presence of two substrate materials having different heights. Such features are very critical to maximize energy harvesting in

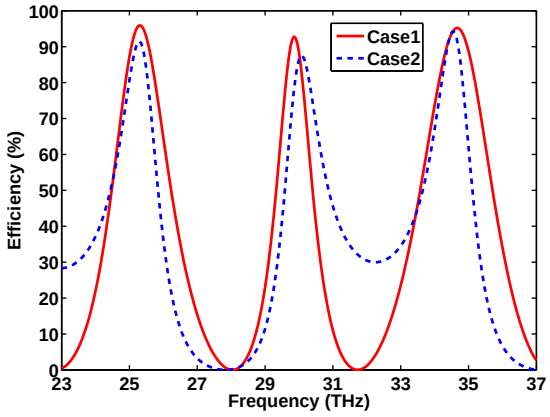

Figure 8.7: Simulation results showing the power distribution of the absorbed energy within the dual polarized 5-layer H-resonator unit cell.

the infrared regime.

It is important to note here that a full and practical realization of the H-resonator metasurface collector/antenna require termination by an MIM diode placed within each gap resonator. Then the energy collected from each cell is combined through power combining network. Although high efficiencies were achieved in both the single and dual polarized unit cells, the silver metallic layers consumed 4% and 12% of the absorbed energy for the single and dual polarized unit cells, respectively. This can be significant loss especially if the mismatch between the diode and the antenna is high. Therefore, low loss metallic materials can be used to minimize the energy dissipated within the resonator and ground layers.

8.3 Conclusion

We presented a numerical study of an infrared metasurface harvester inspired by the perfect absorption concept. The metasurface unit cell was capable of channeling 96% of the absorbed power to a resistive load connected across the gap of the resonator. In addition, a 5-layer unit cell was introduced to provide dual polarization with multiple reception bands. The frequency of operation is selected such that the harvester receives infrared energy throughout the day.

Chapter 9

Accomplished and Future Work

9.1 Accomplished Work

The following list include a summary of the work accomplished in this thesis:

1. A detailed analysis of the radiation to AC conversion efficiency of a common type of antennas (patch antenna) was studied based on the efficiency definition presented in this dissertation (**Chapter 2**).

2. An electromagnetic energy collector based on an array of SRRs that is capable of achieving higher radiation to AC conversion efficiency relative to the collectors presented in the literature was proposed and verified numerically and experimentally (**Chapter 2**).

3. A highly efficient collector that can achieve near unity radiation to AC conversion efficiency based on the full absorption concept using electrically *small* unit cells was presented and verified numerically and experimentally (**Chapter 3**).

4. A method for enhancing radiation to AC conversion efficiency of electromagnetic energy harvesting systems was proposed using 3-dimensional stacked metamaterial arrays (**Chapter 4**).

5. A method for enhancing radiation to DC conversion efficiency of electromagnetic energy harvesting systems was proposed using 3-dimensional stacked folded dipole antenna arrays (**Chapter 5**).

6. A highly efficient collector that can achieve near unity radiation to AC conversion efficiency based on the full absorption concept using electrically *large* unit cells was presented and verified numerically and experimentally. In addition, a simplified channeling methodology to channel the collected AC power and convert it to DC power across a single load using series inductors was achieved (**Chapter 6**).

7. A near unity efficient collector that can collect the radiation energy in the microwave regime from multi-polarized plane wave was presented (**Chapter 7**).

8. A feasibility study of a near unity efficient collector, that can capture the infrared energy and channel it to a resistive load with efficiencies higher than 90% at three frequency bands, was analysed numerically (**Chapter 8**).

9.2 List of Publications

[1] T. S. Almoneef, H. Sun, and O. M. Ramahi, "A 3-d folded dipole antenna array for far-field electromagnetic energy transfer," *IEEE Antennas and Wireless Propagation Letters*, vol. 15, pp. 1406–1409, 2016 **(Accepted)**.

[2] T. S. Almoneef and O. M. Ramahi, "Metamaterial electromagnetic energy harvester with near unity efficiency," *Applied Physics Letters*, vol. 106, no. 15, 2015 **(Accepted)**.

[3] T. Almoneef and O. M. Ramahi, "Split-ring resonator arrays for electromagnetic energy harvesting," *Progress In Electromagnetics Research B*, vol. 62, pp. 167–180, 2015 **(Accepted)**.

[4] T. Almoneef and O. M. Ramahi, "A 3-dimensional stacked metamaterial arrays for electromagnetic energy harvesting," *Progress In Electromagnetics Research*, vol. 146, pp. 109–115, 2014 **(Accepted)**.

[5] O. M. Ramahi, T. S. Almoneef, M. AlShareef, and M. S. Boybay, "Metamaterial particles for electromagnetic energy harvesting," *Applied Physics Letters*, vol. 101, no. 17, 2012 **(Accepted)**.

[6] T. S. Almoneef, F. Erkmen and O. M. Ramahi, "Microwave rectenna system using tightly coupled antennas," *IEEE Transactions on Antenna and Propagation*, 2017 **(Submitted)**.

[7] T. S. Almoneef, F. Erkmen and O. M. Ramahi, "Harvesting the Energy of Multi-Polarized Electromagnetic Waves," *Scientific Reports*,2017 **(Submitted)**.

[8] T. S. Almoneef and O. M. Ramahi, "3-D stacked antenna panels: The promise of high efficient energy harveters," in *Antennas and Propagation (APSURSI), 2016 IEEE International Symposium on.* IEEE, 2016, pp. 601–602 **(Conference)**.

[9] T. S. Almoneef and O. M. Ramahi, "Can split-ring resonators be viable for electromagnetic energy harvesting?" in *Antennas and Propagation Society International Symposium (APSURSI), 2014 IEEE.* IEEE, 2014, pp. 424–425 **(Conference)**.

[10] T. S. Almoneef and O. M. Ramahi, "Harvesting electromagnetic energy using metamaterial particles," in *Antennas and Propagation Society*

International Symposium (APSURSI), 2013 IEEE. IEEE, 2013, pp. 1046–1047 **(Conference)**.

[11] T. Almoneef and O. Ramahi, "337.5: Harvesting electromagnetic energy using metamaterial particles," in *INTERNATIONAL SYMPOSIUM DIGEST ANTENNAS AND PROPAGATION*, vol. 1, no. 2. IEEE, 2013, pp. 1046–1046 **(Conference)**.

[12] O. Ramah, T. Almoneef, B. Alavikia, and A. Ashoor, "Metasurfaces for far-field wireless power transfer" **(Conference)**.

[13] O. Ramahi, "Metasurfaces for far-field wireless power transfer and energy harvesting," in *Qatar Foundation Annual Research Conference Proceedings*, vol. 2016, no. 1. HBKU Press Qatar, 2016, p. EEPP3120 **(Conference)**.

[14] T. S. Almoneef and O. M. Ramahi. Metamaterial electromagnetic energy harvester with near unity efficiency. *US Provisional Patent Application No. 62099219* **(Patent)**.

[15] Omar Ramahi, Thamer Almoneef, and Mohammed AlShareef. Metamaterial particles for electromagnetic energy harvesting, March 15 2013. US Patent App. 13/841,652 **(Patent)**.

[16] O. M. Ramahi and T. S. Almoneef. A three-dimensional stacked metamaterial arrays for electromagnetic energy harvesting. *US Provisional Patent Application No. 61939191* **(Patent)**.

[17] O. M. Ramahi and T. S. Almoneef. A three-dimensional stacked antenna arrays for electromagnetic energy harvesting. *US Provisional Patent Application No. 62033226* **(Patent)**.

[18] T. S. Almoneef and O. M. Ramahi. Folded dipole antenna for electromagnetic energy harvesting. *US Provisional Patent Application No. 62033632* **(Patent)**.

9.3 Future Work

1. **Analyze and compare** different ways to channel the collected AC power to DC that can maximize the overall radiation to DC conversion efficiency.

2. **Extend** the stacking method introduced in (**Chapter 4 & 5**) by combining vertical and horizontal stacked arrays that could further increase the conversion efficiency of the 3-D harvesting system. In (**Chapter 4 & 5**) only vertical stacking is studied, however the space between two

vertical panels can be used to include cross-polarized arrays stacked horizontally to further increase the collection efficiency.

3. **Apply** the proposed collectors and methods to engineering applications. Due to the great efficiency enhancement, the proposed method can be applied to applications such as remote battery charging, RFID's, Space Solar Power and much more.

4. **Fabricate** the infrared near unity collector presented in (**Chapter 8**) and test it experimentally.

5. **Extend** the infrared near unity collector work presented in (**Chapter 8**) by replacing the resistors with MIM diodes to convert the collected AC power to DC.

Bibliography

[1] J. O. McSpadden, Lu Fan, and Kai Chang. Design and experiments of a high-conversion-efficiency 5.8-GHz rectenna. *IEEE Transactions on Microwave Theory and Techniques*, 46(12):2053–2060, Dec 1998.

[2] Hewlett Packard. Linear models for diode surface mount packages. *Application Note 1124*, 1997.

[3] R. Jegadeesan and Y. X. Guo. Topology selection and efficiency improvement of inductive power links. *IEEE Transactions on Antennas and Propagation*, 60(10):4846–4854, Oct 2012.

[4] J. Dai and D. C. Ludois. A survey of wireless power transfer and a critical comparison of inductive and capacitive coupling for small gap applications. *IEEE Transactions on Power Electronics*, 30(11):6017–6029, Nov 2015.

[5] G. Wang, W. Liu, M. Sivaprakasam, M. Zhou, J. D. Weiland, and M. S. Humayun. A dual band wireless power and data telemetry for retinal prosthesis. In *2006 International Conference of the IEEE Engineering in Medicine and Biology Society*, pages 4392–4395, Aug 2006.

[6] A. Fazzi, R. Canegallo, L. Ciccarelli, L. Magagni, F. Natali, E. Jung, P. Rolandi, and R. Guerrieri. 3-d capacitive interconnections with mono- and bi-directional capabilities. *IEEE Journal of Solid-State Circuits*, 43(1):275–284, Jan 2008.

[7] A. M. Sodagar and P. Amiri. Capacitive coupling for power and data telemetry to implantable biomedical microsystems. In *2009 4th International IEEE/EMBS Conference on Neural Engineering*, pages 411–414, April 2009.

[8] J. Dai and D. C. Ludois. Capacitive power transfer through a conformal bumper for electric vehicle charging. *IEEE Journal of Emerging and Selected Topics in Power Electronics*, 4(3):1015–1025, Sept 2016.

[9] R. Jegadeesan, K. Agarwal, Y. X. Guo, S. C. Yen, and N. V. Thakor. Wireless power delivery to flexible subcutaneous implants using capac-

itive coupling. *IEEE Transactions on Microwave Theory and Techniques*, 65(1):280–292, Jan 2017.

[10] André Kurs, Aristeidis Karalis, Robert Moffatt, J. D. Joannopoulos, Peter Fisher, and Marin Soljačić. Wireless power transfer via strongly coupled magnetic resonances. *Science*, 317(5834):83–86, 2007.

[11] A. P. Sample, D. T. Meyer, and J. R. Smith. Analysis, experimental results, and range adaptation of magnetically coupled resonators for wireless power transfer. *IEEE Transactions on Industrial Electronics*, 58(2):544–554, Feb 2011.

[12] B. L. Cannon, J. F. Hoburg, D. D. Stancil, and S. C. Goldstein. Magnetic resonant coupling as a potential means for wireless power transfer to multiple small receivers. *IEEE Transactions on Power Electronics*, 24(7):1819–1825, July 2009.

[13] T. Imura, H. Okabe, and Y. Hori. Basic experimental study on helical antennas of wireless power transfer for electric vehicles by using magnetic resonant couplings. In *2009 IEEE Vehicle Power and Propulsion Conference*, pages 936–940, Sept 2009.

[14] A. K. RamRakhyani, S. Mirabbasi, and M. Chiao. Design and optimization of resonance-based efficient wireless power delivery systems

for biomedical implants. *IEEE Transactions on Biomedical Circuits and Systems*, 5(1):48–63, Feb 2011.

[15] U. Olgun, C. C. Chen, and J. L. Volakis. Investigation of rectenna array configurations for enhanced RF power harvesting. *IEEE Antennas and Wireless Propagation Letters*, 10:262–265, 2011.

[16] S. D. Assimonis, S. N. Daskalakis, and A. Bletsas. Sensitive and efficient RF harvesting supply for batteryless backscatter sensor networks. *IEEE Transactions on Microwave Theory and Techniques*, 64(4):1327–1338, April 2016.

[17] Z. Popovi, S. Korhummel, S. Dunbar, R. Scheeler, A. Dolgov, R. Zane, E. Falkenstein, and J. Hagerty. Scalable RF energy harvesting. *IEEE Transactions on Microwave Theory and Techniques*, 62(4):1046–1056, April 2014.

[18] P. E. Glaser. An overview of the solar power satellite option. *IEEE Transactions on Microwave Theory and Techniques*, 40(6):1230–1238, Jun 1992.

[19] K. Agarwal, R. Jegadeesan, Y. X. Guo, and N. V. Thakor. Wireless power transfer strategies for implantable bioelectronics: Methodolog-

ical review. *IEEE Reviews in Biomedical Engineering*, PP(99):1–1, 2017.

[20] Michael Faraday. Experimental researches in electricity. *Philosophical Transactions of the Royal Society of London*, 122:125–162, 1832.

[21] J Clerk Maxwell. A dynamical theory of the electromagnetic field. *Philosophical Transactions of the Royal Society of London*, 155:459–512, 1865.

[22] William C Brown. The history of power transmission by radio waves. *IEEE Transactions on Microwave Theory and Techniques*, 32(9):1230–1242, 1984.

[23] Jari-Pascal Curty, Michel Declercq, Catherine Dehollain, and Norbert Joehl. *Design and optimization of passive UHF RFID systems*. Springer Science & Business Media, 2006.

[24] Bernd H. Strassner and Kai Chang. Rectifying antennas (rectennas). *Encyclopedia of RF and Microwave Engineering*, 2005.

[25] William C Brown. The history of the development of the rectenna. In *Solar Power Satellite Microwave Power Transmission and Reception*, volume 2141, page 271, 1980.

[26] RM Dickinson. Evaluation of a microwave high-power reception-conversion array for wireless power transmission. 1975.

[27] W. C. Brown and J. F. Triner. Experimental thin-film, etched-circuit rectenna. In *1982 IEEE MTT-S International Microwave Symposium Digest*, pages 185–187, June 1982.

[28] J. Heikkinen and M. Kivikoski. A novel dual-frequency circularly polarized rectenna. *IEEE Antennas and Wireless Propagation Letters*, 2(1):330–333, 2003.

[29] C. Song, Y. Huang, P. Carter, J. Zhou, S. Yuan, Q. Xu, and M. Kod. A novel six-band dual CP rectenna using improved impedance matching technique for ambient RF energy harvesting. *IEEE Transactions on Antennas and Propagation*, 64(7):3160–3171, July 2016.

[30] Yong Huang, N. Shinohara, and H. Toromura. A wideband rectenna for 2.4 GHz-band RF energy harvesting. In *2016 IEEE Wireless Power Transfer Conference (WPTC)*, pages 1–3, May 2016.

[31] M. Arrawatia, M. S. Baghini, and G. Kumar. Broadband bent triangular omnidirectional antenna for RF energy harvesting. *IEEE Antennas and Wireless Propagation Letters*, 15:36–39, 2016.

[32] C. Song, Y. Huang, J. Zhou, J. Zhang, S. Yuan, and P. Carter. A high-efficiency broadband rectenna for ambient wireless energy harvesting. *IEEE Transactions on Antennas and Propagation*, 63(8):3486–3495, Aug 2015.

[33] J. A. Hagerty, N. D. Lopez, B. Popovic, and Z. Popovic. Broadband rectenna arrays for randomly polarized incident waves. In *2000 30th European Microwave Conference*, pages 1–4, Oct 2000.

[34] J. A. Hagerty, F. B. Helmbrecht, W. H. McCalpin, R. Zane, and Z. B. Popovic. Recycling ambient microwave energy with broad-band rectenna arrays. *IEEE Transactions on Microwave Theory and Techniques*, 52(3):1014–1024, March 2004.

[35] Ning Zhu, Richard W. Ziolkowski, and Hao Xin. A metamaterial-inspired, electrically small rectenna for high-efficiency, low power harvesting and scavenging at the global positioning system L1 frequency. *Applied Physics Letters*, 99(11):114101, 2011.

[36] W. H. Tu, S. H. Hsu, and K. Chang. Compact 5.8-GHz rectenna using stepped-impedance dipole antenna. *IEEE Antennas and Wireless Propagation Letters*, 6:282–284, 2007.

[37] M. Ali, G. Yang, and R. Dougal. Miniature circularly polarized rectenna with reduced out-of-band harmonics. *IEEE Antennas and Wireless Propagation Letters*, 5(1):107–110, Dec 2006.

[38] Yu-Jiun Ren and Kai Chang. 5.8-GHz circularly polarized dual-diode rectenna and rectenna array for microwave power transmission. *IEEE Transactions on Microwave Theory and Techniques*, 54(4):1495–1502, June 2006.

[39] H. Sun, Y. x. Guo, M. He, and Z. Zhong. A dual-band rectenna using broadband yagi antenna array for ambient RF power harvesting. *IEEE Antennas and Wireless Propagation Letters*, 12:918–921, 2013.

[40] S. Ladan, A. B. Guntupalli, and K. Wu. A high-efficiency 24 GHz rectenna development towards millimeter-wave energy harvesting and wireless power transmission. *IEEE Transactions on Circuits and Systems I: Regular Papers*, 61(12):3358–3366, Dec 2014.

[41] J. A. G. Akkermans, M. C. van Beurden, G. J. N. Doodeman, and H. J. Visser. Analytical models for low-power rectenna design. *IEEE Antennas and Wireless Propagation Letters*, 4:187–190, 2005.

[42] B. Strassner and Kai Chang. 5.8-GHz circularly polarized dual-rhombic-loop traveling-wave rectifying antenna for low power-density

wireless power transmission applications. *IEEE Transactions on Microwave Theory and Techniques*, 51(5):1548–1553, May 2003.

[43] A. Georgiadis, G. Vera Andia, and A. Collado. Rectenna design and optimization using reciprocity theory and harmonic balance analysis for electromagnetic (eM) energy harvesting. *IEEE Antennas and Wireless Propagation Letters*, 9:444–446, 2010.

[44] F. Erkmen, T. S. Almoneef, and O. M. Ramahi. Electromagnetic energy harvesting using full-wave rectification. *IEEE Transactions on Microwave Theory and Techniques*, 65(5):1843–1851, May 2017.

[45] Z. Harouni, L. Cirio, L. Osman, A. Gharsallah, and O. Picon. A dual circularly polarized 2.45-GHz rectenna for wireless power transmission. *IEEE Antennas and Wireless Propagation Letters*, 10:306–309, 2011.

[46] X. X. Yang, C. Jiang, A. Z. Elsherbeni, F. Yang, and Y. Q. Wang. A novel compact printed rectenna for data communication systems. *IEEE Transactions on Antennas and Propagation*, 61(5):2532–2539, May 2013.

[47] T. S. Almoneef, H. Sun, and O. M. Ramahi. A 3-d folded dipole antenna array for far-field electromagnetic energy transfer. *IEEE Antennas and Wireless Propagation Letters*, 15:1406–1409, 2016.

[48] S. Y. Yang and J. Kim. Wireless power transmission using dipole rectennas made on flexible cellulose membrane. *IET Microwaves, Antennas Propagation*, 6(7):756–760, May 2012.

[49] K. Niotaki, S. Kim, S. Jeong, A. Collado, A. Georgiadis, and M. M. Tentzeris. A compact dual-band rectenna using slot-loaded dual band folded dipole antenna. *IEEE Antennas and Wireless Propagation Letters*, 12:1634–1637, 2013.

[50] E. Falkenstein, M. Roberg, and Z. Popovic. Low-power wireless power delivery. *IEEE Transactions on Microwave Theory and Techniques*, 60(7):2277–2286, July 2012.

[51] N. P. Basta, E. A. Falkenstein, and Z. Popovic. Bow-tie rectenna arrays. In *2015 IEEE Wireless Power Transfer Conference (WPTC)*, pages 1–4, May 2015.

[52] W. Zhao, K. Choi, S. Bauman, Z. Dilli, T. Salter, and M. Peckerar. A radio-frequency energy harvesting scheme for use in low-power ad hoc

distributed networks. *IEEE Transactions on Circuits and Systems II: Express Briefs*, 59(9):573–577, Sept 2012.

[53] H. Kamoda, S. Kitazawa, N. Kukutsu, and K. Kobayashi. Loop antenna over artificial magnetic conductor surface and its application to dual-band RF energy harvesting. *IEEE Transactions on Antennas and Propagation*, 63(10):4408–4417, Oct 2015.

[54] H. K. Chiou and I. S. Chen. High-efficiency dual-band on-chip rectenna for 35- and 94-GHz wireless power transmission in 0.13-μm cmos technology. *IEEE Transactions on Microwave Theory and Techniques*, 58(12):3598–3606, Dec 2010.

[55] T. C. Yo, C. M. Lee, C. M. Hsu, and C. H. Luo. Compact circularly polarized rectenna with unbalanced circular slots. *IEEE Transactions on Antennas and Propagation*, 56(3):882–886, March 2008.

[56] P. Lu, X. S. Yang, J. L. Li, and B. Z. Wang. Polarization reconfigurable broadband rectenna with tunable matching network for microwave power transmission. *IEEE Transactions on Antennas and Propagation*, 64(3):1136–1141, March 2016.

[57] C. Liu, Y. X. Guo, H. Sun, and S. Xiao. Design and safety considerations of an implantable rectenna for far-field wireless power transfer.

IEEE Transactions on Antennas and Propagation, 62(11):5798–5806, Nov 2014.

[58] L. W. Epp, A. R. Khan, H. K. Smith, and R. P. Smith. A compact dual-polarized 8.51-GHz rectenna for high-voltage (50 v) actuator applications. *IEEE Transactions on Microwave Theory and Techniques*, 48(1):111–120, Jan 2000.

[59] Omar M. Ramahi, Thamer S. Almoneef, Mohammed AlShareef, and Muhammed S. Boybay. Metamaterial particles for electromagnetic energy harvesting. *Applied Physics Letters*, 101(17):173903, 2012.

[60] Thamer Almoneef and Omar M Ramahi. Split-ring resonator arrays for electromagnetic energy harvesting. *Progress In Electromagnetics Research B*, 62:167–180, 2015.

[61] Mohamed El Badawe, Thamer S. Almoneef, and Omar M. Ramahi. A metasurface for conversion of electromagnetic radiation to DC. *AIP Advances*, 7(3):035112, 2017.

[62] R. Wang, D. Ye, S. Dong, Z. Peng, Y. Salamin, F. Shen, J. Huangfu, C. Li, and L. Ran. Optimal matched rectifying surface for space solar power satellite applications. *IEEE Transactions on Microwave Theory and Techniques*, 62(4):1080–1089, April 2014.

[63] Babak Alavikia, Thamer S. Almoneef, and Omar M. Ramahi. Complementary split ring resonator arrays for electromagnetic energy harvesting. *Applied Physics Letters*, 107(3):033902, 2015.

[64] Thamer S. Almoneef and Omar M. Ramahi. Metamaterial electromagnetic energy harvester with near unity efficiency. *Applied Physics Letters*, 106(15):153902, 2015.

[65] R.B. Erb. Power from space the tough questions: The 1995 Peter E. Glaser lecture. *Acta Astronautica*, 38(48):539 – 550, 1996. Benefits of Space for Humanity.

[66] John Mankins. *The case for space solar power*. Virginia Edition Publishing, 2014.

[67] A. M. A. Sabaawi, C. C. Tsimenidis, and B. S. Sharif. Analysis and modeling of infrared solar rectennas. *IEEE Journal of Selected Topics in Quantum Electronics*, 19(3):9000208–9000208, May 2013.

[68] G. Andia Vera, S. D. Nawale, Y. Duroc, and S. Tedjini. Read range enhancement by harmonic energy harvesting in passive UHF RFID. *IEEE Microwave and Wireless Components Letters*, 25(9):627–629, Sept 2015.

[69] F. J. Huang, C. M. Lee, C. L. Chang, L. K. Chen, T. C. Yo, and C. H. Luo. Rectenna application of miniaturized implantable antenna design for triple-band biotelemetry communication. *IEEE Transactions on Antennas and Propagation*, 59(7):2646–2653, July 2011.

[70] K. M. Z. Shams and M. Ali. Wireless power transmission to a buried sensor in concrete. *IEEE Sensors Journal*, 7(12):1573–1577, Dec 2007.

[71] J. A. Hagerty and Z. Popovic. An experimental and theoretical characterization of a broadband arbitrarily-polarized rectenna array. In *2001 IEEE MTT-S International Microwave Sympsoium Digest (Cat. No.01CH37157)*, volume 3, pages 1855–1858 vol.3, May 2001.

[72] W.C. Brown. Electronic and mechanical improvement of the receiving terminal of a free-space microwave power transmission system. *NASA STI/Recon Technical Report N*, 77:31613, 1977.

[73] L. Solymar and E. Shamonina. *Waves in metamaterials*. Oxford University Press, USA, 2009.

[74] SL Zhai, XP Zhao, S Liu, FL Shen, LL Li, and CR Luo. Inverse doppler effects in broadband acoustic metamaterials. *Scientific Reports*, 6, 2016.

[75] Kyungjun Song, Seong-Hyun Lee, Kiwon Kim, Shin Hur, and Jedo Kim. Emission enhancement of sound emitters using an acoustic metamaterial cavity. *Scientific reports*, 4:4165, 2014.

[76] Stanley P Burgos, Rene De Waele, Albert Polman, and Harry A Atwater. A single-layer wide-angle negative-index metamaterial at visible frequencies. *Nature Materials*, 9(5):407–412, 2010.

[77] Henri J Lezec, Jennifer A Dionne, and Harry A Atwater. Negative refraction at visible frequencies. *Science*, 316(5823):430–432, 2007.

[78] Wenshan Cai, Uday K Chettiar, Alexander V Kildishev, and Vladimir M Shalaev. Optical cloaking with metamaterials. *Nature photonics*, 1(4):224–227, 2007.

[79] Andrea Alu and Nader Engheta. Plasmonic and metamaterial cloaking: physical mechanisms and potentials. *Journal of Optics A: Pure and Applied Optics*, 10(9):093002, 2008.

[80] Richard A Shelby, David R Smith, and Seldon Schultz. Experimental verification of a negative index of refraction. *science*, 292(5514):77–79, 2001.

[81] John Brian Pendry. Negative refraction makes a perfect lens. *Physical review letters*, 85(18):3966, 2000.

[82] N I Landy, S Sajuyigbe, JJ Mock, DR Smith, and WJ Padilla. Perfect metamaterial absorber. *Physical Review Letters*, 100(20):207402, 2008.

[83] Z.L. Mei, J. Bai, T.M. Niu, and T.J. Cui. A half maxwell fish-eye lens antenna based on gradient-index metamaterials. *Antennas and Propagation, IEEE Transactions on*, 60(1):398–401, 2012.

[84] MF Khan and MJ Mughal. Design of tunable metamaterials by varying the height of rings of s-shaped resonator. In *Electrical Engineering, 2009. ICEE'09. Third International Conference on*, pages 1–4. IEEE, 2009.

[85] K. Aydin, I. Bulu, K. Guven, M. Kafesaki, C.M. Soukoulis, and E. Ozbay. Investigation of magnetic resonances for different split-ring resonator parameters and designs. *New journal of physics*, 7:168, 2005.

[86] F. Bilotti, A. Toscano, L. Vegni, K. Aydin, K.B. Alici, and E. Ozbay. Equivalent-circuit models for the design of metamaterials based on artificial magnetic inclusions. *Microwave Theory and Techniques, IEEE Transactions on*, 55(12):2865–2873, 2007.

[87] Mohammed R. AlShareef and Omar M. Ramahi. Electrically small resonators for energy harvesting in the infrared regime. *Journal of Applied Physics*, 114(22):223101, 2013.

[88] James E. Storer. Impedance of thin-wire loop antennas. *American Institute of Electrical Engineers, Part I: Communication and Electronics, Transactions of the*, 75(5):606–619, Nov 1956.

[89] M. Gorkunov, M. Lapine, E. Shamonina, and K. H. Ringhofer. Effective magnetic properties of a composite material with circular conductive elements. *Eur. Phys. J. B.*, 28:263–269, 2002.

[90] K Balman and E Jordan. *Electromagnetic waves and radiating systems*. Prentice Hall, New Jersey, 1968.

[91] H. T. Hui. A new definition of mutual impedance for application in dipole receiving antenna arrays. *IEEE Antennas and Wireless Propagation Letters*, 3(1):364–367, Dec 2004.

[92] Hon Tat Hui. A practical approach to compensate for the mutual coupling effect in an adaptive dipole array. *IEEE Transactions on Antennas and Propagation*, 52(5):1262–1269, May 2004.

[93] Hon Tat Hui, Kam Yuen Chan, and E. K. N. Yung. Compensating for the mutual coupling effect in a normal-mode helical antenna array for

adaptive ing. *IEEE Transactions on Vehicular Technology*, 52(4):743–751, July 2003.

[94] Y. Yu, H. S. Lui, C. H. Niow, and H. T. Hui. Improved DOA estimations using the receiving mutual impedances for mutual coupling compensation: An experimental study. *IEEE Transactions on Wireless Communications*, 10(7):2228–2233, July 2011.

[95] C. H. Niow and H. T. Hui. Improved noise modeling with mutual coupling in receiving antenna arrays for direction-of-arrival estimation. *IEEE Transactions on Wireless Communications*, 11(4):1616–1621, April 2012.

[96] M. M. Bait-Suwailam, O. F. Siddiqui, and O. M. Ramahi. Mutual coupling reduction between microstrip patch antennas using slotted-complementary split-ring resonators. *IEEE Antennas and Wireless Propagation Letters*, 9:876–878, 2010.

[97] M. M. Bait-Suwailam, M. S. Boybay, and O. M. Ramahi. Electromagnetic coupling reduction in high-profile monopole antennas using single-negative magnetic metamaterials for mimo applications. *IEEE Transactions on Antennas and Propagation*, 58(9):2894–2902, Sept 2010.

[98] Warren L Stutzman and GA Thiele. Antenna theory and design, 1981. *John Wiley New York*.

[99] Buon Kiong Lau and Zhinong Ying. Antenna design challenges and solutions for compact mimo terminals. In *Antenna Technology (iWAT), 2011 International Workshop on*, pages 70–73, 2011.

[100] Jiaming Hao, Jing Wang, Xianliang Liu, Willie J. Padilla, Lei Zhou, and Min Qiu. High performance optical absorber based on a plasmonic metamaterial. *Applied Physics Letters*, 96(25):251104, 2010.

[101] Koray Aydin, Vivian E Ferry, Ryan M Briggs, and Harry A Atwater. Broadband polarization-independent resonant light absorption using ultrathin plasmonic super absorbers. *Nature Communications*, 2:517, 2011.

[102] Fei Ding, Yanxia Cui, Xiaochen Ge, Yi Jin, and Sailing He. Ultra-broadband microwave metamaterial absorber. *Applied Physics Letters*, 100(10):103506, 2012.

[103] Jianping Hao, ric Lheurette, Ludovic Burgnies, tienne Okada, and Didier Lippens. Bandwidth enhancement in disordered metamaterial absorbers. *Applied Physics Letters*, 105(8):081102, 2014.

[104] Somak Bhattacharyya and Kumar Vaibhav Srivastava. Triple band polarization-independent ultra-thin metamaterial absorber using electric field-driven LC resonator. *Journal of Applied Physics*, 115(6):064508, 2014.

[105] Shuomin Zhong and Sailing He. Ultrathin and lightweight microwave absorbers made of mu-near-zero metamaterials. *Scientific Reports*, 3:2083, 2013.

[106] Xiaopeng Shen, Tie Jun Cui, Junming Zhao, Hui Feng Ma, Wei Xiang Jiang, and Hui Li. Polarization-independent wide-angle triple-band metamaterial absorber. *Opt. Express*, 19(10):9401–9407, May 2011.

[107] Wangren Xu and Sameer Sonkusale. Microwave diode switchable metamaterial reflector/absorber. *Applied Physics Letters*, 103(3):031902, 2013.

[108] Yong Zhi Cheng, Ying Wang, Yan Nie, Rong Zhou Gong, Xuan Xiong, and Xian Wang. Design, fabrication and measurement of a broadband polarization-insensitive metamaterial absorber based on lumped elements. *Journal of Applied Physics*, 111(4):044902, 2012.

[109] Guo-Hui Yang, Xiao-Xin Liu, Yue-Long Lv, Jia-Hui Fu, Qun Wu, and Xuemai Gu. Broadband polarization-insensitive absorber based

on gradient structure metamaterial. *Journal of Applied Physics*, 115(17):17E523, 2014.

[110] Suresh Venkatesh, David Shrekenhamer, Wangren Xu, Sameer Sonkusale, Willie Padilla, and David Schurig. Interferometric direction finding with a metamaterial detector. *Applied Physics Letters*, 103(25):254103, 2013.

[111] David Shrekenhamer, Wangren Xu, Suresh Venkatesh, David Schurig, Sameer Sonkusale, and Willie J. Padilla. Experimental realization of a metamaterial detector focal plane array. *Physical Review Letters*, 109:177401, Oct 2012.

[112] Y. J. Yoo, H. Y. Zheng, Y. J. Kim, J. Y. Rhee, J.-H. Kang, K. W. Kim, H. Cheong, Y. H. Kim, and Y. P. Lee. Flexible and elastic metamaterial absorber for low frequency, based on small-size unit cell. *Applied Physics Letters*, 105(4):041902, 2014.

[113] D. Schurig, J. J. Mock, and D. R. Smith. Electric-field-coupled resonators for negative permittivity metamaterials. *Applied Physics Letters*, 88(4):041109, 2006.

[114] Hu Tao, C. M. Bingham, A. C. Strikwerda, D. Pilon, D. Shrekenhamer, N. I. Landy, K. Fan, X. Zhang, W. J. Padilla, and R. D.

Averitt. Highly flexible wide angle of incidence terahertz metamaterial absorber: Design, fabrication, and characterization. *Physical Review B*, 78:241103, Dec 2008.

[115] D. R. Smith, D. C. Vier, Th. Koschny, and C. M. Soukoulis. Electromagnetic parameter retrieval from inhomogeneous metamaterials. *Physical Review E*, 71:036617, Mar 2005.

[116] Y.H. Suh and K. Chang. A high-efficiency dual-frequency rectenna for 2.45-and 5.8-GHz wireless power transmission. *Microwave Theory and Techniques, IEEE Transactions on*, 50(7):1784–1789, 2002.

[117] Allen M Hawkes, Alexander R Katko, and Steven A Cummer. A microwave metamaterial with integrated power harvesting functionality. *Applied Physics Letters*, 103(16):163901, 2013.

[118] ANSYS HFSS Version 15.0.0. Ansys Inc. *http://www.ansys.com*.

[119] Marco Bernardi, Nicola Ferralis, Jin H Wan, Rachelle Villalon, and Jeffrey C Grossman. Solar energy generation in three dimensions. *Energy & Environmental Science*, 5(5):6880–6884, 2012.

[120] Ralph H Nansen. Wireless power transmission: the key to solar power satellites. *Aerospace and Electronic Systems Magazine, IEEE*, 11(1):33–39, 1996.

[121] Thamer Almoneef and Omar M Ramahi. A 3-dimensional stacked metamaterial arrays for electromagnetic energy harvesting. *Progress In Electromagnetics Research*, 146:109–115, 2014.

[122] Ying Liu, Hu Liu, Ming Wei, and Shuxi Gong. A novel slot yagi-like multilayered antenna with high gain and large bandwidth. *Antennas and Wireless Propagation Letters, IEEE*, 13:790–793, 2014.

[123] H. Maema and T. Fukusako. Radiation efficiency improvement for electrically small and low-profile antenna by stacked elements. *Antennas and Wireless Propagation Letters, IEEE*, 13:305–308, 2014.

[124] XM Zhang, JL Huyan, PC Gao, H Wang, and YF Zheng. Stacked series-fed linear array antenna with reduced sidelobe. *Electronics Letters*, 50(4):251–253, 2014.

[125] J.J. Schlesak, A. Alden, and T. Ohno. A microwave powered high altitude platform. In *Microwave Symposium Digest, 1988., IEEE MTT-S International*, pages 283–286 vol.1, May 1988.

[126] T. Sakamoto, Y. Ushijima, E. Nishiyama, M. Aikawa, and I Toyoda. 5.8-GHz series/parallel connected rectenna array using expandable differential rectenna units. *Antennas and Propagation, IEEE Transactions on*, 61(9):4872–4875, Sept 2013.

[127] D. Masotti, A. Costanzo, P. Francia, M. Filippi, and A. Romani. A load-modulated rectifier for RF micropower harvesting with start-up strategies. *Microwave Theory and Techniques, IEEE Transactions on*, 62(4):994–1004, April 2014.

[128] Ben A Munk. *Finite antenna arrays and FSS*. John Wiley & Sons, 2003.

[129] E. A. Alwan, K. Sertel, and J. L. Volakis. A simple equivalent circuit model for ultrawideband coupled arrays. *IEEE Antennas and Wireless Propagation Letters*, 2012.

[130] J. P. Doane, K. Sertel, and J. L. Volakis. A wideband, wide scanning tightly coupled dipole array with integrated balun (TCDA-IB). *IEEE Transactions on Antennas and Propagation*, 61(9):4538–4548, Sept 2013.

[131] H. Wheeler. Simple relations derived fom a phased-array antenna made of an infinite current sheet. *IEEE Transactions on Antennas and Propagation*, 13(4):506–514, July 1965.

[132] D. K. Papantonis and J. L. Volakis. Dual-polarized tightly coupled array with substrate loading. *IEEE Antennas and Wireless Propagation Letters*, 2016.

[133] I. Tzanidis, K. Sertel, and J. L. Volakis. Uwb low-profile tightly coupled dipole array with integrated balun and edge terminations. *IEEE Transactions on Antennas and Propagation*, 61(6):3017–3025, June 2013.

[134] W. H. Choi, J. H. Shin, T. H. Song, J. B. Kim, C. M. Cho, W. J. Lee, and C. G. Kim. Design of circuit-analog (CA) absorber and application to the leading edge of a wing-shaped structure. *IEEE Transactions on Electromagnetic Compatibility*, 56(3):599–607, June 2014.

[135] D. Kundu, A. Mohan, and A. Chakrabarty. Thickness reduction of single layer circuit analog absorber. In *2015 IEEE Applied Electromagnetics Conference (AEMC)*, pages 1–2, Dec 2015.

[136] BA Munk. Frequency selective surfaces: theory and design. 2005. *Hoboken: John Wiley & Sons*.

[137] Y. Shang, Z. Shen, and S. Xiao. On the design of single-layer circuit analog absorber using double-square-loop array. *IEEE Transactions on Antennas and Propagation*, 61(12):6022–6029, Dec 2013.

[138] B. A. Munk, P. Munk, and J. Pryor. On designing Jaumann and circuit analog absorbers (CA Absorbers) for oblique angle of incidence. *IEEE Transactions on Antennas and Propagation*, 55(1):186–193, Jan 2007.

[139] S. M. Rouzegar, A. Alighanbari, and O. M. Ramahi. Wideband uniplanar artificial magnetic conductors based on curved coupled microstrip line resonators. *IEEE Microwave and Wireless Components Letters*, 27(4):326–328, April 2017.

[140] Nathan Marcuvitz. *Waveguide handbook*. Number 21. Iet, 1951.

[141] D. R. Smith, Willie J. Padilla, D. C. Vier, S. C. Nemat-Nasser, and S. Schultz. Composite medium with simultaneously negative permeability and permittivity. *Physical Review Letters*, 84:4184–4187, May 2000.

[142] B. Semnani and A. Borji. Lower bound on scattered power from antennas. *IEEE Antennas and Wireless Propagation Letters*, 11:373–376, 2012.

[143] Constantine A Balanis. *Antenna theory: analysis and design*. John Wiley & Sons, 2016.

[144] W. Kahn and H. Kurss. Minimum-scattering antennas. *IEEE Transactions on Antennas and Propagation*, 13(5):671–675, Sept 1965.

[145] Daryl Ronald Myers. *Solar radiation: practical modeling for renewable energy applications*. CRC Press, 2013.

[146] Antonio Luque. Will we exceed 50% efficiency in photovoltaics? *Journal of Applied Physics*, 110(3):–, 2011.

[147] Dale K Kotter, Steven D Novack, WD Slafer, and PJ Pinhero. Theory and manufacturing processes of solar nanoantenna electromagnetic collectors. *Journal of Solar Energy Engineering*, 132(1):011014, 2010.

[148] William Shockley and Hans J. Queisser. Detailed balance limit of efficiency of pn junction solar cells. *Journal of Applied Physics*, 32(3), 1961.

[149] R. R. King, D. C. Law, K. M. Edmondson, C. M. Fetzer, G. S. Kinsey, H. Yoon, R. A. Sherif, and N. H. Karam. 40% efficient metamorphic gainpgainasge multijunction solar cells. *Applied Physics Letters*, 90(18):–, 2007.

[150] Robert Leo Bailey. A proposed new concept for a solar-energy converter. *Journal of Engineering for Gas Turbines and Power*, 94(2):73–77, 1972.

[151] S. Grover and G. Moddel. Applicability of metal/insulator/metal (MIM) diodes to solar rectennas. *Photovoltaics, IEEE Journal of*, 1(1):78–83, July 2011.

[152] Daniel Dregely, Richard Taubert, Jens Dorfmüller, Ralf Vogelgesang, Klaus Kern, and Harald Giessen. 3d optical yagi-uda nanoantenna array. *Nature Communications*, 2:267, 2011.

[153] MN Gadalla, M Abdel-Rahman, and Atif Shamim. Design, optimization and fabrication of a 28.3 THz nano-rectenna for infrared detection and rectification. *Scientific Reports*, 4, 2014.

[154] Cheryl Feuillet-Palma, Yanko Todorov, Angela Vasanelli, and Carlo Sirtori. Strong near field enhancement in THz nano-antenna arrays. *Scientific Reports*, 3, 2013.

[155] Yoav Avitzour, Yaroslav A. Urzhumov, and Gennady Shvets. Wide-angle infrared absorber based on a negative-index plasmonic metamaterial. *Physical Review B*, 79:045131, Jan 2009.

[156] Ben-Xin Wang, Ling-Ling Wang, Gui-Zhen Wang, Wei qing Huang, Xiao fei Li, and Xiang Zhai. Theoretical investigation of broadband and wide-angle terahertz metamaterial absorber. *Photonics Technology Letters, IEEE*, 26(2):111–114, Jan 2014.

[157] Xiang Xiong, Zhen-Hong Xue, Cong Meng, Shang-Chi Jiang, Yu-Hui Hu, Ru-Wen Peng, and Mu Wang. Polarization-dependent perfect absorbers/reflectors based on a three-dimensional metamaterial. *Physical Review B*, 88:115105, Sep 2013.

[158] Xianliang Liu, Tatiana Starr, Anthony F. Starr, and Willie J. Padilla. Infrared spatial and frequency selective metamaterial with near-unity absorbance. *Physical Review Letters*, 104:207403, May 2010.

[159] David Shrekenhamer, Wen-Chen Chen, and Willie J. Padilla. Liquid crystal tunable metamaterial absorber. *Physical Review Letters*, 110:177403, Apr 2013.

[160] Jiaming Hao, Yu Yuan, Lixin Ran, Tao Jiang, Jin Au Kong, C. T. Chan, and Lei Zhou. Manipulating electromagnetic wave polarizations

by anisotropic metamaterials. *Physical Review Letters*, 99:063908, Aug 2007.

[161] CST STUDIO SUITE. CST Computer Simulation Technology AG. *www.cst.com*.

[162] MA Ordal, LL Long, RJ Bell, SE Bell, RR Bell, RW Alexander, and CA Ward. Optical properties of the metals al, co, cu, au, fe, pb, ni, pd, pt, ag, ti, and w in the infrared and far infrared. *Applied Optics*, 22(7):1099–1119, 1983.